University of Glasgow & University of Applied Sciences Karlsruhe

Thesis submitted in fulfilment of the requirements for the
degree of Master of Science (M.Sc.)

SIMULATION OF HAEMODYNAMIC FLOW IN HEAD AND NECK CHEMOTHERAPY

Research about the unsteady distribution of a chemical agent in head and neck vessels in the treatment of human cancer using multiphase computational fluid dynamics

Stephan Rhode

October 2010–March 2011

Supervisor from University of Glasgow
Dr Manosh Paul
Supervisor from University of Applied Sciences Karlsruhe
Prof. Dr.-Ing. Eckhard Martens

University of Glasgow

Hochschule Karlsruhe
Technik und Wirtschaft
UNIVERSITY OF APPLIED SCIENCES

License:

st.rhode@gmail.com

Typesetting:
LaTeX, BibTeX, TikZ, pgfplots, nomencl, hyperref, KOMA-Script and some additional packages.

Für Tanja

ABSTRACT

In recent years, intra arterial chemotherapy has become an important component in head and neck cancer treatment. However, therapy success can vary significantly and consistent treatment guidelines are missing.

The purpose of this study was to create a computer simulation of the chemical agent injection in the head and neck arteries to investigate the distribution and concentration of the chemical. This is of great interest for medical scientists and vital for prognosis. Realistic three dimensional patient specific geometry was created from image scan data. Engineering principles such as conservation of mass and momentum, turbulence models and a multiphase model were applied in a computational fluid dynamics (CFD) software.

At first, a steady cause and effect study with various turbulence and material models was made without the chemical component. It was discovered, that a non-*Newtonian* material model is compulsory for blood. The shear stress transport k-ω turbulence model is appropriate for the whole velocity range and of superior robustness.

These conclusions were used in the following two-component transient simulation. Pulsatile blood flow, turbulence, the chemical agent injection via a catheter and the mixture between blood and the chemical were considered. The principal conclusion was; the modelled catheter position right before the common carotid artery bifurcation produced an ineffective cisplatin distribution consistent throughout all the arteries. Due to high wall shear stress and turbulence at the inner bifurcation wall, serious complications during the treatment could occur, for instance heamolysis or acute vascular endothelial changes.

To the best of the author's knowledge a novel CFD based approach was introduced, suitable for the optimization and the formulation of treatment guidelines in intra arterial injection chemotherapy. After a required validation, this model can be modified to investigate the influence of various catheter positions and dose rate schemes in future simulations.

Keywords: patient specific geometry; computational fluid dynamics; multiphase model; pulsatile blood flow; chemotherapy; non-*Newtonian* material model

Acknowledgements

It is an honour to have the great opportunity to finish my studies with a research project abroad. This thesis would not have been possible without the support of numerous contributors.

I am heartily thankful to my supervisor Dr Manosh Paul for offering this challenging and exceptional topic and for his guidance and support during the whole project. I owe my deepest gratitude to my supervisor Prof. Eckhard Martens for his encouragement and guidance. Thank you for the generous funding that allows me to publish the results of my work at the CMBE conference in Washington. I know that this is anything but ordinary in a Master's thesis. I am grateful to Duncan Campbell for his introduction and support in the medical aspects of this project. Hopefully, this report provides you with an appropriate background for any further investigation to optimize the treatment strategies in the future.

I benefited from numerous published studies of researchers in biomedical sciences all over the world and owe them a debt of gratitude. I would like to show my thanks to the ERASMUS program for awarding a scholarship and to the very helpful exchange coordinators. I very much appreciate the effort of many people in the LaTeX community. Their awesome work makes it possible to use professional typesetting in this report and proves that open software is superior.

I would like to thank my parents for their contribution and of course my wife Tanja for her encouragement and patience during this time. My apologies if I have inadvertently omitted anyone to whom acknowledgement is due.

Stephan Rhode, Glasgow

CONTENTS

1 INTRODUCTION

Biofluid-mechanics is a multidisciplinary science, the study of a certain class of biological problems from a fluid mechanics point of view. Through a combination of engineering and medical science, new applications of the computational fluid dynamics method were introduced, the most significant are to be found in patient care.

Complex movement of fluids in the cardiovascular system demand professional fluid mechanics skills. In comparison to machinery analysis, blood flow inside the human body can become very complex right from the start. Most assumptions and simplifications are unsatisfactory, for instance *Newtonian* fluids. Furthermore the geometry is, from an engineer's point of view, very irregular and complex. From a bionics point of view, it is fascinating and ingenious. Chapter 2 deals with methods and mathematical models, that are required to compute blood flow in arteries.

Advances in computational methods and three-dimensional imaging techniques allow improved understanding of haemodynamic flow in the cardiovascular network. Computational fluid dynamics (CFD), which solves differential equations of fluid flows numerically and is widely used in turbo machinery, is an excellent tool for analysing and displaying blood flow in the head and neck arterial network. In contrast to previous studies [1–4], using two or three-dimensional ideal geometry, this project deals with real geometry obtained from image-scan segmentation of a patient [5–9]. To set up a realistic model, mesh independence, various blood viscosity models and turbulence models has been studied in a steady CFD model, shown in chapter 3.

In cancer treatment using intra-arterial infusion, the knowledge about the chemical agent concentration in blood and the technique by which the tumours were infused is vital for therapy success [10, 11]. A two-component transient CFD model can assist medical scientists to select the most appropriate treatment strategy. This model is presented in chapter 4.

The influence of various parameters must be investigated. Chapter 5 provides advice for future research from the author's experience during this project.

1.1 Haemodynamic Flows

The cardiovascular circulatory system ensures the transport of nutrients, gases and hormones between organs of the human body. Blood circulation is driven

Table 1.1: Typical blood flow values, taken from [13, p. 79].

site	internal diameter (mm)	wall thickness (mm)	cross sectional area (mm^2)	peak velocity (m/s)	peak *Reynolds* number
ascending aorta	15	0.65	200	1.2	4500
carotid artery	5	0.3	20		
arteriole	0.5	0.02	$2 \cdot 10^{-3}$	0.0075	0.09
capillary	0.06	0.001	$3 \cdot 10^{-5}$	0.0007	0.001
venule	0.4	0.002	$2 \cdot 10^{-3}$	0.0035	0.035
vena cava	10	0.15	80	0.25	700

by the heart, which pumps roughly 5 l/min blood through the body, with just 1 W power, [12, p. 19]. The rate of flow can be increased by up to 20–30 l/min during physical exercise. The heart comprises two chambers, the left and right ventricles. During the cardiac cycle, the ventricles execute a periodic contraction and relaxation. As a result, the ventricle and aortic pressure changes periodically. The entire cycle can be divided into filling phase, contraction phase, evacuation phase and relaxation phase. Contraction and evacuation phase are known as systole (ventricle contraction), relaxation and filling phase as diastole (ventricle relaxation). The time period of systole is about 300 ms and approximately constant at each heart frequency, the time period of diastole varies significantly. The mean pressure of the leaving blood flow in the left ventricle is approximately 133 mbar. The pressure drops to roughly 13 mbar when the blood returns to the right ventricle. In the aorta, the pressure pulses between 120 mbar and 160 mbar around its mean value, which is known as systolic (maximum) and diastolic (minimum) pressure, [12, p. 23].

The blood circuit is divided into the pulmonary and systemic circulation. The aorta is the root of the systemic circulation. Blood flows through several arterial branches into the capillaries, where a proportion of oxygen is supplied to organs and carbon dioxide is absorbed. The flow in capillaries is also known as micro circulation, which is a comprehensive term for flow in small vessels, meaning arterioles capillaries and venules. Blood flows back into the heart through veins and is pumped into the pulmonary circulation for a renewed gas exchange. Table 1.1 provides an overview of typical vessel diameters and flow values.

The *Reynolds* number in arteries ranges from 100 to several thousand. This causes laminar flow in smaller arteries and transitional flow in larger arteries. A fully developed turbulent flow does not occur at any point during the cardiac cycle. This is mainly explainable by a too short time period for turbulent flow development. Because of vessel distensibility, the pulsatile flow becomes rather

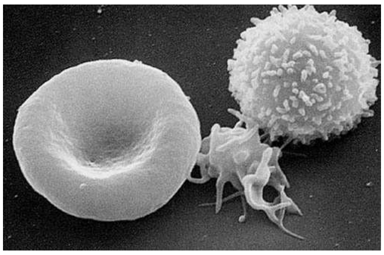

Figure 1.1: From left to right erythrocytes (red blood cell), thrombocytes (platelet) and leukocytes (white blood cell). Scanning electron microscope photograph, taken from [15].

steady with increasing distance from the heart. The aorta acts as a volume reservoir for the heart.

> "The smaller the branching of the arteries, the less the pulsing flow is noticeable." [14, p. 691]

At the aortic root, as well as after each arterial branch, the flow is initiated as intake flow, which means that in the greatest part of the arterial network fully developed flow is not present.

1.1.1 Blood

Blood is a mixture of liquid plasma 55 % and blood cells, which are erythrocytes (red blood cells), leukocytes (white blood cells) and thrombocytes (platelets), shown in Fig. 1.1.

Erythrocytes contain the blood's haemoglobin (iron containing oxygen transport metalloprotein) surrounded by a flexible red cell membrane and are responsible for oxygen transport in the whole circulatory system. They are biconcave-shaped and have roughly a diameter of 8.5 µm, a maximum thickness of 2.5 µm and a minimum thickness in the centre of about 1 µm, [16, p. 125]. In comparison with a spherical-shape, the biconcave-shape has a larger surface area at the same cell volume, which leads to a more efficient gas exchange. Due to the flexible membrane, erythrocytes can pass through capillaries with small diameters up to 5 µm by assuming a bent shape. Leukocytes play a major role in attacking infectious agents and are part of the human immune system. Thrombocytes are responsible for blood clotting, and this is visible after a skin injury. They convert fibrinogen into fibrin, which creates a mesh to collect erythrocytes, causing clotting. The proportion of all blood cells in the blood is called haematocrit value Ht and is normally about 45 %. Because erythrocytes represent the largest share of all blood cells with roughly 95 %,

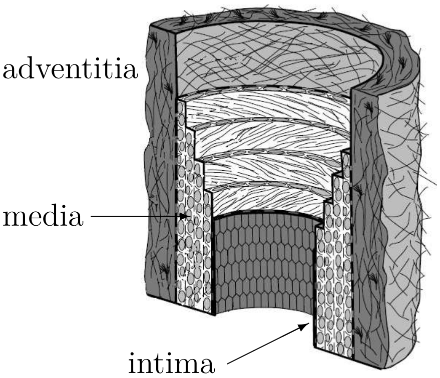

Figure 1.2: Schematic of the components of a healthy artery, taken from [23].

Ht mainly indicates the red blood cell concentration. The remaining shares of blood cells are 0.13 % leukocytes and 4.9 % thrombocytes.

Blood plasma is essentially a yellow aqueous solution containing 92 % water, 8 % blood plasma proteins, which are fibrinogen, globulin (a carrier of lipids), albumin and trace amounts of other materials, [16, p. 123]. Blood plasma without fibrinogen is called blood serum.

The viscosity of blood can be measured with capillary or rotatory viscometers, detailed in [17, pp. 220–223]. However, as soon as blood is removed from the body, clotting is initiated. Therefore an anticoagulant (a substance which prevents blood clotting) must be added, which is assumed to reduce the blood viscosity. Several factors influence the viscosity. Temperature has a significant impact and it is because of this fact, that it is kept at a constant value, preferably at body temperature. The viscosity increases with increasing haematocrit. Furthermore, the tube diameter influences the blood viscosity. In small diameter tubes the viscosity decreases. At tube diameters larger than approximately 0.5 mm, the viscosity approaches an asymptotic value. This effect is known as the *Fahraeus-Lindqvist* effect. This means that red blood cells are moving toward the centre in small tubes, and which results in a cell free wall layer and decreasing viscosity.

1.1.2 Vessels

Investigation in blood vessel mechanics and derivation of mechanical models is mainly a contribution by Fung [18–20] and Holzapfel [21–24].

The arterial wall is subdivided in three layers. From inside to outside they are called intima, media and adventitia, shown in Fig. 1.2. Each layer consists of varying amounts of the proteins elastin and collagen, vascular smooth muscle cells and extracellular matrix, [16, p. 152]. The innermost layer intima, which is the thinnest, comprises of endothelial cells and a lamina of elastin. The endothelial cells create a smooth wall for blood flow with a small wall friction. These cells are selectively permeable to water, electrolytes, sugars and other substances, and thus provide mass transport between the blood stream and the tissues. The middle layer media, comprises of circularly arranged elastin fibres, collagen and vascular smooth muscles. The outermost layer adventitia, provides the connection to surrounding structures by merging with them, and it also contains nerves.

The veins basic structure is similar to that of arteries. The relative wall thickness is thinner in comparison with arteries, because of the lower interior pressure level in veins and because the media contains very little elastic tissue.

> “The intimal surface of most larger veins has semilunar valves, generally arranged in pairs and associated with a distinct sinus or local widening of the vessel.” [18, p. 325–326]

Collagen fibres, which are present in media and adventitia, are much stiffer than elastin fibres, both produce a network. Although each component shows linear elastic properties, the combination of elastin and collagen fibres behave non-linearly and directionally. Because of this, soft tissue shows viscoelastic properties such as hysteresis, relaxation and conditioning, and these are briefly described in Section 2.7.

Measurements of vessel mechanics can only be made *in-vitro* (outside the living organism), for instance in uniaxial extension tests on strips of arteries cut in various orientations (most commonly circumferential and longitudinal). A second method is to apply an internal pressure to the vessels in their natural geometry and to measure the change in radius and wall thickness, to determine the load deformation behaviour. Angiographic (CT or MRI), ultrasonic or other imaging techniques are required to measure the radius and wall thickness. Conversely, these tests provide the basis for non-invasive indirect blood pressure measurements *in-vivo* (inside the living organism), as shown in [25, 26]. All tests have to be made in a physiological environment with controlled moisture, temperature and ionic content.

1.1.3 Implications for Patient Care

Haemodynamics play an essential role in patient care. In head and neck cancer treatment using chemotherapy, the chemical agent concentration is of major interest. The aim is to supply a high application rate of chemical in a specified target region inside the human body. Using intra-arterial infusion improved the success of treatment. This is because of the arteries that supply specific tissue, detailed in [11, 27, 28]. This technique allows the supply of much higher chemical agent concentration directly to the tumour than intra-venous infusion.

The latter, distributes the chemical agent throughout the whole body and causes increased side effects. Because of the patient specific artery geometry and resultant haemodynamics, there is no method that always leads to success, and this is discussed in [10]. Simulation of patient specific two-component flow, using various injection positions and parameters, for instance the mass flow rate of the chemical agent, should deepen the knowledge of chemical agent distribution in the artery network, which is the aim of this study. If an accurate computer simulation is achievable in a sufficiently short time, patient specific computation would provide the basis of comparing the effect of several treatment methods and parameters prior to therapy.

The thorough understanding of haemodynamics in blood vessels is of great interest in the pathophysiology of cardiovascular diseases. The success of several therapies depends on the knowledge of fluid flow values, such as wall shear stress, turbulence parameters and pressure. For instance in aneurysm therapy, a patient specific blood flow model, could assist medical scientists to select the most appropriate treatment strategy, dealt with in [6, 29]. It is desirable to compare different treatment methods, such as coiling or stent placement, using computational methods prior to human treatment, [30]. Several biomechanical factors influence aneurysm initiation, growth and rupture. The wall shear stress for instance is a major indicator in prediction of aneurysm rupture risk.

Turbulent flow, indicated by the turbulent kinetic energy, causes potential damage to red blood cells, known as haemolysis. Due to turbulence, the risk of thrombosis (blood clotting) increases, associated with the possible and catastrophic result of a stroke, [4]. An additional indicator for haemolysis of erythrocytes (red blood cells) in turbulent flow is the wall shear stress. The study in [31] shows, that on high stresses above 250 Pa, fragmentation of human erythrocytes occurs. Free haemoglobin content is increasing in the suspending medium. Red blood cell damage induced by artificial organs is dealt with in [32, 33], with a threshold of approximately 400 Pa for haemolysis caused by turbulent shear stress.

Acute vascular endothelial changes (vessel wall traumas) caused by high velocity gradients near the vessel wall is dealt with in [34]. It was found, that the acute yield stress is approximately 37.9 Pa. “Exposure to stress in excess of this value for periods as short as one hour resulted in [...] cell deformation, cell disintegration, and finally dissolution and erosion of cell substance.”

Finally the most prevalent cardiovascular disease is atherosclerosis, which involves the accumulation of lipid material (plaque) in the intima of arteries. The blood supply to vital organs like the brain, heart and lungs is disturbed, which can lead to stroke. The haemodynamic factors play a significant role in the localization of atherosclerosis, which is often present in artery bifurcations and bends caused by flow recirculation. A number of studies have shown that

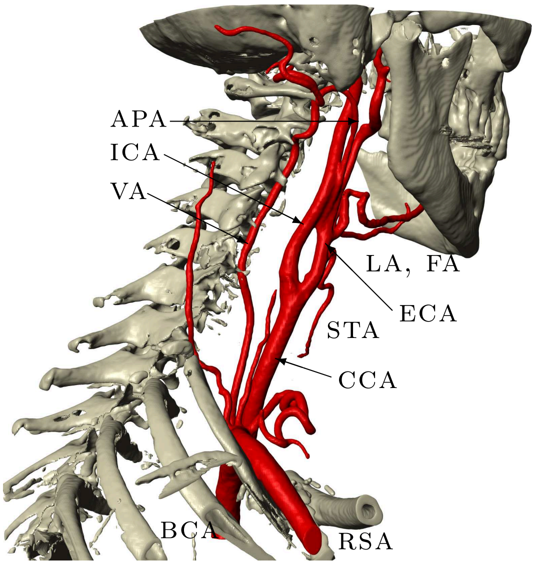

Figure 1.3: Right arterial network and skull volume model, using SCANIP.

there is a correlation between low wall shear stress and the progression of atherosclerotic lesions, [35–37].

The difference between image based and idealized CFD models is significant, which “[. . .] mask interesting hemodynamic features that may be of importance in understanding the localization of individual lesions.”, [8]. Taylor [5] is referring to various recent research papers in this topic.

1.2 Head and Neck Arteries

The main arteries of head and neck are presented in Fig. 1.3, which is the result of image segmentation described in Section 2.4. Connected to the aortic arch, the brachiocephalic artery (BCA) supplies the right shoulder and arm through the right subclavian artery (RSA) as well as the head and neck via the arising common carotid artery (CCA), which branches into the internal carotid artery (ICA) and the external carotid artery (ECA). The ICA ensures the main blood supply of the brain. The ECA branches several times and supplies the neck, face and tongue, mainly via the facial artery (FA) and lingual artery (LA).
The origin of the lingual artery was studied in 211 specimens in [38, p. 766]:

> “In 80 %, the superior thyrid, lingual and facial arteries arose separately, in 20 %, the lingual and facial arteries arose from a common stem inferiorly or high on the external carotid artery.”

Figure 1.3 belongs to the minority with a common stem of the FA and LA. Furthermore this Fig. shows just a selection of arteries, in reality there are even more branches and the arterial network is much finer, which is extensively shown in [38, 39].

1.3 Head and Neck Cancer Treatment

A general definition for cancer is given in [40, p. 97]:

> "Cancer is the general term for more than 100 different distinct diseases that can affect every part of the body. Cancer is defined by a rapid abnormal cell growth beyond usual boundaries that can affect adjoining parts of the body including other organs. This process is referred to as metastasis which is the major cause of death from cancer."

There are several influence factors, which play a significant role in cancer prevention, such as tobacco and alcohol use, exposure to sunlight and many more. There are mainly three common treatment methods; surgery, radiotherapy and chemotherapy and combinations of them. Early cancer detection is vital for treatment success.

In head and neck cancer treatment and particularly in oral cancer treatment, radiotherapy alone or in combination with chemotherapy is generally administered. Optionally, this is followed by surgery, leading to significant cosmetic and functional disabilities and a drastic reduction in life quality. The general aim is to approach maximum tumour control with minimum related side effects.

In recent years, chemotherapy has become more relevant and is now an important treatment component in combined modality approaches, several studies in this subject are summarized in [41, p. 127]. Studies, using concurrent chemoradiation in comparison with radiation alone, are commonly randomized trials, which vary in radiation dose, fractionation schedule, and administered chemotherapy. The dosage scheme, which is usually given in mass per body surface area $^{mg}/_{m^2}$, as well as the administration method of the chemical is vital for the prognosis. Intra-arterial injection via catheter in the tumour-feeding artery (lingual artery), comparing three different injection methods, is dealt with in [10]. As mentioned in Section 1.1.3, the advantage of intra-arterial injection is the selective chemical distribution; only the tumour region is supplied with a high concentration of chemical agent. In [11, 27] the infusion dose of cisplatin (anticancer chemical) was further increased by simultaneous infusion of a neutralizing agent (sodium thiosulfate) via a vein, which leads to superior control of regional cisplatin concentration.

> “However, as a catheter must be inserted every time an anticancer agent is injected, severe complications such as cerebral infarction and sudden death can occur.” [10]

Additional complications caused by catheter and adverse effects due to outflow of the anti cancer agent, are mentioned in [28], such as catheter dislocation, local inflammation and neurological complications, for instance headache and facial paresis.

In chemotherapy, various chemical agents are used in order to kill cancerous cells. A very effective drug is cisplatin, which is briefly described in Section 2.6.2. Since, several other cells divide rapidly in the human body, side effects such as hair loss appear.

1.4 Previous Project

A two dimensional CFD simulation with ideal geometry and steady flow condition was done in [42]. The geometry was set up in three different models with increasing complexity. The last and most detailed one included major arteries and veins of the head and neck as a pipe system. Blood was set as a *Newtonian* fluid. Two phase flow is considered using the VOF (volume of fluid) model. A case study was made with various blocked veins to examine the chemical agent distribution after injection at one specific artery.

The present study distinguishes from the previous project strongly. The step into the third dimension requires different procedures in most simulation stages.

2 SIMULATION OF BLOOD FLOW

Computational fluid dynamics is a powerful simulation tool for system analysis involving fluid flow, heat transfer, combustion and associated phenomena such as chemical reactions. The basic idea is the subdivision of a not analytically solvable complex domain, into a number of smaller, non-overlapping sub domains. This is known as meshing. Conservation equations, in particular the *Navier-Stokes* equations in fluid dynamics (2.2), are solved numerically, which means this procedure always leads to an approximative result. The whole theory and numerics is brilliantly described in detail in numerous books, for instance in [43–46]. And because of this, it was decided to skip the CFD fundamentals in this report. However, this chapter deals partly with CFD topics, that are required in blood flow simulation. The other part describes analytical models and relevant measured data.

2.1 Basic Mathematical Models

Several different notation methods are common in fluid mechanics. For a *Cartesian* coordinate system in Fig. 2.1 with directions (x, y, z), the velocity of a fluid can be written as a vector $\vec{u}$ (2.1). In computational fluid mechanics it is more common to use the index notation with numbers $(1, 2, 3)$. Sometimes it is more convenient to use letters (i, j, k). These different ways of referring to velocity components and directions will be used interchangeably. A tensor is characterized by two over bars. One over bar means time averaged.

$$\vec{u} = \begin{pmatrix} u \\ v \\ w \end{pmatrix} = \begin{pmatrix} u_1 \\ u_2 \\ u_3 \end{pmatrix} = \begin{pmatrix} u_i \\ u_j \\ u_k \end{pmatrix} \tag{2.1}$$

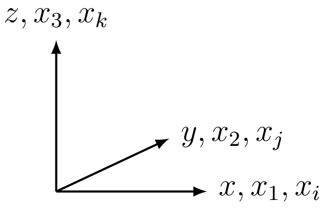

Figure 2.1: *Cartesian* coordinate system.

2.1.1 Navier-Stokes Equations

The basic equations for all *Newtonian* flows are conservations of mass, momentum and energy, which were independently derived from Claude Louis Marie Henri Navier and George Gabriel Stokes. The *Navier-Stokes* equations for constant density are given by (2.2) with $a = \lambda/(\rho \cdot c_p)$, meaning thermal conductivity λ, density ρ, specific heat capacity c_p, temperature T, pressure p and the kinematic viscosity ν. The first equation is conservation of mass, the next three are conservations of momentum and the last is conservation of energy. It is a system of five partial differential equations with five unknowns. There are many forms of the *Navier-Stokes* equations, for instance compressible flow, cylindrical coordinate systems and turbulent flow (2.53). Additionally, it is common to shorten theses equations by using *Nabla* and *Laplace* operators, or write them in integral form.

$$
\begin{aligned}
\frac{\partial u}{\partial x} + \frac{\partial v}{\partial y} + \frac{\partial w}{\partial z} &= 0, \\
\frac{\partial u}{\partial t} + u\frac{\partial u}{\partial x} + v\frac{\partial u}{\partial y} + w\frac{\partial u}{\partial z} &= -\frac{1}{\rho}\frac{\partial p}{\partial x} + \nu\left(\frac{\partial^2 u}{\partial x^2} + \frac{\partial^2 u}{\partial y^2} + \frac{\partial^2 u}{\partial z^2}\right), \\
\frac{\partial v}{\partial t} + u\frac{\partial v}{\partial x} + v\frac{\partial v}{\partial y} + w\frac{\partial v}{\partial z} &= -\frac{1}{\rho}\frac{\partial p}{\partial y} + \nu\left(\frac{\partial^2 v}{\partial x^2} + \frac{\partial^2 v}{\partial y^2} + \frac{\partial^2 v}{\partial z^2}\right), \\
\frac{\partial w}{\partial t} + u\frac{\partial w}{\partial x} + v\frac{\partial w}{\partial y} + w\frac{\partial w}{\partial z} &= -\frac{1}{\rho}\frac{\partial p}{\partial z} + \nu\left(\frac{\partial^2 w}{\partial x^2} + \frac{\partial^2 w}{\partial y^2} + \frac{\partial^2 w}{\partial z^2}\right), \\
\frac{\partial T}{\partial t} + u\frac{\partial T}{\partial x} + v\frac{\partial T}{\partial y} + w\frac{\partial T}{\partial z} &= a\left(\frac{\partial^2 T}{\partial x^2} + \frac{\partial^2 T}{\partial y^2} + \frac{\partial^2 T}{\partial z^2}\right).
\end{aligned}
\tag{2.2}
$$

2.1.2 Steady Pipe Flow

All following described fundamental fluid equations are inappropriate for computing pulsatile pipe flow. But they can be used for a quick prediction of time averaged flow values, which is often reasonable. There are many simplifications that arise from the *Navier-Stokes* equations. One method is to reduce the spatial expansion. In two dimensional cylindrical pipes on laminar *Reynolds* numbers, the *Navier-Stokes* equations become the *Hagen-Poiseuille* equation, derived in Section 2.3. The velocity profile on laminar flow, shown in Fig. 2.2, is a parabolic function of the radius r, inner pressure p_i and dynamic viscosity μ, with the maximum velocity $w_{max} = w(0)$ at the pipe axis (2.3).

$$
w(r) = -\frac{1}{4\mu}(r_a^2 - r^2)\frac{\mathrm{d}p_i}{\mathrm{d}z} \quad w_{mean} = \frac{w_{max}}{2}
\tag{2.3}
$$

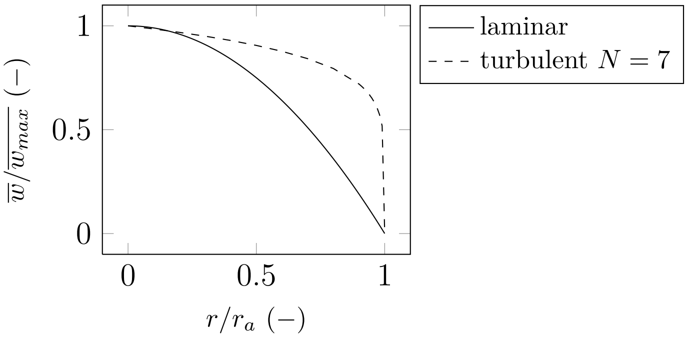

Figure 2.2: Dimensionless velocity profile for laminar and turbulent flow as a function of the dimensionless pipe radius.

It is impossible to solve the velocity profile analytically on turbulent *Reynolds* numbers. Hence, empirical relations were obtained from experiments. The time averaged velocity as function of the radius is given by (2.4). N is a function of the *Reynolds* number and for $Re = 10^5$, the distribution exponent N becomes 7. The function $N = N(Re)$ is shown in [47, p. 201]. The turbulent velocity profile in Fig. 2.2 is flatter than the laminar function.

$$\begin{aligned} \overline{w(r)} &= \overline{w_{max}} \left(\frac{r}{r_a}\right)^{(1/N)}, \\ \frac{\overline{w_{mean}}}{\overline{w_{max}}} &= \frac{2N^2}{(N+1)(2N+1)}. \end{aligned} \tag{2.4}$$

Furthermore, it is common to reduce pipe flows to only one dimension and calculate with cross sectional averaged fluid values. Assuming viscous forces are negligible, the *Bernoulli* equation is given by (2.5), z means the height and u_{mean} is the mean velocity along the pipe length direction. It is an energy equation and widely used in technical pipe systems with additional loss and source terms.

$$p + \frac{1}{2} \cdot \rho \cdot u_{mean}^2 + \rho \cdot g \cdot z = \text{const} \tag{2.5}$$

Equations (2.3) and (2.4) are only valid for fully developed pipe flows. That is at a certain distance in a straight smooth-surfaced tube, far enough from the entrance, so that any upstream disturbances have dissipated. This distance is called entrance length. The entrance length for high *Reynolds* numbers is defined by (2.6), with the hydraulic diameter d_h, dealt with in [12, p. 230].

$$l_e = 0.03 \cdot d_h \cdot Re \tag{2.6}$$

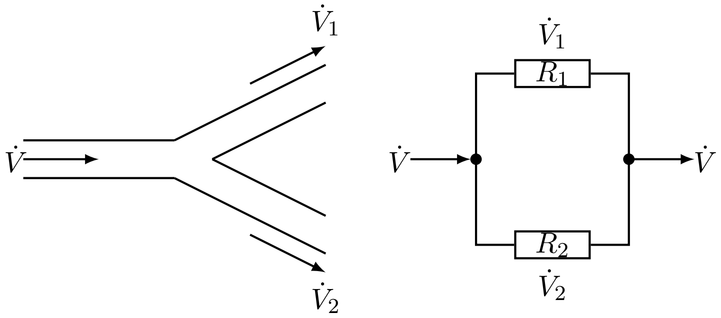

Figure 2.3: Arterial bifurcation.

In contrast in [16, p. 39] the entrance length for turbulent flows l_e is estimated with (2.7) and for laminar flows with (2.8).

$$l_e = 0.693 \cdot d_h \cdot Re^{1/4} \tag{2.7}$$

$$l_e = 0.06 \cdot d_h \cdot Re \tag{2.8}$$

The arterial network subdivides large arteries into small vessels through numerous bifurcations. It is convenient to introduce the hydraulic resistance R, analogous to resistance in electrical circuits. The pressure drop is equivalent to the voltage $\Delta p \equiv \mathcal{U}$ and the rate of flow to the current $\dot{V}^2 \equiv \mathcal{I}$. Hence, the hydraulic resistance is $R = \Delta p / \dot{V}^2$, [48, p. 135]. Figure 2.3 shows an artery bifurcation and the equivalent model with hydraulic resistance.

Using the friction coefficient $\lambda_r = 64/Re$ for laminar *Reynolds* numbers, conservation of mass $\dot{V} = \sum_{i=1}^{n} \dot{V}_i$ and assuming $\Delta p_1 = \Delta p_2 = \text{const.}$, the pressure drop yields to (2.9), with the pressure loss coefficient ξ and the overall length L for each pipe segment.

$$\Delta p = R \cdot \dot{V}^2 = \frac{8\rho}{\pi} \frac{\dot{V}^2}{\left[\sum\limits_{i=1}^{n} \sqrt{\dfrac{{d_{hi}}^4}{\xi_i + \lambda_{ri} \dfrac{L_i}{d_{hi}}}} \right]^2} \tag{2.9}$$

The rate of flow for each segment is defined by (2.10).

$$\dot{V}_i = \sqrt{\frac{\Delta p}{R_i}} \quad \text{with} \quad R_i = \frac{8}{\pi^2} \frac{\rho}{{d_{hi}}^4} \left(\xi_i + \lambda_{ri} \frac{L_i}{d_{hi}} \right) \tag{2.10}$$

2.1.3 Pulsatile Pipe Flow

Blood flow is pulsatile, which means a special type of transient flow. Velocity and pressure functions vary periodically, driven by the cardiac cycle. The heart contracts during systole and, due to the artery elasticity, a pressure wave originates from the left ventricle and travels through the aorta. Due to the compliant nature of arteries, the wave speed is much faster than the flow velocity. Similar to sound waves, wave reflection and transmission occur at artery branches. The pulsatile flow characteristic influences the pressure distribution out in the arteries, the velocity profiles and the critical *Reynolds* number when transition from laminar to turbulent flow occurs. The flow accelerates rapidly during early systole in the aorta. This stabilizes the flow and enhances the transitional point compared with steady flow. The second reason for laminar flow during systole in the aorta is; there is insufficient time for turbulence to develop. The triggering mechanism, for instance surface roughness or vibration, exists for a limited time and then reverses.

> “Therefore, in a healthy artery, turbulence is generally absent because the flow destabilization time interval (mid-to-end systole) is short $t \approx 150\,\mathrm{ms}$ and is immediately followed by diastole when the velocity and instantaneous *Re* are low.” [16, p. 43]

The equivalent to the *Reynolds* number in steady flow is the *Womersley* number in pulsatile flow (2.11), with the heart rate ω_h, which provides a comparison between unsteady inertial forces and viscous forces. When $\alpha_W < 1$, viscous forces dominate in every region in the tube and the flow is known as quasi-steady flow. Womersley derived the mathematical expressions to compute pulsatile flow in compliant arteries using frequency parameters and Bessel functions [49].

$$\alpha_W = \frac{d_h}{2}\sqrt{\frac{\rho \cdot \omega_h}{\mu}} \tag{2.11}$$

Arteries can be modelled as thin walled elastic tubes. The simplest kind of wave speed equation, using *Hooke’s* law, is the *Moens-Kortweg* formula, given by (2.12) [13, p. 107], with wall thickness h and the modulus of elasticity E.

$$c = \sqrt{\frac{E \cdot h}{2 \cdot \rho \cdot r}} \tag{2.12}$$

Figure 2.4 shows an arterial bifurcation with pulsatile blood flow and the equivalent alternating current model for one single ductile tube. Reflection and transmission of pressure and rate of low waves occur at junctions in the arterial

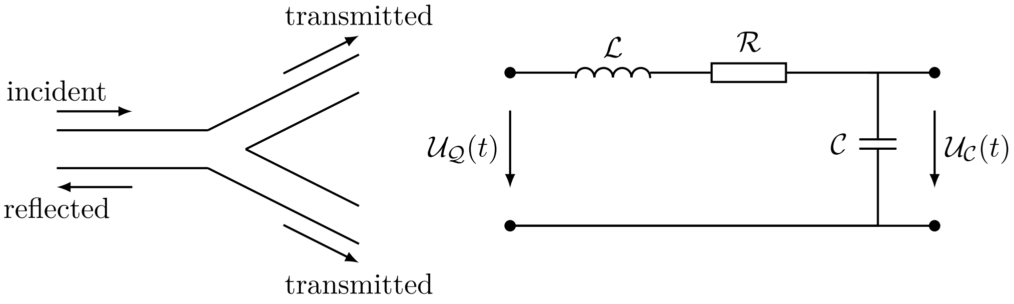

Figure 2.4: Arterial bifurcation with pulsatile flow. The equivalent electrical model on the right substitutes one single tube and is taken from [50].

network. Hence, the pressure and rate of flow is superposed (2.13), with index I-incident wave, R-reflected wave and $T1, 2$-transmitted waves. The left hand side represents the flow out of the parent tube and the right hand side the flow into two daughters.

$$\begin{aligned} p_I + p_R &= p_{T1} = p_{T2}, \\ \dot{V}_I - \dot{V}_R &= \dot{V}_{T1} + \dot{V}_{T2}. \end{aligned} \tag{2.13}$$

The relationship between pressure and velocity waves in positive x-direction is $p = \rho \cdot c \cdot u$. With $\dot{V} = A \cdot u_{mean}$, the flow-pressure relationship can be written as (2.14) with the cross sectional area A. The $+$ sign applies if the wave goes in positive axis direction and the $-$ sign applies if the wave goes the opposite way.

$$\dot{V} = \pm \frac{A}{\rho \cdot c} p \tag{2.14}$$

The quantity $\rho c / A$ is the characteristic impedance of the tube and is denoted by the symbol Z, which is also the ratio of oscillatory pressure to oscillatory flow when the wave goes in positive axis direction (2.15).

$$Z = \frac{\rho \cdot c}{A} = \frac{p}{\dot{V}} \tag{2.15}$$

The ratio of reflected to incident wave is called reflection factor (2.16), the transmission factor is the ratio of transmitted to incident wave (2.17).

$$\mathbb{R} = \frac{p_R}{p_I} \tag{2.16}$$

$$\mathbb{T} = \frac{p_{T1}}{p_I} = \frac{p_{T2}}{p_I} \tag{2.17}$$

Table 2.1: Electrical values for pulsatile pipe flow in compliant tubes from various references.

reference	$\mathcal{R}$	$\mathcal{L}$	$\mathcal{C}$
[50]	$\frac{8\mu l}{\pi r^4}$	$\frac{\rho l}{\pi r^2}$	$\frac{3\pi r^2 l}{2Eh}$
[51]	$\frac{81\mu l}{8\pi r^4}$	$\frac{9\rho l}{4\pi r^2}$	$\frac{3\pi r^3 l}{2Eh}$
[53]	$\frac{8\mu l}{\pi r^4}$	$\frac{9\rho l}{4\pi r^2}$	$\frac{3\pi r^3 l}{2Eh}$
[56]	$\frac{8\pi\mu l}{\pi^2 r^4}$	$\frac{\rho l}{\pi r^2}$	$\frac{2\pi r^3 l}{Eh}$

The electrical model in Fig. 2.4 on the right, is based on the one-dimensional form of the *Navier-Stokes* equations. Due to the similarity to propagating electromagnetic wave equations, a compliant tube can be mathematically modelled by a segment of electrical transmission line.

Modelling the whole arterial network is an issue in numerous research papers [50–55] and in books [56, pp. 309–320], [17, pp. 347–394]. All are based on the electrical analogue of flow in vessels, where pressure is equal to voltage $p \equiv \mathcal{U}$, the rate flow to current $\dot{V} \equiv \mathcal{I}$, viscous drag to resistance $\mathcal{R}$, compliance to capacitance $\mathcal{C}$ and mass to inductance $\mathcal{L}$. Using single electrical oscillator models and interconnecting them to a complex system, creates the preconditions for calculating pressure and rate of flow wave forms for every point in the arterial network.

There are different approaches for determining the electrical values $\mathcal{R}$, $\mathcal{C}$ and $\mathcal{L}$ for the arterial tube segments, shown in Tab. 2.1. It is common to use the CGS-system (centimetre gram second) to directly obtain the electrical units ohm, henry and farad.

Signal processing is a convenient method, for treating arterial pressure and rate of flow waves, by converting the electric circuit with *Laplace* transformation in transfer functions [56, pp. 317–318]. Using *Kirchhoff's* laws and the complex equations for resistor $\mathcal{U}(t) = \mathcal{R} \cdot \mathcal{I}(t)$, inductor $\mathcal{U}(t) = \mathrm{j}\omega\mathcal{L} \cdot \mathcal{I}(t)$ and capacitor $\mathcal{I}(t) = \mathrm{j}\omega\mathcal{C} \cdot \mathcal{U}(t)$, the transfer function for one arterial segment is derived in (2.18), with the complex number j, the complex argument s and here ω means the frequency. Combining transfer functions in parallel (addition) or in series

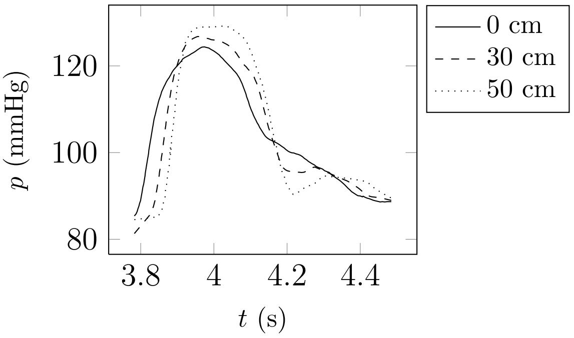

Figure 2.5: Aorta pressure wave forms at various distances from the aortic root computed by the model of Olufsen [55].

(multiplication) yields to a total arterial system.

$$
\begin{aligned}
\mathcal{U}_{\mathcal{Q}}(t) &= \mathcal{U}_{\mathcal{R}}(t) + \mathcal{U}_{\mathcal{L}}(t) + \mathcal{U}_{\mathcal{C}}(T), \\
&= \mathcal{R} \cdot \mathcal{I}(t) + \mathrm{j}\omega\mathcal{L} \cdot \mathcal{I}(t) + \mathcal{U}_{\mathcal{C}}(t), \\
&= \mathcal{R} \cdot \mathrm{j}\omega\mathcal{C} \cdot \mathcal{U}_{\mathcal{C}}(t) + (\mathrm{j}\omega)^2\mathcal{L}\mathcal{C} \cdot \mathcal{U}_{\mathcal{C}}(t) + \mathcal{U}_{\mathcal{C}}(t), \\
&= \mathcal{U}_{\mathcal{C}}(t)[\mathcal{R}\mathcal{C}\mathrm{j}\omega + (\mathrm{j}\omega)^2\mathcal{L}\mathcal{C} + 1], \\
\frac{\mathcal{U}_{\mathcal{C}}(t)}{\mathcal{U}_{\mathcal{Q}}(t)} &= \frac{1}{\mathcal{R}\mathcal{C}\mathrm{j}\omega + \mathcal{L}\mathcal{C}(\mathrm{j}\omega)^2 + 1} \quad \circ\!\!-\!\!\!\bullet, \\
H(s) &= \frac{1}{s^2\mathcal{L}\mathcal{C} + s\mathcal{R}\mathcal{C} + 1}. \qquad (2.18)
\end{aligned}
$$

Figure 2.5 shows pressure waveforms alongside the aorta. Phase shift and increasing peak pressure with increasing distance from the aortic root are visible. The mean pressure decreases, which is difficult to observe, because of the small pressure drop along the aorta.

The above described one dimensional models are required to offer adequate boundary conditions in CFD simulations, where it is often complex to obtain measured data. A constant pressure or resistance outflow condition, which is widely used in blood flow simulations, neglects pressure wave propagation and phase shift. This results in inaccurate pressure values [5, 57].

2.2 Model Simplifications

In image-based CFD blood flow simulations inside human vessels, the most common simplification is the rigid wall assumption. This assumption is mainly due to a lack of elasticity and wall thickness information required to model compliant walls [6, 7, 30, 58]. Other reasons are a lack of software packages, that can deal with fluid structure interaction (FSI), their very high price and too few computational resources. In the most contemporary available commercial mesh generation packages, vessel wall modelling from image data is not included. This approval is more or less admissible depending on the region inside the cardiovascular system. Obviously, it is not feasible for the heart and adjacent arteries.

The carotid artery bifurcation is probably the most studied region, using computational fluid dynamics. The effect of wall distensibility on arterial flow patterns has been investigated by many researchers. Steinman [8] mentions: “[. . .] the wall distensibility has only a minor effect on the distribution of wall shear stress [. . .]”. However, the quantitative value is influenced. Further evidence for the rigid wall simplification for carotid arteries is found in [59], where it is concluded that:

> “Flow simulations have been carried out under the rigid wall assumption and for the compliant wall, respectively. Comparison of the results demonstrates the quantitative influence of the vessel wall motion. [. . .] but the global characteristics of the flow and stress patterns remained unchanged.”

Perktold [60] summarizes for a numerical model of the carotid artery bifurcation:

> “With respect to the quantities of main interest, it can be seen, that flow separation and recirculation slightly decrease in the sinus and somewhat increase in the bifurcation side region, and the wall shear stress magnitude decreases by 25 % in the distensible model. The global structure of the flow and stress patterns remains unchanged.”

Experimental studies with similar conclusions are referred to in [8, 59].

Fully coupled FSI models, that model the interaction between blood flow and deforming vascular structure, are still one of the major challenges in image-based simulations, [5]. In contrast to former studies it is known that *in-vivo* measured boundary conditions, geometry, tissue properties and wall movement are required to adjust all the parameters for realistic FSI models. The recent papers of [9, 61, 62] show the high complexity in these matters.

The main aim is not to investigate accurate wall shear stress values in this study. Rather, the distribution of the chemical agent during injection into the head and neck artery network is of main interest. From the above mentioned studies it can be concluded, that the influence of a distensible model seems minor for the general characteristics of flow pattern. An influence study of moving walls would require efforts similar to this project and seems to be inoperable in this case. However such a study is described, using an ideal pipe model of the carotid artery and an self written MATLAB software, in Section 2.3.

Apart from the rigid wall condition, it is also necessary to restrict the geometry. The voxel resolution during the image segmentation process in SCANIP is with the used image data $x \times y \times z = 0.48828 \ \times 0.48828 \ \times 0.5\,\mathrm{mm}$. A voxel is the smallest three dimensional spatial unit, usually a cube and analogous to a pixel in two dimensions. Depending on image data quality and resolution there exists a lower limit for creating arterial tube geometry. In this study, the smallest artery diameter, that is possible to generate, is approximately 2 mm. Because of this, micro circulation in arterioles and capillaries is excluded in the simulation.

2.3 Fluid Structure Interaction

Fluid structure interaction problems are generally very complex, due to freely moving structures and often large deformations. Two sets of partial differential equations are coupled on the moving interface that separates the fluid and solid component. The *Navier-Stokes* equations are typical in *Eulerian* coordinates, in contrast to the momentum and equilibrium equations, which are typical in *Lagrangian*. One method is to use the arbitrary *Euler-Lagrange* equations (ALE).

> "The ALE is an effective way to treat FSI problems. Instead of using either a single *Lagrangian* approach or a single *Eulerian* approach, the ALE describes the motion of fluid in a moving reference frame whose velocity is almost arbitrary with the sole constraint that the velocity on the fluid-solid boundary must equal to that of the boundary." [63, p. 143]

It is omitted to give the whole set of ALE equations, which are extensively explained in [17, 63, 64].

In the most technical pipe flows, FSI is negligible due to the high stiffness of the pipe wall material, which is often steel. A blood vessel is an elastic tube. The blood pressure distends the vessel wall, hence the boundary shape changes and the fluid flow depends on the pressure drop and the wall stiffness. This is a coupled problem, that comprises a solid mechanics and a fluid mechanics part. The differential equations can be solved analytically for basic geometries. Figure 2.6 shows a cylindrical blood vessel with laminar and steady flow. The flow is maintained by a pressure gradient in z direction. Linear elasticity and *Newtonian* fluid are assumptions for simplifying the model.

The velocity is a function of x and y direction, $w = w(x, y)$, $u = 0$, $v = 0$. The *Navier-Stokes* equations for incompressible *Newtonian* flow are condensed in a compact form for pipe flow (2.19), dealt with in [13, p. 83].

$$\frac{\partial^2 w}{\partial x^2} + \frac{\partial^2 w}{\partial y^2} = \frac{1}{\mu}\frac{\mathrm{d}p_i}{\mathrm{d}z} \tag{2.19}$$

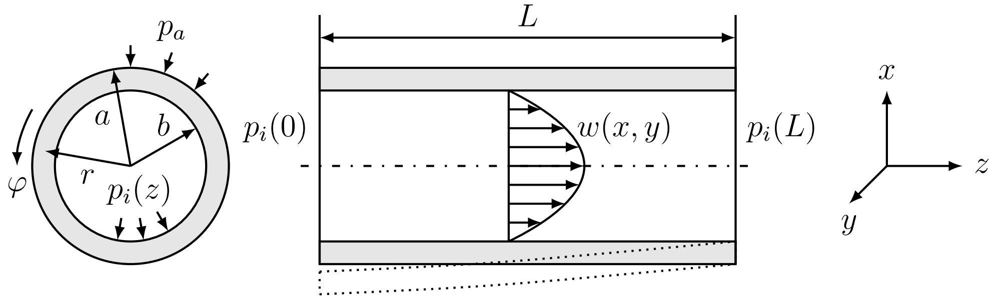

Figure 2.6: Elastic pipe flow in a blood vessel. On the left; the solid mechanics model, two dimensional with plain strain assumption and polar coordinate system. On the right; the fluid mechanics model, three dimensional in *Cartesian* coordinates. Coordinate transformation $r^2 = x^2 + y^2$, $z = z$. The flow is laminar, hence the velocity profile is a parabola. The dotted line below shows the deformed boundary shape after considering fluid structure interaction, $p_i(L) < p_i(0)$.

Here, $\mathrm{d}p_i/\mathrm{d}z$ is a constant. In cylindrical polar coordinates with $r^2 = x^2 + y^2$ and the assumption that the flow is symmetric (2.19) becomes.

$$\frac{1}{r}\frac{\mathrm{d}}{\mathrm{d}r}\left(r\frac{\mathrm{d}w}{\mathrm{d}r}\right) = \frac{1}{\mu}\frac{\mathrm{d}p_i}{\mathrm{d}z} \tag{2.20}$$

After integration the velocity is determined by (2.21) with the constants C_0 and C_1. They are obtained by the non-slip boundary conditions and symmetry on the centre line $w(r=b)=0$, $\mathrm{d}w/\mathrm{d}r = 0$ at $r = 0$.

$$w(r) = \frac{1}{\mu}\frac{r^2}{4}\frac{\mathrm{d}p_i}{\mathrm{d}z} + C_0 \log r + C_1 \tag{2.21}$$

The solution is determined by (2.22). It is the parabolic velocity profile of the *Hagen-Poiseuille* flow.

$$w(r) = -\frac{1}{4\mu}(b^2 - r^2)\frac{\mathrm{d}p_i}{\mathrm{d}z} \tag{2.22}$$

The rate of flow is obtained by integration through the tube.

$$\dot{V} = 2\pi\int_0^b w \cdot r \cdot \mathrm{d}r \qquad = -\frac{\pi b^4}{8\mu}\frac{\mathrm{d}p_i}{\mathrm{d}z} \tag{2.23}$$

The mean velocity is obtained by dividing the rate of flow by the cross sectional area.

$$w_{mean} = -\frac{b^2}{8\mu}\frac{\mathrm{d}p_i}{\mathrm{d}z} \tag{2.24}$$

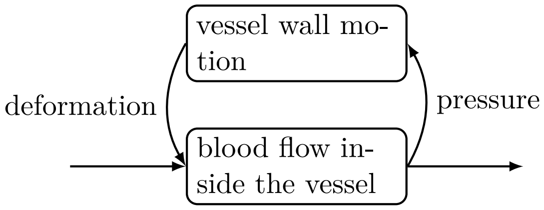

Figure 2.7: Fluid structure interaction in a vessel as a feedback system of fluid mechanism and solid mechanism.

With rigid walls b is a constant in (2.23). For solving a coupled flow with structure interaction, b has to be determined by the pressure. Hence $b = b(p_i(z))$ or shortened to $b = b(z)$. The solution of a coupled problem is much more complicated, because of the opposite influence of fluid-solid and solid-fluid. The mass conservation has to be fulfilled $\dot{m} = \rho \cdot A \cdot w_{mean}$. With a constant density, the rate of flow has to be constant, here it is $\dot{V} = A \cdot w_{mean}$. In other words, the rate of flow gradient has to be zero $\partial \dot{V}/\partial z = 0$. With a moving wall $b = b(z)$, the only remaining variable in (2.23) is the pressure drop $\mathrm{d}p_i/\mathrm{d}z$. An iterative method is required, and this leads to an equilibrium shown in Fig. 2.7.

An assumption for calculating the solid mechanics part is *Hooke's* law, meaning linear elastic solid mechanics. In reality the vessel tissue has a non-linear elasticity, dealt with in Section 2.7. With the Bi potential equation $\Delta\Delta F = 0$, dealt with in [65, p. 61] for axially symmetric geometry, the general solution for a thick walled cylinder in polar coordinates becomes,

$$F = C_0 + C_1 \ln r + C_2 r^2 + C_3 r^2 \ln r \tag{2.25}$$

$C_0 \ldots C_3$ are integration constants. With $\partial F/\partial \varphi = 0$ the stresses are defined by (2.26).

$$\begin{aligned} \sigma_r &= \frac{1}{r}\frac{\mathrm{d}F}{\mathrm{d}r} = \frac{C_1}{r^2} + 2C_2 + C_3(1 + 2\ln r), \\ \sigma_\varphi &= \frac{\mathrm{d}^2F}{\mathrm{d}r^2} = -\frac{C_1}{r^2} + 2C_2 + C_3(3 + 2\ln r), \\ \tau_{r\varphi} &= 0. \end{aligned} \tag{2.26}$$

With $C_3 = 0$, which means no asymmetric displacement and the boundary conditions $\sigma_r(a) = -p_a$ and $\sigma_r(b) = -p_i$, the constants C_1 and C_2 are given by (2.27).

$$C_1 = \frac{a^2b^2(p_a - p_i(z))}{a^2 - b^2} \quad C_2 = \frac{b^2p_i(z) - a^2p_a}{2(a^2 - b^2)} \tag{2.27}$$

The axial stress is obtained by $\sigma_z = \nu_p(\sigma_r + \sigma_\varphi)$. With the correlation computations of plain strain $E \rightarrow E/(1-{\nu_p}^2)$, $\nu_p \rightarrow \nu_p/(1-\nu_p)$, the radial strain $E \cdot \epsilon_r = \sigma_r - \nu_p \cdot \sigma_\varphi$ and the circumferential strain $E \cdot \epsilon_\varphi = \sigma_\varphi - \nu_p \cdot \sigma_r$ are computed. The resulting stresses and strains are shown in (2.28).

$$
\begin{aligned}
\sigma_r(r,z) &= \frac{a^2b^2(p_a - p_i(z))}{(a^2-b^2)r^2} - \frac{a^2p_a - b^2p_i(z)}{a^2-b^2},\\
\sigma_\varphi(r,z) &= \frac{-a^2b^2(p_a - p_i(z))}{(a^2-b^2)r^2} - \frac{a^2p_a - b^2p_i(z)}{a^2-b^2},\\
\sigma_z(r,z) &= \frac{-2(a^2p_a - b^2p_i(z)\nu_p}{a^2-b^2},\\
\epsilon_r(r,z) &= \frac{a^2b^2(\nu_p+1)(p_a - p_i(z))}{(a^2-b^2)Er^2} + \frac{(a^2p_a - b^2p_i(z))(\nu_p+1)(2\nu_p-1)}{(a^2-b^2)E},\\
\epsilon_\varphi(r,z) &= \frac{(a^2p_a - b^2p_i(z))(\nu_p+1)(2\nu_p-1)}{(a^2-b^2)E} - \frac{a^2b^2(\nu_p+1)(p_a - p_i(z))}{(a^2-b^2)Er^2},\\
\tau_{r\varphi}(r,z) &= 0 \quad \epsilon_z(r,z) = 0.
\end{aligned}
\tag{2.28}
$$

In the first step the pressure p_i is a variable, given by the linear pressure drop equation $p_i(z) = ([p_i(L) - p_i(0)]/L)z + p_i(0)$. Hence, all stresses and strains in (2.28) are also dependent on z, $\sigma_r = \sigma_r(r,z)$, $\sigma_\varphi = \sigma_\varphi(r,z)$, $\epsilon_r = \epsilon_r(r,z)$, $\epsilon_\varphi = \epsilon_\varphi(r,z)$. The circumferential strain is the ratio between radial displacement by original radius (2.29), in this case the original radius is b.

$$
\epsilon_\varphi = \frac{U_r}{r} = \frac{b(z)-b}{b} = \frac{b(z)}{b} - 1 \tag{2.29}
$$

The result for the variable inner radius $b(z)$ at $r = b$, which means the deformed wall shape, is given by (2.30).

$$
\begin{aligned}
b(z) = (\epsilon_\varphi + 1)b = \Bigg[&\frac{(a^2p_a - b^2p_i(z))(\nu_p+1)(2\nu_p-1)}{(a^2-b^2)E} - \\
&\frac{a^2b^2(\nu_p+1)(p_a - p_i(z))}{(a^2-b^2)Eb^2} + 1\Bigg]\, b
\end{aligned}
\tag{2.30}
$$

In contrast to a rigid wall proposition (2.22), the velocity profile is dependent on z, due to the moving wall $b = b(z)$ and the non linear pressure drop $\mathrm{d}p_i/\mathrm{d}z$.

$$
w(r,z) = -\frac{1}{4\mu}\left(b(z)^2 - r^2\right)\frac{\mathrm{d}p_i}{\mathrm{d}z} \tag{2.31}
$$

To estimate the influence of FSI on fluid flow characteristics in head and neck arteries, a MATLAB program was written, presented in Section A.1. A two

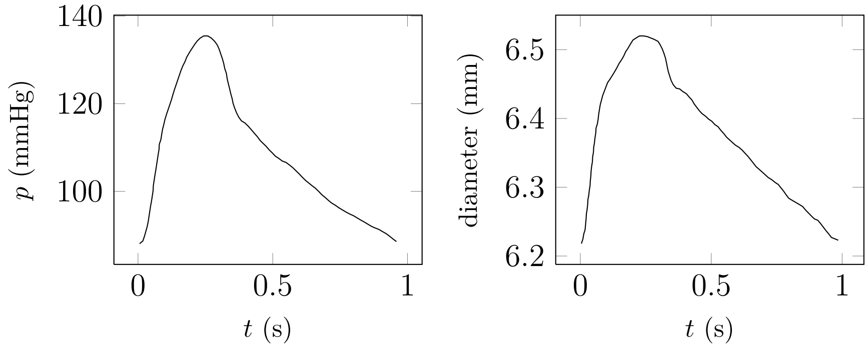

(a) Pressure.

(b) Diameter.

Figure 2.8: Common carotid artery pressure and diameter waveforms [26]. The systolic pressure is 135 mmHg the diastolic pressure is 88 mmHg, 1 mmHg ≈ 133.322 Pa.

dimensional axisymmetric cylindrical pipe is divided in finite differences along the pipe length and along the pipe radius for the fluid and solid continuum, respectively. Conservation of rate of flow is the principle point in the program. As shown in Fig. 2.7 the fluid continuum is solved by (2.23), the inner pressure $p_i(z)$ acts as boundary condition for the solid continuum, solved by (2.28). Obtaining the wall shape by (2.30) the pressure is adjusted so that $\mathrm{d}\dot{V}/\mathrm{d}z = 0$, which means constant rate of flow at each point in the fluid region. The new pressure distribution influences the wall shape and so on.

Figure 2.8 shows a simultaneous measured pressure and diameter waveform of the CCA, which is statistically analysed in 2026 subjects [26]. The CCA mean diameter is 6.2 mm, systolic and diastolic pressure difference is used as boundary condition range for the pipe inlet.

In the MATLAB program the pressure drop along the pipe length $p_i(L) - p_i(0)$ is assumed to be constant for each inlet pressure with 300 Pa. The pipe wall thickness is set with 0.5 mm, which is a typical value for the CCA [59]. The modulus of elasticity was adjusted to $E = 7.5 \cdot 10^5\,\mathrm{N/m^2}$ to fit approximately the diameter function in Fig. 2.8(b), due to the large modulus of elasticity range found in [2, 59, 62], which varies from $E = 2.6 \cdot 10^5\,\mathrm{N/m^2}$ to $1 \cdot 10^6\,\mathrm{N/m^2}$.

Figure 2.9 shows the comparison of the FSI coupled simulation and a rigid wall assumption for the ideal model, which is explained in Fig. 2.6. Figure 2.9(a) shows the pressure distribution p_i along the pipe length z with various inlet pressure boundary conditions $p_i(0)$. There is no visible difference between the rigid and FSI calculation. Figure (b) shows the *Reynolds* number distribution. Due to the rate of flow conservation, the *Reynolds* number increases in the FSI simulation towards the pipe outlet. The rigid model has a constant *Reynolds* number distribution along the pipe length, which is significantly lower on high inlet pressures. A major difference between the two calculations is visible in Fig. (c), showing the solid wall shape, which is a slightly non-linear function in the FSI model and obviously constant with the rigid wall assumption.

As a consequence, the rate of flow increases in the FSI model in comparison with the constant rigid model, in Fig. 2.9(d). As mentioned, this simulation is bounded on laminar *Reynolds* numbers. Hence, the boundary pressure drop is limited. All presented FSI results have non-linear functions, which would be more likely to be seen on higher pressure drop, or with more ductile geometry properties. It could be concluded, that the fluid structure interaction has an increasing influence on the quantitative fluid values with increasing pressure. This influence is assumed to be insignificant in smaller arteries on low *Reynolds* numbers, as discussed in numerous research papers, and summarized in Section 2.2. However, a simulation of blood flow in arteries with rigid walls leads to quantitatively inaccurate fluid values, but still represents the fluid characteristics correct. Therefore, it was decided to neglect fluid structure interaction in this study.

To obtain more realistic results by using the MATLAB program, non-linear elasticity is desirable. Implementing a strain energy function would consider the non-homogeneous stress-strain relationship of arterial tissue, but requires more effort, for instance in computing of *Green-Lagrange* strains, which are dealt with in Section 2.7. The stiffness matrix is not updated during the calculation and this means large deformation is unconsidered. This omission is debatable.

2.4 From Image Data to a Computational Domain

The recent development in high resolution image data techniques enables the gaining of *in-vivo* anatomy information non-invasively. This is a precondition for modelling realistic arterial tubes in a patient specific manner. The geometry has a major influence on haemodynamics. Various geometry creation processes from clinically acquired images are described and compared in [17, pp. 123–175].

Three widely used imaging methods are explained in [8], X-ray computed tomography (CT), magnetic resonance imaging (MRI) and ultrasound imaging (US). During CT-scanning, commonly an iodinated contrast agent is intra-arterial injected, which increases the contrast between blood and surrounding tissue. Because of that, this method shows a superior contrast-to-noise ratio, combined with high temporal and spatial resolution (200–400 µm isotropic). Using high frame rates, complex vessel motion can be recorded. The main disadvantage is the risk associated with catheterization and the risk arising from the radiation dose.

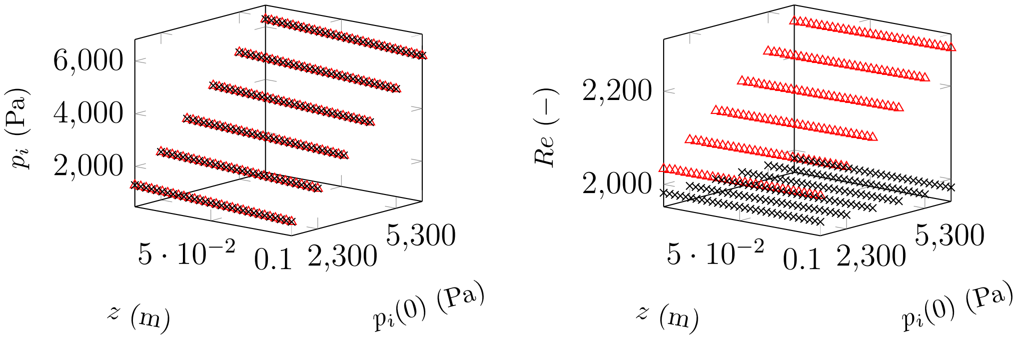

(a) Pressure. (b) *Reynolds* number.

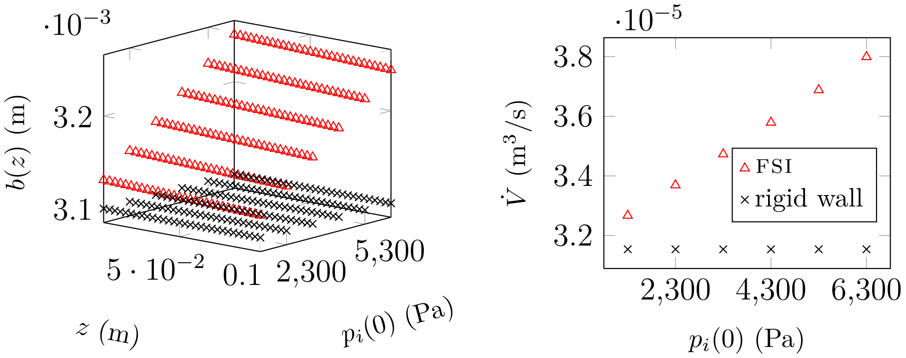

(c) Wall shape. (d) Rate of flow.

Figure 2.9: Comparison between a rigid and a FSI simulation of the CCA using a MATLAB program and ideal geometry. The input parameters were, pipe length $L = 0.1\,\mathrm{m}$, inner radius $b = 0.0031\,\mathrm{m}$, outer radius $a = 0.0036\,\mathrm{m}$, inlet pressure $p_i(0) = 1300, 2300 \ldots 6300\,\mathrm{Pa}$, outlet pressure $p_i(L) = p_i(0) - 300$, viscosity $\mu = 0.00345\,\mathrm{Pa\ s}$, Poisson's ratio $\nu_p = 0.499$ and modulus of elasticity $E = 7.5 \cdot 10^5\,\mathrm{N/m^2}$.

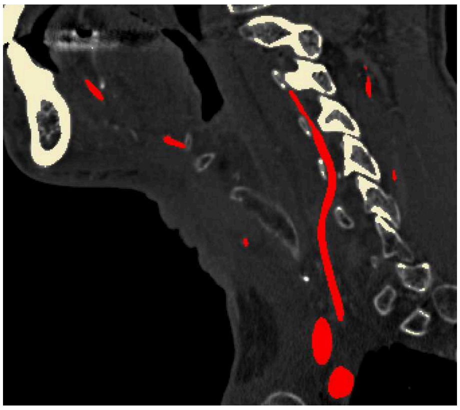

Figure 2.10: Dicom image with red marked artery and white marked bone. On the right side the spine can be seen.

In MRI, the blood itself can be used as contrast agent, which makes this method very attractive. However, to obtain higher signal quality, intra-venous injected contrast agents can be used. This has a negligible risk compared with intra-arterial catheterization. The isotropic spatial resolution is about 600 µm. Furthermore, it is possible to measure accurate spatially resolved time varying flow velocities and flow rate waveforms, assuming a fully developed flow, by using cross sectional integration. The MRI method is excellent in obtaining volunteer data.

In combination with the low costs of ultrasound scanners, US is probably the most widely available method. The image quality depends significantly on the proximity of the transducer. Hence, "[. . .] ultrasound imaging is typically limited to superficial vessels such as the carotid and femoral arteries.", [8]. *Doppler* ultrasound provides real time measured velocities at the centre line of the vessel, assuming a fully developed flow, the mean velocity and flow rate can be calculated. The main disadvantage is the inferior contrast-to-noise ratio in comparison with the previous two methods.

In this project, it was decided to work with real three dimensional geometry. With the software SCANIP [66], head and neck CT-scans of a patient were segmented to generate a volume mesh. It is an image processing software including three dimensional geometry generation and CFD mesh export tools. The image files represent slices across the patient. Using grey scale values, vessels were marked throughout all slices and segmented into a volume. In Fig. 2.10 a dicom image is shown with marked artery and bone. All individual steps from image to mesh are explained in Fig. 2.11. For all following steps it is very important to adjust the lower and upper bound of grey scale histogram carefully at the beginning. A sharp contrast between vessel and surrounding

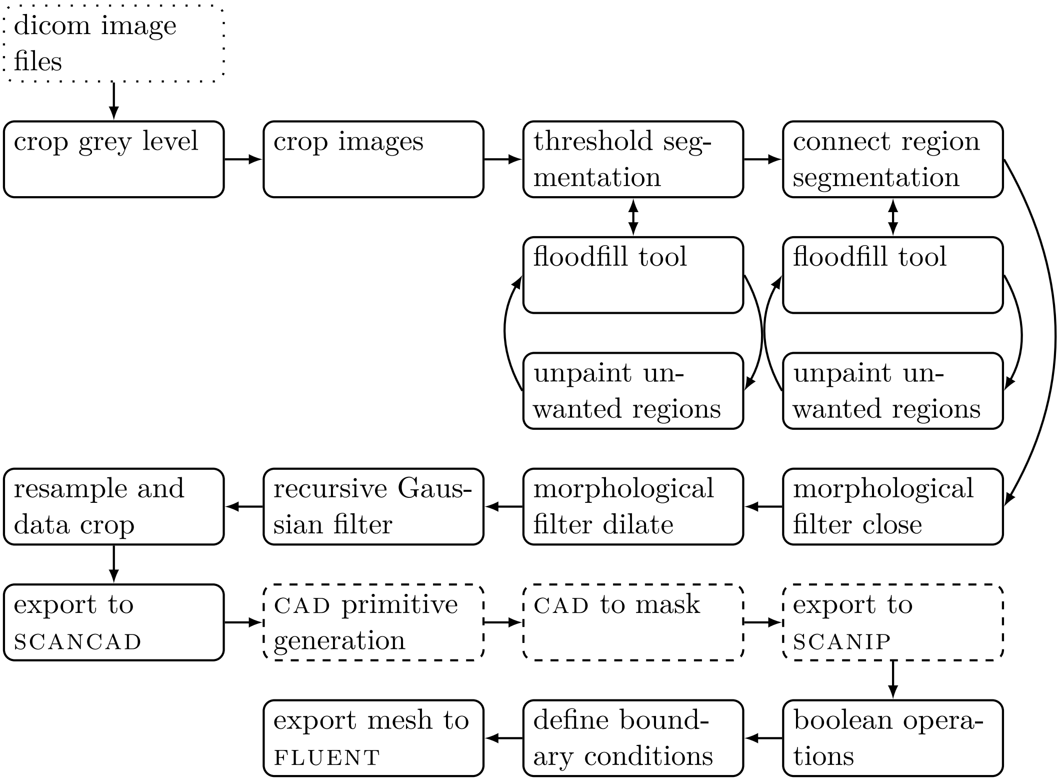

Figure 2.11: Geometry generation with SCANIP (solid box) and SCANCAD (dashed box). In small vessel diameters, the steps in SCANCAD lead to irregular boundary edges. Therefore it is desirable that most vessels terminate at the space limitations. Then the steps in SCANCAD can be omitted.

tissue is desirable. The first segmentation tool is the threshold. Just as with very clear image data, it is possible to obtain the required geometry automatically. It was noticed that arteries and bones have approximately the same grey scale. Because of that, it was necessary to append a process with floodfill and unpaint tools to erase the unwanted regions. The floodfill tool generates one coherent volume and small artefacts are removed. A segmentation tool recommended for small vessels is the connected region growing. By clicking into a centre of an artery this tool combines equal grey scales across some slices. Also here it can appear that unwanted areas are picked-up. Using morphological filters, pixel holes are closed and the size is adapted to the inner diameter of the vessel. Prior to the smoothing process it is useful to enhance the vessel diameter slightly, because the recursive Gaussian filter shrinks the outline. A value of 0.8 mm with linear option is a good compromise between smooth surface and a little outline shrink.

It turned out that the steps in SCANCAD with following boolean operations and smoothing in SCANIP can lead to fuzzy boundary edges. Hence it is better to crop as many as possible of the vessels directly onto the space limitations with the data crop tool.

SCANIP offers export features to various CAD exchange formats, for instance iges or stl files. Such a complex geometry leads to large file sizes. An attempt was made to import a geometry file into the CAD software SWORKS. Two gigabyte memory was insufficient to import the file. With a more powerful workstation, it should be possible to compile the file. Hence it was required to export a FLUENT mesh file. During the export it is possible to set all boundary types and fluid or solid regions. Features like creating a boundary layer or mesh refinement on edges are missing in SCANIP.

2.5 Meshing

Mesh quality and spatial resolution has a considerable influence on CFD simulations. In general there are two ways of meshing; structured and unstructured. A structured mesh contains elements with a high accuracy and offers a short computing time. Depending on the geometry, it is sometimes very difficult or impossible to produce. An unstructured mesh is simpler to generate, needs more computing time and has to be finer for obtaining the same accuracy as the structured mesh. It was decided to combine both advantages and to generate a mixed mesh, shown in Fig. 2.12. The mesh of SCANIP was imported into GAMBIT [67] for remeshing. The software GAMBIT, offers more tools to control the meshing process. It was impossible to convert the geometry in so called real geometry. Then it would be practicable to split the vessel into simpler partial volumes and to generate the very important boundary layer adjacent to the wall in the initial mesh. With such a coarse mesh near the wall, as in Fig. 2.12, the simulation results are not sufficiently accurate.

To enhance the mesh accuracy, the solution-adaptive mesh refinement feature is included in FLUENT. The cell size can be controlled through different values. For example through geometry or numerical solution data. The user sets limits, and cells outside this range are automatically refined or coarsened. First, it makes sense to refine the grid on the wall with the geometry based Boundary tool. Otherwise the following methods will not work well.

An approach for dealing with turbulent flows near walls is the wall y^+ distance (2.32), with the wall shear stress τ_{wall}, the friction velocity u_t and the distance to the nearest wall y_{wall}. This variable describes the non-dimensional distance between the cell centroid and the wall. It is used to describe how fine or coarse the mesh is for particular flow. The ratio between turbulent and laminar

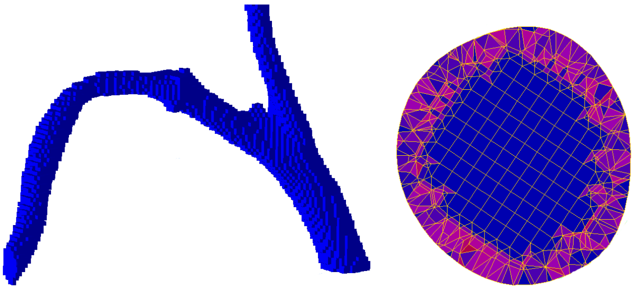

Figure 2.12: The initial mesh consists of hexahedron elements in the core of the vessel, shown separately on the left and tetrahedron elements adjacent to the wall. The element quality extends from high quality with the blue colour to low quality with the red colour. In the cross section, no boundary layer near to the wall is visible. This mesh is insufficient.

influences in a cell, is an additional proper definition.

$$y^+ = \frac{\rho \cdot u_t \cdot y_{wall}}{\mu} \quad \text{with} \quad u_t = \sqrt{\frac{\tau_{wall}}{\rho}} \tag{2.32}$$

Depending on which turbulence model and wall function is used, a lower and upper bound is recommended in [68, ch. 12.11.1]. For the standard and SST k-ω model with enabled transitional flow option, for low or high *Reynolds* numbers, the value of y^+ should be $y^+ = 1$. A higher y^+ is acceptable as long as it is well inside the viscous sublayer $y^+ < 4$–5. Extensive research about using the wall y^+ approach for different turbulence models has been conducted.

> “The different mesh configurations and corresponding wall y^+ have a significant influence on the computed wall friction coefficient [...], but a minimal effect on the mean velocity profile [...]”. [69]

The k-ω model is recommended for near-wall modelling, $y^+ \approx 2.5$ is desirable.

To see the influence of mesh adaption on simulation, it is necessary to iterate with a finer grid further after each convergent computation. During the solution it is useful to monitor surface values, for instance the average velocity on outlets. If these monitors remain unchanged, the grid is fine enough and mesh independence is achieved.

In addition to y^+ adaption it is also useful to refine the grid in areas with a high gradient. The user can choose between many values. For example pressure or velocity. At the start an upper bound of 10 % from current level is recommended. The whole mesh adaption procedure is shown in Fig. 2.13.

Although this process needs at least 3–4 iterations, it is advisable for complex real geometry CFD simulations. The grid is generated out of the flow field and

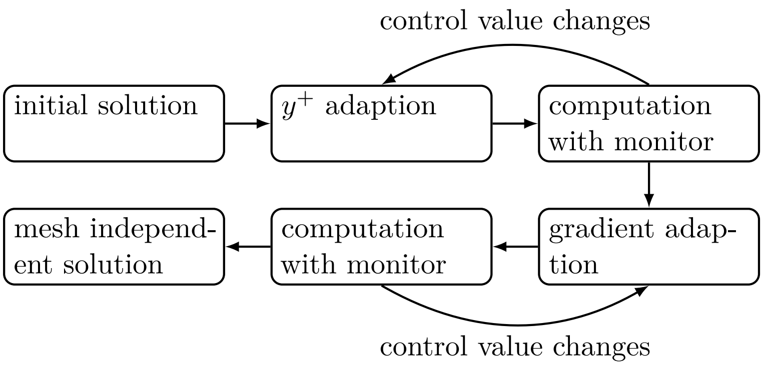

Figure 2.13: Mesh adaption in FLUENT.

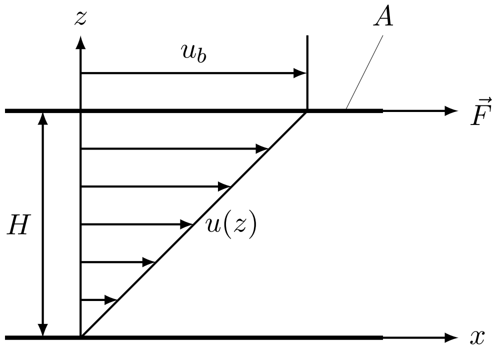

Figure 2.14: Shear flow between parallel plates.

is just as fine as required. In summary, even if the computing time needs one or two days, it is much faster then a manual generated grid including a boundary layer.

2.6 Fluid Model

All fluids have a viscosity or inner friction. It is a resistance to motion which causes shear stress. A common two dimensional model is the *Couette* flow, shown in Fig. 2.14 [14, p. 114]. The gap between two parallel plates, with the distance H, is filled with a fluid. The upper plate moves with the constant velocity u_b while the lower plate remains at rest. Because of the non slip condition on both plate surfaces A, a shear flow is formed. The velocity gradient is also called shear rate (2.33).

$$\dot{\gamma} = \frac{du}{dz} \tag{2.33}$$

For *Newtonian* mediums, the approach (2.34) is valid. The dynamic viscosity μ is a chemical property. Its value is independent of shear rate and is determined by experiments. It is obvious that μ depends on the temperature. Otherwise, the temperature inside the human body is almost constant. In addition to μ the kinematic viscosity ν is also common. Both properties are related through the density $\nu = \mu/\rho$.

$$\tau_{wall} = \mu \frac{du}{dz} = \mu \cdot \dot{\gamma} \quad \text{here is} \quad \tau_{wall} = \tau_{zx} = \tau_{xz} \tag{2.34}$$

In general, for incompressible *Newtonian* fluids, the stress tensor is proportional to the strain rate tensor $\overline{\overline{D}}$ (2.35), also known as rate of deformation tensor, [17, p. 232]. It has only 6 independent components, because of the equal strains $\epsilon_{ij} = \epsilon_{ji}$ in (2.36) with the displacement U.

$$\overline{\overline{\tau}} = 2 \cdot \mu \cdot \overline{\overline{D}} \tag{2.35}$$

$$\overline{\overline{D}} = \begin{pmatrix} \epsilon_{11} & \epsilon_{12} & \epsilon_{13} \\ \epsilon_{21} & \epsilon_{22} & \epsilon_{23} \\ \epsilon_{31} & \epsilon_{32} & \epsilon_{33} \end{pmatrix} \quad \text{with} \quad \epsilon_{ij} = \frac{1}{2}\left(\frac{\partial U_i}{\partial x_j} + \frac{\partial U_j}{\partial x_i}\right) \tag{2.36}$$

Each these terms are written out in (2.37), [70].

$$\overline{\overline{D}} = \begin{pmatrix} \frac{\partial U_1}{\partial x_1} & \frac{1}{2}\left(\frac{\partial U_1}{\partial x_2} + \frac{\partial U_2}{\partial x_1}\right) & \frac{1}{2}\left(\frac{\partial U_1}{\partial x_3} + \frac{\partial U_3}{\partial x_1}\right) \\ \frac{1}{2}\left(\frac{\partial U_2}{\partial x_1} + \frac{\partial U_1}{\partial x_2}\right) & \frac{\partial U_2}{\partial x_2} & \frac{1}{2}\left(\frac{\partial U_2}{\partial x_3} + \frac{\partial U_3}{\partial x_2}\right) \\ \frac{1}{2}\left(\frac{\partial U_3}{\partial x_1} + \frac{\partial U_1}{\partial x_3}\right) & \frac{1}{2}\left(\frac{\partial U_3}{\partial x_2} + \frac{\partial U_2}{\partial x_3}\right) & \frac{\partial U_3}{\partial x_3} \end{pmatrix} \tag{2.37}$$

A very compact equivalent equation with the *Nabla*-operator is $\overline{\overline{D}} = \frac{\nabla\vec{U} + \nabla\vec{U}^T}{2}$.

Non *Newtonian* mediums can be described as a special class of *Reiner-Rivlin* fluids called generalized *Newtonian* fluids. Commonly the viscosity μ is a function of the second and third invariant I_2, I_3 (2.38) [65, pp. 57–58], of the rate of deformation tensor $\overline{\overline{D}}$. However the dependence on the value of I_3 is often considered negligible, [17, p. 232].

$$\begin{aligned} I_1 &= \epsilon_{ii} = \epsilon_{11} + \epsilon_{22} + \epsilon_{33}, \\ I_2 &= \frac{1}{2}(\epsilon_{ij}\epsilon_{ij} - \epsilon_{ii}\epsilon_{jj}) = -(\epsilon_{11}\epsilon_{22} + \epsilon_{22}\epsilon_{33} + \epsilon_{33}\epsilon_{11}), \\ I_3 &= \det(\epsilon_{ij}) = \epsilon_{11}\epsilon_{22}\epsilon_{33}. \end{aligned} \tag{2.38}$$

The equations (2.39) lead to the generalised *Newtonian* model (2.40).

$$\begin{aligned} \overline{\overline{\tau}} &= 2 \cdot \mu(I_2) \cdot \overline{\overline{D}}, \\ \dot{\gamma} &= \sqrt{\frac{1}{2}\overline{\overline{D}} : \overline{\overline{D}}} = \sqrt{-4 \cdot I_2} = \sqrt{4(\epsilon_{11}\epsilon_{22} + \epsilon_{22}\epsilon_{33} + \epsilon_{33}\epsilon_{11})}. \end{aligned} \tag{2.39}$$

$$\overline{\overline{\tau}} = 2 \cdot \mu(\dot{\gamma}) \cdot \overline{\overline{D}}. \tag{2.40}$$

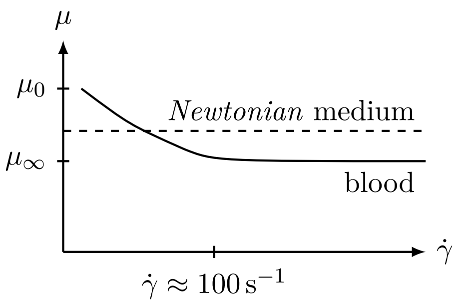

Figure 2.15: Non-*Newtonian* viscosity of blood.

2.6.1 Blood

Blood is a fluid with a non-*Newtonian* viscosity, qualitatively compared with *Newtonian* viscosity in Fig. 2.15, [16, pp. 126–129]. The viscosity is shear rate dependent. The dependence of the blood's shear stress τ on the shear rate $\dot{\gamma}$ can be described to a good approximation with the *Casson* equation, given by (2.41) and dealt with in [14, p. 698].

$$\sqrt{\tau} = K_{cas} \cdot \sqrt{\dot{\gamma}} + \sqrt{C_{cas}} \tag{2.41}$$

A least square fit of measured data yields the relationship (2.42).

$$\sqrt{\frac{\tau}{\mu_p}} = 1.53\sqrt{\dot{\gamma}} + 2 \quad \text{with} \quad \mu_p = 0.0002\,\mathrm{Pa\ s} \tag{2.42}$$

The viscosity of blood is approximately constant when $\dot{\gamma} > 100\,\mathrm{s}^{-1}$, [12, p. 249] and [16, p. 7]. Hence, it is permissible to use a *Newtonian* material model if it is certain that there are no regions with a small shear rate. The flow in veins and small arteries particularly have a very small shear rate. Because of that, non-*Newtonian* models are needed. It is common to use generalized *Newtonian* fluids, which have a shear rate dependent viscosity. A selection is presented in Tab. 2.2. The models *Carreau-Yasuda*, *Simplified Cross* and *Powell-Eyring* should be mentioned additionally. Each model has its advantages and disadvantages, a comparison is studied in [1].

The three non-*Newtonian* viscosity models of Tab. 2.2 are available in FLUENT, [68, ch. 8.4.5]. The *Power-law* model with μ_0 and μ_∞, has an additional temperature term with the reference temperature T_0, which should be set to zero for temperature independent viscosity, given by (2.43).

$$\begin{aligned} &\mu = K \cdot \dot{\gamma}^{(n-1)} \cdot e^{T_0/T}, \\ &\mu_0 < K \cdot \dot{\gamma}^{(n-1)} \cdot e^{T_0/T} < \mu_\infty. \end{aligned} \tag{2.43}$$

Table 2.2: Rheological models for blood, with constant density $\rho = 1056\,\mathrm{kg/m^3}$. Material constants for haematocrit value of $Ht = 45\,\%$ and temparature of $T = 310.15\,\mathrm{K}$, [17, pp. 236–237].

model	$\mu(\dot{\gamma})$	material constants for blood
Newtonian	constant	$\mu = 0.00345\,\mathrm{Pa\ s}$
Power-law	$\mu = K \cdot \dot{\gamma}^{(n-1)}$	$n = 0.775 \quad K = 0.0148\,\mathrm{Pa\ s^n}$
Cross	$\mu = \mu_\infty + \dfrac{\mu_0 - \mu_\infty}{1 + (\lambda_t \dot{\gamma})^m}$	$\mu_0 = 0.056\,\mathrm{Pa\ s} \quad \mu_\infty = 0.00345\,\mathrm{Pa\ s}$ $m = 1.028 \quad \lambda_t = 1.007\,\mathrm{s}$
Carreau	$\mu = \mu_\infty + (\mu_0 - \mu_\infty)[1 + (\lambda_t \dot{\gamma})^2]^{(n-1)/2}$	$\mu_0 = 0.056\,\mathrm{Pa\ s} \quad \mu_\infty = 0.00345\,\mathrm{Pa\ s}$ $n = 0.3568 \quad \lambda_t = 3.313\,\mathrm{s}$ $\mu_0 = 0.056\,\mathrm{Pa\ s} \quad \mu_\infty = 0.00345\,\mathrm{Pa\ s}$

The *Cross* model is determined by (2.44). Unfortunately there is no possibility of adding the zero and infinity viscosity μ_0 and μ_∞ to this model in FLUENT. Hence, the shear rate converged to zero on high shear rates. Therefore, this model implementation is improper for blood flow.

$$\mu = \frac{\mu_0}{1 + (\lambda \dot{\gamma})^{(1-n)}} \tag{2.44}$$

There is also an additional function of temperature $H(T)$ in the *Carreau* model introduced in FLUENT, shown in (2.45). The reference temperature T_α is the temperature where $H(T) = 1$. Hence, if $T = T_\alpha$, $H(T) = 1$ for all values of α and T_0 then this model becomes exactly the same as in Tab. 2.2.

$$\begin{aligned} \mu &= \mu_\infty + (\mu_0 - \mu_\infty)[1 + (H(T) \cdot \lambda_t \dot{\gamma})^2]^{(n-1)/2}, \\ H(T) &= \exp\left[\alpha\left(\frac{1}{T - T_0} - \frac{1}{T_\alpha - T_0}\right)\right]. \end{aligned} \tag{2.45}$$

A comparison between the *Power-law* and *Carreau* model is shown in Fig. 2.16. The Carreau model is more realistic in low shear rates than the *Power-law* model. Therefore the Carreau model seems to be superior for the use in FLUENT. In [1] and [64, pp. 89–96] more non-*Newtonian* models are compared.

2.6.2 Chemical Agent

Cisplatin (cis-diamminedichloroplatinum) is a widely used platinum-based anti cancer drug for treating various types of cancers. It is a heavy metal complex containing a central atom of platinum surrounded by two chloride atoms and two ammonia molecules, shown in Fig. 2.17. It is a yellow non odorous powder with the molecular formula $\mathrm{Cl_2H_6N_2Pt^{+2}}$, and a molecular weight of $300.05\,\mathrm{g/mol}$. It is soluble in water or saline up to $2530\,\mathrm{mg/l}$. It has a melting point of

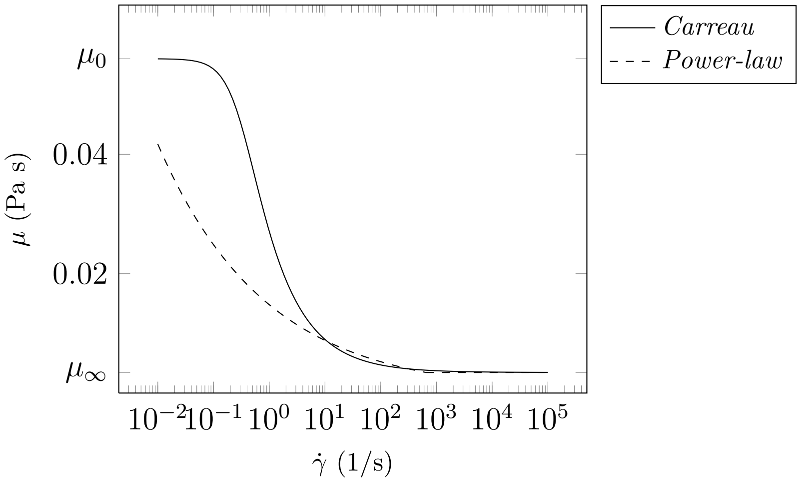

Figure 2.16: Non-*Newtonian* blood viscosity models available in FLUENT. The *Power-law* model in FLUENT is limited between μ_0 and μ_∞, to prevent that the model closes asymptotically to zero on high shear rates and to ∞ on $\lim_{\dot{\gamma}\to 0}$.

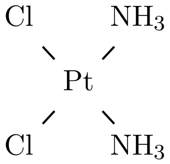

Figure 2.17: Cisplatin.

207 °C, [71]. Usually it is administered intravenously as a short-term infusion in physiological saline for the treatment of solid malignant tumours. In this study, it was decided to assume material properties of water, which means *Newtonian* behaviour, a constant density of $\rho = 998.2\,\mathrm{kg/m^3}$ and a constant viscosity of $\mu = 0.001003\,\mathrm{Pa\ s}$.

2.7 Solid Model

Soft tissue, for instance skin or arterial walls, shows viscoelastic and anisotropic properties, because of the distribution of stiff collagen fibres, [21, p. 180]. Figure 2.18(a) shows a typical stress-strain response of soft tissue. Non-linear elasticity and hysteresis is visible. Furthermore, viscoelasticity is characterized through relaxation Fig. 2.18(b) and conditioning Fig. 2.18(c). Relaxation is a time dependent decreasing stress response to a constant stress load. Conditioning

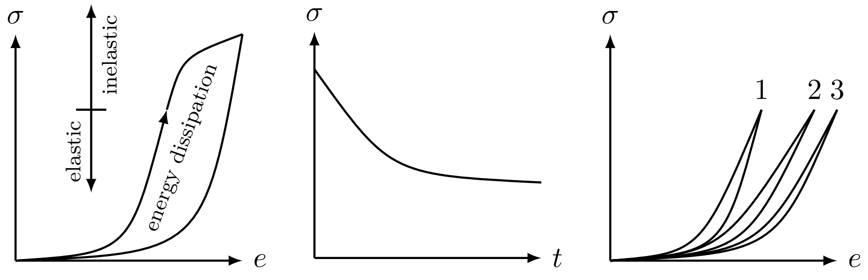

(a) Hysteresis. (b) Relaxation. (c) Conditioning.

Figure 2.18: Viscoelasticity of soft tissue.

is a cyclic adjustment of mechanical material properties to a specified load, causing a finite increasing strain response.

The first mechanical model for soft tissues introduced by Fung, neglects anisotropy and was an uniaxial exponential stress-stretch relation on the basis of experimental results from mensentary tissue. The formula is given by (2.46), with the material constants C_1 and C_2, dealt with in [21, p. 212].

$$\sigma = \frac{C_1}{C_2}(\exp[C_2(\epsilon - 1)] - 1) \tag{2.46}$$

Nowadays, mechanical models for soft tissue are determined with strain-energy functions Ψ, based on the *Green-Lagrange* strain tensor $\overline{\overline{e}}$, [18, 22, 23]. In general, strain-energy functions are only valid for hyper-elastic materials without energy dissipation, which means without hysteresis. However, using two separate strain-energy functions for applied load and release, allows the description of hypo-elastic materials with hysteresis. This procedure is known as the concept of pseudo-elasticity.

Green-Lagrange strains are non-linear and in *Cartesian* tensor notation defined by (2.47), [72].

$$\begin{aligned} e_{ij} &= \frac{1}{2}(U_{i,j} + U_{j,i} + U_{k,i}U_{k,j}), \\ &= \epsilon_{ij} + \frac{1}{2}(U_{1,i}U_{1,j} + U_{2,i}U_{2,j} + U_{3,i}U_{3,j}). \end{aligned} \tag{2.47}$$

The extensive definition of $\overline{\overline{e}}$ is given by (2.48) [12, p. 52] and shows the non-linear properties in contrast to *Cauchy*-strains (2.36).

$$\begin{aligned}
e_{11} &= \frac{\partial U_1}{\partial x_1} + \frac{1}{2} \cdot \sum_{i=1}^{3} \left(\frac{\partial U_i}{\partial x_1} \right)^2, \\
e_{22} &= \frac{\partial U_2}{\partial x_2} + \frac{1}{2} \cdot \sum_{i=1}^{3} \left(\frac{\partial U_i}{\partial x_2} \right)^2, \\
e_{22} &= \frac{\partial U_3}{\partial x_3} + \frac{1}{2} \cdot \sum_{i=1}^{3} \left(\frac{\partial U_i}{\partial x_3} \right)^2, \\
e_{12} &= \frac{1}{2} \left(\frac{\partial U_1}{\partial x_2} + \frac{\partial U_2}{\partial x_1} + \frac{\partial U_1}{\partial x_1}\frac{\partial U_1}{\partial x_2} + \frac{\partial U_2}{\partial x_1}\frac{\partial U_2}{\partial x_2} + \frac{\partial U_3}{\partial x_1}\frac{\partial U_3}{\partial x_2} \right) = e_{21}, \\
e_{23} &= \frac{1}{2} \left(\frac{\partial U_2}{\partial x_3} + \frac{\partial U_3}{\partial x_2} + \frac{\partial U_1}{\partial x_2}\frac{\partial U_1}{\partial x_3} + \frac{\partial U_2}{\partial x_2}\frac{\partial U_2}{\partial x_3} + \frac{\partial U_3}{\partial x_2}\frac{\partial U_3}{\partial x_3} \right) = e_{32}, \\
e_{31} &= \frac{1}{2} \left(\frac{\partial U_3}{\partial x_1} + \frac{\partial U_1}{\partial x_3} + \frac{\partial U_1}{\partial x_3}\frac{\partial U_1}{\partial x_1} + \frac{\partial U_2}{\partial x_3}\frac{\partial U_2}{\partial x_1} + \frac{\partial U_3}{\partial x_3}\frac{\partial U_3}{\partial x_1} \right) = e_{13}.
\end{aligned} \tag{2.48}$$

One example of a strain-energy function for arterial walls in cylindrical coordinates introduced by Fung is presented in (2.49), with material constants C_0 and $b_1 \dots b_9$, [23].

$$\begin{aligned}
\Psi &= \frac{1}{2} C_0 [\exp(Q) - 1], \\
Q &= b_1 e_{\phi\phi}^2 + b_2 e_{zz}^2 + b_3 e_{rr}^2 + 2b_4 e_{\phi\phi} e_{zz} + 2b_5 e_{zz} e_{rr} + 2b_6 e_{rr} e_{\phi\phi}, \\
&\quad + b_7 e_{\phi z}^2 + b_8 e_{rz}^2 + b_9 e_{r\phi}^2.
\end{aligned} \tag{2.49}$$

2.8 Turbulence

Turbulence is a flow state characterized by apparently random vorticity. Often it is measured through transient velocity fluctuations. The famous *Reynolds*-experiment from 1883 is one way to make turbulence visible. If turbulence is present the whole flow field changes its behaviour. The velocity profile changes from parabolic to logarithmic (Fig. 2.2) near walls in pipe flows. Energy exchange between molecules, heat exchange, drag and mixing is increased in comparison to laminar flows. A detailed description of turbulent effects can be found in [73].

With the *Navier-Stokes* equations it is possible to solve turbulent flows directly. However for direct numerical simulation (DNS) an excessive fine mesh and computer power is also compulsory to solve the smallest eddy motions.

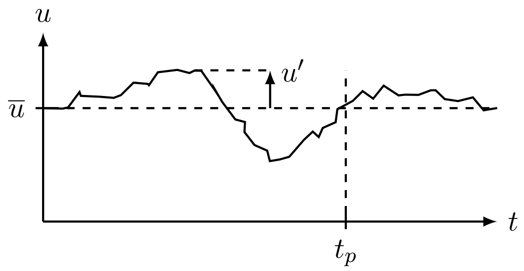

Figure 2.19: Mean velocity component $\overline{u}$ at a point $(x_{1,2,3})$.

Therefore today it is only possible to compute simple flows on rather small *Reynolds* numbers. The DNS is a tool for turbulence research and is an addition to turbulence measurements.

Because of that, assumptions are required to overcome the need to calculate the small eddy motions. The eddy size extends over a large quantity, defined by the *Kolmogorov* scale of turbulence. The small eddies have a damping effect on the turbulent fluctuations. Turbulent kinetic energy dissipates into heat. This effect is determined by the eddy viscosity μ_T, which is a property of the flow field not of the fluid.

In 1895 O. Reynolds introduced a view about turbulence which simplifies the solution for turbulent flows. With the *Reynolds* averaged assumption (2.50), the velocity $\vec{u}$ is an addition of a time independent mean velocity $\vec{\overline{u}}$ and time dependent turbulent fluctuations $\vec{u'}$, [74, p. 524]. The mean velocity components are integral values per period of time t_p, defined in (2.51) and shown in Fig. 2.19.

$$\vec{u} = \vec{\overline{u}} + \vec{u'} \tag{2.50}$$

$$\vec{\overline{u}}(\vec{x}) = \lim_{t_p \to \infty} \frac{1}{t_p} \int_{t=0}^{t_p} \vec{u'}(\vec{x}, t)\ \mathrm{d}t \tag{2.51}$$

It is an area averaged method. The integral of the turbulent fluctuations over time is zero and the integral of the velocity is the mean velocity (2.52). This approach is valid not only for velocity but also for the pressure, temperature and density.

$$\int_{t=0}^{\infty} \vec{u'}(\vec{x}, t)\ \mathrm{d}t = 0 \quad \text{and} \quad \int_{t=0}^{\infty} \vec{u}(\vec{x}, t) = \vec{\overline{u}}(\vec{x}) \tag{2.52}$$

The *Navier-Stokes* equations are changing in the *Reynolds* equations or also called *Reynolds*-averaged *Navier-Stokes* (RANS) equations. In (2.53) the RANS equations are given for *Newtonian* fluids with constant density, [46, p. 168]. After time averaging, the continuity equation is the only one which remains unchanged in comparison to laminar flow. New turbulent momentum transport terms are introduced in the impulse equation and energy equation. These terms are condensed in the *Reynolds* stress tensor $\overline{\overline{\tau_{Re}}}$ (2.54). The fluctuating stresses in $\overline{\overline{\tau_{Re}}}$ are undetermined, the RANS equations are not solvable without turbulence models. These models are required to calculate the turbulent fluctuations out from the mean values.

$$\begin{aligned}
\frac{\partial \overline{u}}{\partial x}+\frac{\partial \overline{v}}{\partial y}+\frac{\partial \overline{w}}{\partial z} =&0,\\
\rho\left(\overline{u}\frac{\partial \overline{u}}{\partial x}+\overline{v}\frac{\partial \overline{u}}{\partial y}+\overline{w}\frac{\partial \overline{u}}{\partial z}\right) =&-\frac{\partial \overline{p}}{\partial x}+\mu\left(\frac{\partial^2 \overline{u}}{\partial x^2}+\frac{\partial^2 \overline{u}}{\partial y^2}+\frac{\partial^2 \overline{u}}{\partial z^2}\right)\\
&-\left(\frac{\partial}{\partial x}\rho\overline{u^2}+\frac{\partial}{\partial y}\rho\overline{uv'}+\frac{\partial}{\partial z}\rho\overline{u'w'}\right),\\
\rho\left(\overline{u}\frac{\partial \overline{v}}{\partial x}+\overline{v}\frac{\partial \overline{v}}{\partial y}+\overline{w}\frac{\partial \overline{v}}{\partial z}\right) =&-\frac{\partial \overline{p}}{\partial y}+\mu\left(\frac{\partial^2 \overline{v}}{\partial x^2}+\frac{\partial^2 \overline{v}}{\partial y^2}+\frac{\partial^2 \overline{v}}{\partial z^2}\right)\\
&-\left(\frac{\partial}{\partial x}\rho\overline{v'u'}+\frac{\partial}{\partial y}\rho\overline{v'^2}+\frac{\partial}{\partial z}\rho\overline{v'w'}\right), \qquad (2.53)\\
\rho\left(\overline{u}\frac{\partial \overline{w}}{\partial x}+\overline{v}\frac{\partial \overline{w}}{\partial y}+\overline{w}\frac{\partial \overline{w}}{\partial z}\right) =&-\frac{\partial \overline{p}}{\partial z}+\mu\left(\frac{\partial^2 \overline{w}}{\partial x^2}+\frac{\partial^2 \overline{w}}{\partial y^2}+\frac{\partial^2 \overline{w}}{\partial z^2}\right)\\
&-\left(\frac{\partial}{\partial x}\rho\overline{w'u'}+\frac{\partial}{\partial y}\rho\overline{w'v'}+\frac{\partial}{\partial z}\rho\overline{w'^2}\right),\\
\rho c_p\left(\overline{u}\frac{\partial \overline{T}}{\partial x}+\overline{v}\frac{\partial \overline{T}}{\partial y}+\overline{w}\frac{\partial \overline{T}}{\partial z}\right) =&\lambda\left(\frac{\partial^2 \overline{T}}{\partial x^2}+\frac{\partial^2 \overline{T}}{\partial y^2}+\frac{\partial^2 \overline{T}}{\partial z^2}\right)\\
&-\left(\frac{\partial}{\partial x}\rho c_p\overline{T'u'}+\frac{\partial}{\partial y}\rho c_p\overline{T'v'}+\frac{\partial}{\partial z}\rho c_p\overline{T'w'}\right).
\end{aligned}$$

$$\overline{\overline{\tau_{Re}}} = -\rho\overline{u'_i u'_j} = -\rho\begin{pmatrix}\overline{u'u'} & \overline{u'v'} & \overline{u'w'}\\ \overline{v'u'} & \overline{v'v'} & \overline{v'w'}\\ \overline{w'u'} & \overline{w'v'} & \overline{w'w'}\end{pmatrix} \qquad (2.54)$$

A value to describe turbulence is the turbulence intensity I (2.55). It is the ratio between root mean square of the turbulent velocity fluctuations $\vec{u'}$ and the magnitude of the mean velocity u_{mag}.

$$\begin{aligned}
I =& \frac{u'_{rms}}{u_{mag}},\\
u'_{rms} =& \sqrt{\frac{1}{3}\left(u'^2+v'^2+w'^2\right)} \quad \text{and} \quad u_{mag}=\sqrt{\overline{u}^2+\overline{v}^2+\overline{w}^2}. \qquad (2.55)
\end{aligned}$$

The turbulence intensity can be divided into three thresholds:

- “High-turbulence case: High speed flow inside complex geometries like heat exchangers and flow inside rotating machinery (turbines and compressors). Typically the turbulence intensity is between 5 % and 20 %.
- Medium-turbulence case: Flow in not so complex devices like large pipes, ventilation flows etc. or low speed flows (low *Reynolds* number). Typically the turbulence intensity is between 1 % and 5 %.
- Low-turbulence case: Flow originating from a fluid that stands still, like external flow across cars, submarines and aircrafts. Very high-quality wind tunnels can also reach really low turbulence levels. Typically the turbulence intensity is very low, well below 1 %” [75].

Another value to describe the strength of turbulent eddies is the turbulent kinetic energy k, shown by (2.56). It is the mean kinetic energy per unit mass associated with large eddies in turbulent flow.

$$k = \frac{1}{2}\left(\overline{u'^2} + \overline{v'^2} + \overline{w'^2}\right) \tag{2.56}$$

2.8.1 Choosing a Turbulence Model

There is no single turbulence model which is universally superior for all classes of fluid flow. A guideline for choosing an appropriate turbulence model is presented in [68, ch. 12.2]. Apart from the direct numerical simulation, which solves the *Navier-Stokes* equations directly without any simplifications, most turbulence models are created by empirical correlations obtained from experiments.

There is a general relationship between computational effort and accuracy. The so called two equation models k-ϵ and k-ω are widely accepted in combination with the RANS equations, shown in (2.53). Both models are rather engineering-approximations than scientific laws, based on eddy viscosity. These two models compute turbulent flows with an adequate accuracy and require few computational resources. A limitation in both models is the isotropic turbulence approach, which means that turbulence is reduced to a scalar field.

The next level of accuracy is the large eddy simulation (LES), which solves explicitly the *Navier-Stokes* equations for large scales of motion and uses models and assumptions just for small eddies. This is just a very small selection of present turbulence models. Turbulence is an ongoing research field and new models are introduced every year.

The method with superior accuracy, but also with extensively resource consumption, is the already mentioned DNS. In contrast to all other models, there is no time averaged approach or turbulence model present, which means, that turbulence here is space and time dependent. As mentioned, today this method is just usable for low *Reynolds* number flows with simple geometry and requires high performance computer clusters. It is used in turbulence research, combustion, convective heat transfer and aerodynamic noise simulation, [44, pp. 319–320]. It is questionable if it is required to solve turbulence exhaustive in every case.

> “The solution would result in such a large amount of information that it could not be possible to process them further, or to exploit them, in order to gain new insights into fluid mechanical processes.” [74, p. 527]

The boundary layer represents a big share in arterial network, especially in small vessels. The core zone is small, for instance in comparison with aerodynamic flows. The k-ω turbulence model proposed by Wilcox [76] is designed for near wall modelling on low *Reynolds* number flows. The k-ϵ model has advantages in turbulent core flows, but is not valid throughout the boundary layer. Hence, wall functions are used. The Shear-Stress transport (SST) k-ω model introduced by Menter [77] blends the k-ϵ model in the core region and k-ω model in the near wall region. A comparative study of different turbulence models with experiments in near wall treatment is presented by [69]. It can be seen, that the k-ω model shows a high correlation with experimental data, if the mesh has a high resolution in the viscous sublayer region. It was decided to use the k-ω turbulence model in this project. A comparison with the SST k-ω model seems to be useful.

2.8.2 The k-ω Turbulence Model

A brief description of the k-ω model, used in FLUENT, is found in [68, ch. 12.5.1]. The *Reynolds* stresses are computed with the *Boussinesq* expression, shown in (2.57). It is an empirical model based on model transport equations for turbulent kinetic energy k and the specific dissipation rate ω, shown by (2.58). The model has been modified over the years and hence, production terms have been added in contrast to the initial equation proposed by Wilcox [76].

$$\overline{\overline{\tau_{Re}}} = -\rho\overline{u'_i u'_j} = \mu_T\left(\frac{\partial\overline{u}_i}{\partial x_j}+\frac{\partial\overline{u}_j}{\partial x_i}\right)-\frac{2}{3}\left(\rho k+\mu_T\frac{\partial\overline{u}_k}{\partial x_k}\right)\delta_{ij} \tag{2.57}$$

$$\frac{\partial}{\partial t}(\rho k) + \frac{\partial}{\partial x_i}(\rho k \overline{u}_i) = \frac{\partial}{\partial x_j}\left(\Gamma_k \frac{\partial k}{\partial x_j}\right) + G_k - Y_k + S_k,$$
$$\frac{\partial}{\partial t}(\rho \omega) + \frac{\partial}{\partial x_i}(\rho \omega \overline{u}_i) = \frac{\partial}{\partial x_j}\left(\Gamma_\omega \frac{\partial \omega}{\partial x_j}\right) + G_\omega - Y_\omega + S_\omega. \tag{2.58}$$

G_k and G_ω represent the generation of turbulent kinetic energy and specific dissipation rate due to mean velocity gradients. Γ_k and Γ_ω are effective diffusivity terms and Y_k, Y_ω are dissipation of k and ω due to turbulence. S_k and S_ω are user-defined source terms. The effective diffusivities are shown in (2.59), where σ_k and σ_ω are the turbulent *Prandtl* numbers for k and ω.

$$\Gamma_k = \mu + \frac{\mu_T}{\sigma_k},$$
$$\Gamma_\omega = \mu + \frac{\mu_T}{\sigma_\omega}. \tag{2.59}$$

The turbulent viscosity is computed by (2.60).

$$\mu_T = \alpha^* \frac{\rho \cdot k}{\omega} \tag{2.60}$$

The coefficient α^* damps the turbulent viscosity causing a low *Reynolds* number correction (2.61), with $Re_t = (\rho \cdot k)/(\mu \cdot \omega)$, $R_k = 6$, $\alpha_0^* = \beta_i/3$ and $\beta_i = 0.072$.

$$\alpha^* = \alpha_\infty^* \left(\frac{\alpha_0^* + Re_t/R_k}{1 + Re_t/R_k}\right) \tag{2.61}$$

In high *Reynolds* number k-ω model is $\alpha^* = \alpha_\infty^* = 1$. The production of k and ω is given by (2.62), with $R_\omega = 2.95$ and $\alpha_0 = 1/9$.

$$G_k = -\rho \overline{u_i' u_j'} \frac{\partial u_j}{\partial x_i},$$
$$G_\omega = \alpha^\star \frac{\omega}{k} G_k, \tag{2.62}$$
$$\alpha^\star = \frac{\alpha_\infty}{\alpha^*}\left(\frac{\alpha_0 + Re_t/R_\omega}{1 + Re_t/R_\omega}\right).$$

Also here is $\alpha^\star = \alpha_\infty = 1$ in the high *Reynolds* number form of the k-ω model. The author avoids indicating the long dissipation of k and ω equations, they are to be found in [68, ch. 12.5.1]. The model constants are shown in (2.63).

$$\alpha_\infty^* = 1, \quad \alpha_\infty = 0.52, \quad \sigma_k = \sigma_\omega = 2.0 \tag{2.63}$$

2.8.3 Determining Turbulence Parameters

In the standard and SST k-ω model are two parameters to be set for every inlet and outlet. The turbulent kinetic energy k and the specific dissipation rate ω. In the best case it is possible to determine these parameters from measured data. In [68, ch. 7.2.2] is a best practice described for an approximately setup for k (2.64) and ω (2.65). The turbulence intensity I (2.66) can be estimated from an empirical correlation for pipe flows with fully developed turbulent flow. The *Reynolds* number is given by (2.67). As discussed in Section 2.1.3, fully developed turbulent flow is not present in arteries, hence this approach leads to large values of turbulence.

$$k = \frac{3}{2}(u_{mag} \cdot I)^2 \tag{2.64}$$

$$\omega = \frac{k^{1/2}}{C_\mu^{1/4} \cdot l_T} \quad \text{with} \quad C_\mu = 0.09 \quad \text{and} \quad l_T = 0.07 \cdot d_h \tag{2.65}$$

$$I = 0.16 \cdot Re^{-\frac{1}{8}} \tag{2.66}$$

$$Re = \frac{u_{mag} \cdot d_h \cdot \rho}{\mu} \tag{2.67}$$

To determine the hydraulic diameter d_h (2.68) it is necessary to know the circumference C and area A of the vessel cross section. In FLUENT it is simple to measure the area. A proper way to specify C is to create an iso-surface onto the cross section with a velocity value of zero. Because of the non-slip condition a spline is produced which is connected to the wall. Using a xy-plot with the option curve-length as position, the circumference C is computed. However, FLUENT cannot plot a value along an endless iso-surface, like a circle. Hence, if the cross section wall is very smooth, FLUENT is unable in determining a start and end point. In this case it is valid to approximate d_h out of the area (2.69).

$$d_h = 4 \cdot A/C \tag{2.68}$$

$$d_h = 2\sqrt{\frac{A}{\pi}} \tag{2.69}$$

2.9 Multiphase Models

In cancer treatment using chemotherapy, the flow contains two liquids; blood and cisplatin. It is assumed that a miscible flow occurs, by reason that blood, as well as the cisplatin dilution are water based. Both substances are of the same phase. Hence, their mixture is a one-phase flow, containing two components.

There are several multiphase models available. To characterize multiphase flow, or in this case multicomponent flow, the dimensionless *Stokes* number is of great significance, given by (2.70). It is a ratio between the particle relaxation time and the characteristic time scale of the flow. Index c means continuous component (blood) and index d disperse component (cisplatin). If $St \ll 1$, particles will closely follow the flow field. If $St \gg 1$, particles will move independently of the flow field.

$$St = \frac{\tau_d}{\tau_c} \tag{2.70}$$

In determining the *Stokes* number, it is often assumed that the dispersed component or phase comprises of spheric bubbles. Then, the particle relaxation time τ_d can be written as (2.71) with the bubble diameter d_d. The characteristic time scale τ_c of the flow is the ratio between characteristic length, here the hydraulic diameter and the velocity scale, given by (2.72), dealt with in [46, p. 194].

$$\tau_d = \frac{\rho_d \cdot {d_d}^2}{18\mu_c} \tag{2.71}$$

$$\tau_c = \frac{d_h}{u_{mag}} \tag{2.72}$$

Commonly two different approaches are used to describe multiphase models mathematically. Modelling discrete phases by using the *Euler-Lagrange* approach is not adequate, due to a fundamental assumption that the dispersed second phase occupies a low volume fraction (< 10–12 %), which is not known previously, [68, ch. 22.1.2].

The second category is comprised of models using the *Euler-Euler* approach. FLUENT treats different phases as penetrating continua and a concept of phasic volume fraction is used, which means the volume fraction is mapped as continuous functions in time and space and their sum is equal to one. In FLUENT, there are three multiphase models available. The volume of fluid method (VOF) can solve two or more immiscible fluids and is commonly used in the modelling of large bubbles or open channels for tracking the liquid-gas interface. Hence, this method can be excluded.

The mixture model is designed for particle-laden flows and bubble flows on $St \ll 1$ and is a simplified multiphase model, which means it solves for the mixture the momentum equation and prescribes relative velocities to describe the dispersed phases.

> “The mixture model is a simplified multiphase model that can be used to model multiphase flows where the phases move at different

> velocities, but assume local equilibrium over short spatial length scales. The coupling between the phases should be strong. [. . .] In addition, the mixture model can be used to calculate non-*Newtonian* viscosity." [68, ch. 23.4.1]

The most complex of all multiphase models is the *Eulerian* model, because it solves a set of i momentum and continuity equations for each phase. It is the most accurate model and valid for all *Stokes* numbers, but it also requires the most computational effort and user inputs.

In this study, it is to be expected that blood and cisplatin are moving in similar directions with different velocities. The coupling between these components is assumed to be strong. Hence, the mixture model seems to be the most appropriate. The model equations are to be found in [68, ch. 23.4.2].

2.10 Measured Data

Blood flow measurement can be distinguished by direct or indirect methods and by invasive or non invasive techniques. In CFD blood flow simulation, blood pressure and velocity in terms of rate of flow are of major interest as boundary condition. As blood circulation is pulsatile, that is a particular type of unsteady flow, time dependent functions are required. Therefore, the familiar pressure cuff method at the upper arm's brachial artery, using a pneumatic cuff and a stethoscope for the detection of *Korotkoff* sound, is insufficient.

One time dependent and direct blood pressure measurement method is to insert a catheter in the arterial network. Apart from the risk by catheterization, this procedure also influences the local haemodynamics by the present sensor. Invasive methods are commonly unsuitable for routine examination and research with volunteers.

In [16, pp. 344–390], an extensive description is given for several time dependent and non invasive techniques, such as ultrasound and laser *Doppler* velocimetry or MRI velocity mapping. Figure 2.20 refers to several research papers, which deal with non invasive *in-vivo* measurement of blood pressure or rate of flow in the common carotid artery, the internal carotid artery and external carotid artery.

Magnetic resonance and ultrasound imaging provide geometric data, such as wall thickness and vessel diameter, as well as blood velocities. In [25], ultrasound *Doppler* velocimetry is used for creating an archetypal blood flow waveform in the common carotid artery of 6 female and 11 male healthy volunteers in the 24–34 age group, shown in Fig. 2.20(a). The heart cycle time was $t_p = 0.917\,\mathrm{s}$ and the CCA mean diameter 6.3 mm.

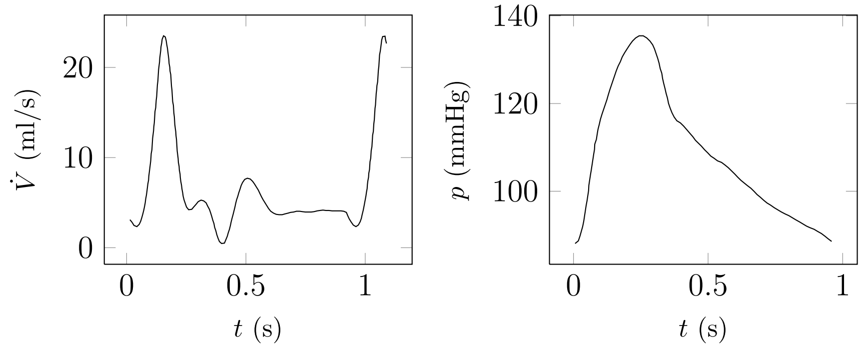

(a) Rate of flow CCA [25].

(b) Pressure CCA [26].

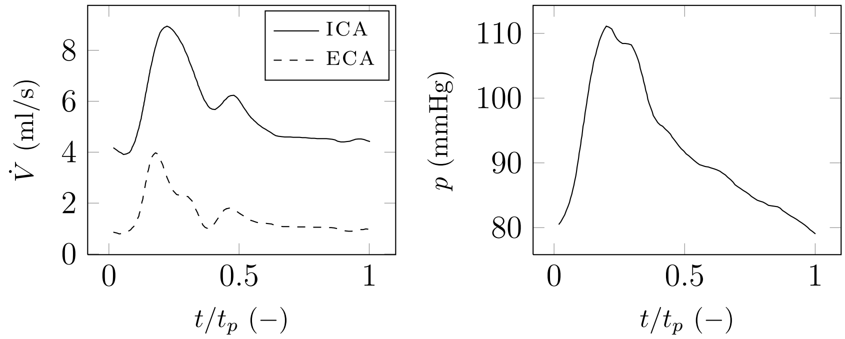

(c) Rate of flow ICA and ECA [59].

(d) Pressure CCA [59].

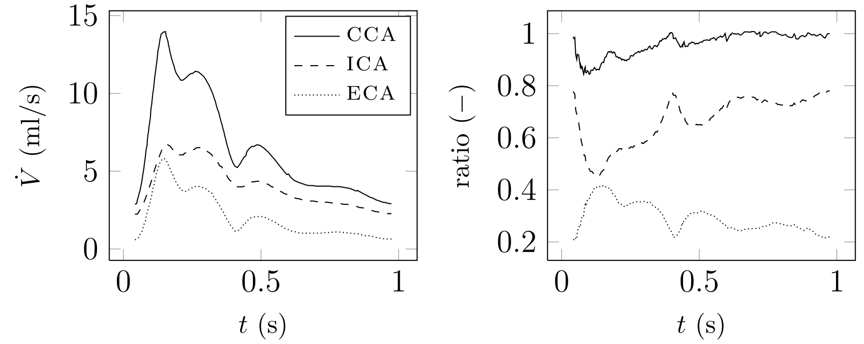

(e) Rate of flow CCA, ICA and ECA [78].

(f) Rate of flow ratios [78], solid (ICA +ECA)/CCA, dashed ICA/CCA, dotted ECA/CCA.

Figure 2.20: Measured data of CCA, ICA and ECA.

Table 2.3: Measurements of the cycle averaged CCA rate of flow division in ml/min and the relative outflow/inflow mass loss.

reference	$\dot{V}$ ICA	$\dot{V}$ ECA	$\dot{V}$ CCA	$\dot{m}$ loss
[78]	245	125	389	4.9 %
[82]	248	95	370	7.0 %
[83]	255	95	376	6.9 %

Image based velocity measurement techniques commonly use an assumption of uniform flow. Because of this, high accuracy is only achievable in relatively straight vessels, [8]. A high temporal and, if using MRI, spatial resolution are required to maintain time dependent velocity functions.

Using a calibrated pressure vessel distension function, blood pressure can be measured indirectly out of the time dependent vessel diameter in a non invasive way, and this is shown for the common carotid artery in [26, 79, 80]. Figure 2.20(b) shows a pressure waveform for the CCA, which is statistically assessed in 2026 subjects and already presented in Section 2.3 Fig. 2.8.

Time dependent rate of flow and pressure data, using for a common carotid artery bifurcation CFD model as boundary conditions, is presented in Fig. 2.20(c) and (d), [59]. This data is obtained of one healthy male volunteer, by using *Doppler* ultrasound and applanation tonometry and was simultaneously recorded. The flow split ratio ICA/ECA is about 75/25. A similar study, using MRI velocity measurements, is found in [81].

The simultaneous measured rate of flow in CCA, ECA, ICA, shown in Fig. 2.20(e), is obtained from 94 older adults (age 68 ± 8 years). The CCA flow function is distinguished from younger volunteers, compared with Fig. (a). The calculated flow division into the ICA and ECA is presented in (f). The flow distribution is time dependent and there is a peak mass loss of about 10 % during early systole. The cycle averaged outflow/inflow deficit in [78] is explained with:

> ”[. . .] we suggest that at least some of this flow deficit may be attributed to the superior thyroid or other small branch arteries that arise off the ECA, and sometimes the CCA, near the bifurcation.“

Table 2.3 compares the time averaged flow division and mass loss of further studies. According to this measured data, the STA flow proportion is assumed with max. 20 % of the ECA flow in a CFD study, dealt with in [84].

3 STEADY SIMULATION

The simulation of blood flow in head and neck vessels with patient specific geometry was started with a model of the right head and neck arterial network, shown in Fig. 3.2. In general, a transient CFD simulation demands a large computation time and requires extensive memory and disk capacity in comparison with a steady simulation. A cause and effect study is compulsory to set up a realistic transient simulation with appropriate parameters. Therefore, it is good to begin with a steady simulation to study the effects of various meshes, *Reynolds* numbers, turbulence models and material models. In order to simplify the simulation, fluid structure interaction was not considered, hence rigid walls were set up for this model. First order discretization was used. The geometry was created as described in Section 2.4.

3.1 Mesh

The mesh consists of hexahedron elements in the artery core and tetrahedron elements for the vessel wall. Due to this separation, the core elements have a perfect quality, the skewness being close to zero. The focus was on the tetrahedron elements next to the wall. To resolve the boundary layer, it is required to create a fine mesh next to the wall. The mesh refinement and independence test was done by wall y^+ adaption and pressure gradient adaption in FLUENT.

In the most critical case with the maximum *Reynolds* number, a value of $y^+ = 5.9$ was achieved, which is slightly above the recommendation of $y^+ < 5$, found in [68, ch. 12.11.1]. In [69], the desirable value of wall y^+ for the k-ω model is 2.5. The final mesh comprises 1286416 elements and 517304 nodes. The impact on the simulation results, during the mesh adaption process, was monitored by the velocity magnitude of the BCA-inlet and ICA-, FA-outlets, shown in Fig. 3.1.

3.2 Results and Discussion

The geometry does not contain the major neck veins, hence the pressure value in Fig. 3.2 is not directly comparable with blood pressure measures. It is desirable to include as many geometric details as possible for further studies,

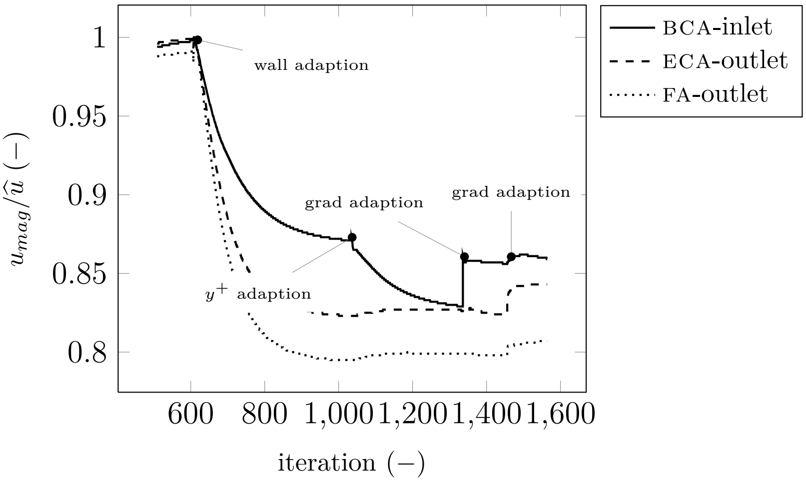

Figure 3.1: The mesh quality is examined by monitoring mass averaged velocity at pressure inlet and two pressure outlets, using the k-ω turbulence model and taking blood as a *Newtonian* medium with the highest *Reynolds* number $Re = 3972$. The velocity is normalized for each variable with its maximum value. The first mesh adaption for all cells adjacent to the wall results in decreasing velocity values. The change after the wall y^+ adaption in the smaller arteries (ECA and FA-outlet) is marginal, the maximum value of wall y^+ is 5.9. The following velocity gradient adaption was stopped when the value change was below 3 %.

meaning major neck veins and a model including smaller peripheral arterial and venous blood vessels. The *Reynolds* number was calculated on a cross section near the pressure inlet BCA with the velocity magnitude. The cross sectional area is $1.071377 \cdot 10^{-4}\,\mathrm{m}^2$, and (2.69) the approximately spare diameter is $1.1679553 \cdot 10^{-2}\,\mathrm{m}$.

3.2.1 Variation of the Reynolds Number

After finding an appropriate mesh, a series of simulations was made. It was decided to vary the *Reynolds* number in eight steps at the pressure inlet BCA in a typical range $676 \leq Re \leq 3972$, given by [13, p. 79], shown in Tab. 1.1 for the brachiocephalic artery. As boundary condition, the BCA is set as a pressure inlet with a range of $500 < p < 3000\,\mathrm{Pa}$. All other limits of the model are pressure outlets with $p = 0\,\mathrm{Pa}$. First, the fluid model of blood was *Newtonian* and the k-ω turbulence model was used, with turbulent parameters for the whole range of *Reynolds* number. In Fig. 3.3 velocity profiles for two line probes are visible for high, medium and low *Reynolds* number. The flattened shape in Fig. 3.3(a) is due to the only partially developed flow near to the pressure inlet. This

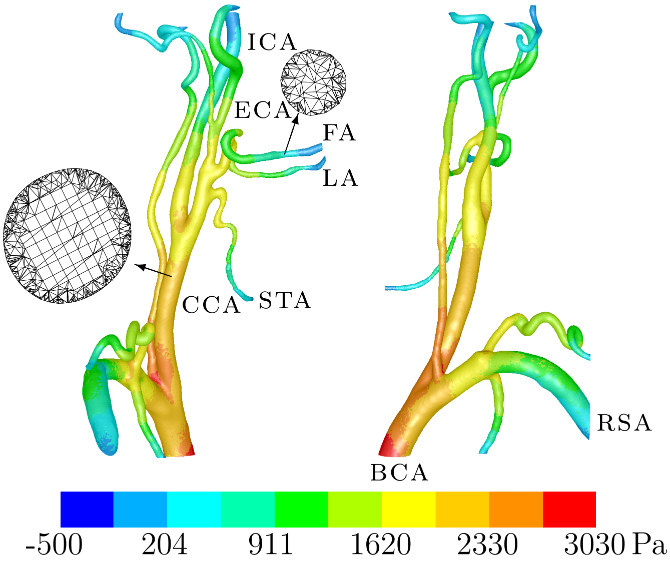

Figure 3.2: Total pressure on the wall for the highest *Reynolds* number $Re = 3972$. The k-ω turbulence model and blood as a *Newtonian* medium were used. The pressure inlet is the BCA. All other limits are pressure outlets. The mesh figures are cross sections through the CCA and FA.

region is in the entrance length of the flow. The asymmetric shape is a result of the BCA bend. The velocity function has an approximately parabolic shape in Fig. 3.3(b), which indicates laminar flow. The gradient of the velocity function depends on the *Reynolds* number level. Hence, the shear rate increases with increasing *Reynolds* number. The shear rate is essential for the non-*Newtonian* properties of blood, considered in later simulations.

3.2.2 Turbulence Parameters

The turbulence parameters were obtained as explained in Section 2.8.3, for fully developed turbulent pipe flows. The range of *Re* extends from laminar over transitional to turbulent, measured by the critical *Reynolds* number for pipe flows $Re = 2300$. However, in pulsatile blood flow it is unlikely that fully developed turbulent flow will occur. Neither the entrance length nor the time are long enough for a fully established turbulent flow, [12, p. 230] and [16, p. 43], respectively. Nevertheless low turbulent effects will be present and have to be taken into account. In a transient simulation, choosing between laminar and turbulent is required in pre processing.

Figure 3.4 shows the inlet part of the vessel on various *Reynolds* numbers and an iso-surface of turbulent viscosity ratio $\mu_T/\mu = 0.1$, and this is arbitrarily chosen. The value of μ_T/μ increases in the region inside the surface. The

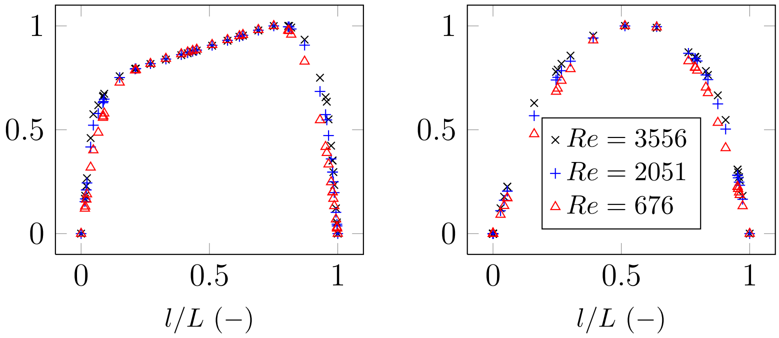

(a) Line-BCA.
(b) Line-ICA.

Figure 3.3: Velocity profiles with various *Reynolds* numbers at the pressure inlet. The k-ω turbulence model with turbulence parameters also in the laminar region and blood as *Newtonian* medium was used. The velocity is normalized for each variable with its maximum value to compare the qualitative velocity function. The velocity gradient near to the wall is rising with increasing *Reynolds* number. The length of line-BCA is $L = 0.0121\,\mathrm{m}$ and of line-ICA $L = 0.0057\,\mathrm{m}$.

contour levels show the specific dissipation rate ω. The turbulence is introduced by the user defined boundary condition. The zone where turbulent effects are present, shrinks with decreasing *Reynolds* number. The major dissipation occurs directly at the inlet.

3.2.3 Wall Shear Stress

The wall shear stress for various *Reynolds* numbers is shown in Fig. 3.5. The region with the highest stress is the bend from the BCA to RSA. After the bifurcation of the CCA into the ICA and ECA, there is a region with high wall shear stress on the ICA wall, easily visible on top of Fig. 3.5(a)-(d). The wall shear stress decreases with decreasing *Reynolds* number. Medically speaking, high wall shear stress can induce red blood cell damage, leading possibly to thrombosis (blood clotting) and in the worst case to a stroke, [4]. Additionally high wall shear stress can introduce acute vascular endothelial changes (vessel wall traumas), dealt with in [34].

Figure 3.5(h) with the smallest *Reynolds* number $Re = 676$, is comparable with an arterial stenoses model in [16, pp. 243–246]. This is a steady ideal model with an inner diameter of 8 mm on $Re = 483$. The wall shear stress beside the stenoses is approximately 3 Pa, and this is very similar to the stress level in the CCA in the present model on $Re = 676$. Further transient arterial stenoses models with a comparable wall shear stress level are found in [2] and [3].

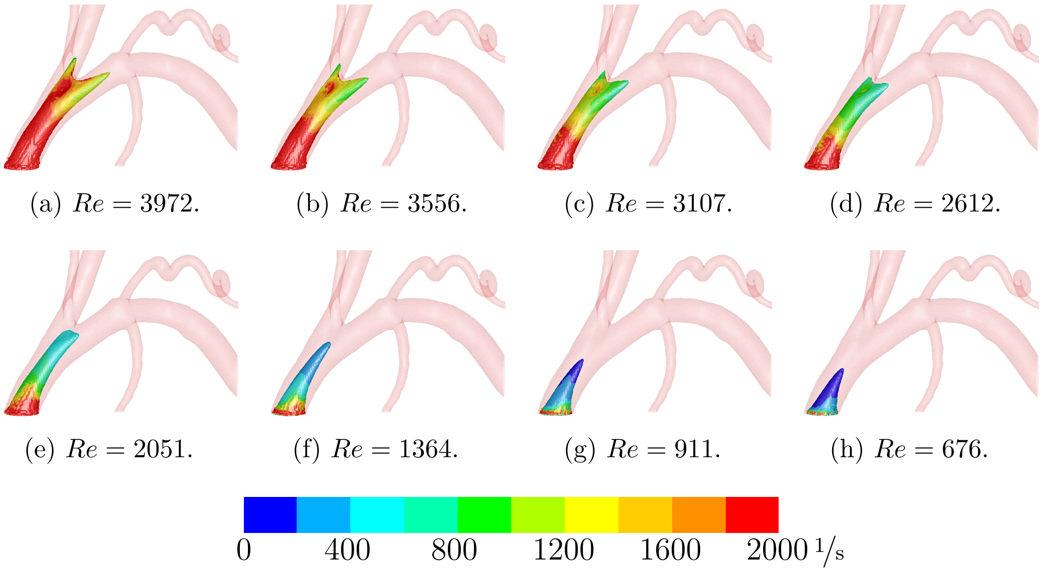
(a) $Re = 3972$. (b) $Re = 3556$. (c) $Re = 3107$. (d) $Re = 2612$.

(e) $Re = 2051$. (f) $Re = 1364$. (g) $Re = 911$. (h) $Re = 676$.

Figure 3.4: Specific dissipation rate ω plotted on an iso-surface of turbulent viscosity ratio $\mu_T/\mu = 0.1$ with varying *Reynolds* number of the pressure inlet. Inside this iso-surface is μ_T/μ ascending. In Fig. (e)-(h) on laminar *Reynolds* numbers, the impact of the boundary settings, $k, \omega > 0$ also in the laminar region, is visible. It is desirable to avoid induced turbulence from the BCA-inlet on low *Reynolds* numbers. The k-ω turbulence model and blood as a *Newtonian* medium was used.

3.2.4 Comparison of Various Models

Later on, simulations were done with various models such as; laminar viscous, SST k-ω and k-ω with various turbulence parameters and non-*Newtonian* fluid models. An overview of all cases is found in Tab. 3.1. The file number, boundary conditions and several results are listed. The first eight cases show the range of the inlet pressure descending from 3000 Pa to 150 Pa using the k-ω model, with k and ω values obtained for fully developed pipe flow. This is undesirable for low *Reynolds* numbers. In laminar flow, the turbulent parameters k and ω should be set to zero, and this was done in the next simulations, file 20 to 23. The difference between the SST k-ω model and the laminar model is negligible for low *Reynolds* numbers, compare the results in Tab. 3.1 for 150 Pa inlet pressure (file 14, 15 and 24). Significantly, the SST k-ω model seems to produce the same results for $k = \omega = 0$ and small values of k and ω at the BCA-inlet. This is not the case in the k-ω model. Comparing file 13 and 23, the *Reynolds* number is decreasing at the BCA-inlet.

Generally, the results are the same in low *Reynolds* numbers with all models

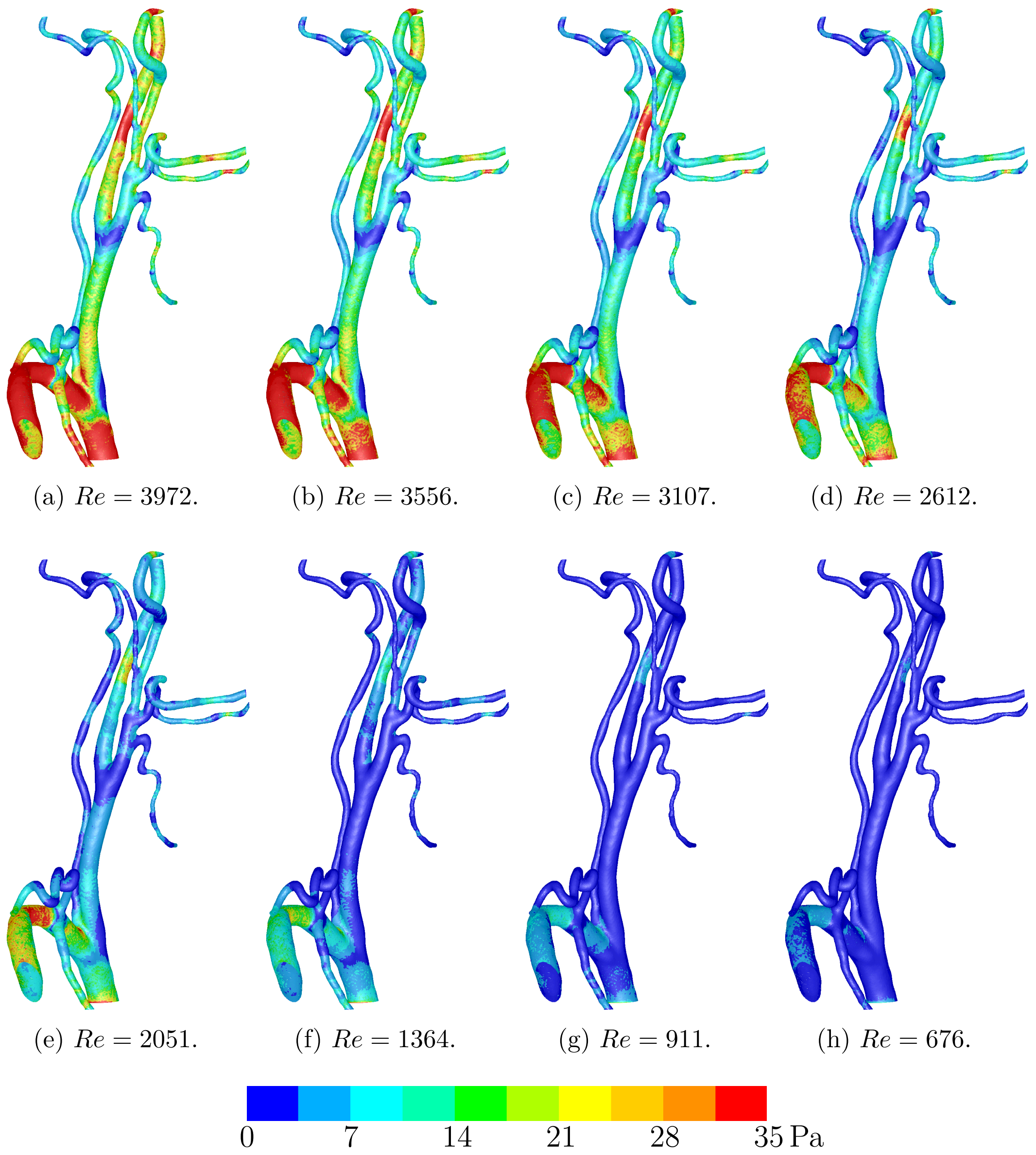

(a) $Re = 3972$.
(b) $Re = 3556$.
(c) $Re = 3107$.
(d) $Re = 2612$.
(e) $Re = 2051$.
(f) $Re = 1364$.
(g) $Re = 911$.
(h) $Re = 676$.

Figure 3.5: Wall shear stress with varying *Reynolds* number at the pressure inlet. The k-ω turbulence model with $k, \omega > 0$ also in the laminar region and blood as *Newtonian* medium was used. The colour label is limited to 35 Pa. The maximum value in Fig. (a) is approximately 90 Pa.

Table 3.1: Pressure and turbulence parameters as boundary condition at BCA inlet. Velocity and *Reynolds* number at inlet cross section and velocities at outlets.

	boundary BCA			BCA cross		outlets u_{mag} ($^{m}/_{s}$)				
#	p	$k \cdot 10^{-5}$	ω	u_{mag}	Re	ICA	ECA	FA	LA	STA
	(Pa)	($^{m^2}/_{s^2}$)	($^{1}/_{s}$)	($^{m}/_{s}$)						
		k-ω								
06	3000	597	172.55	1.111	3972	0.660	0.692	0.376	0.308	0.262
07	2500	492	156.64	0.995	3556	0.592	0.617	0.334	0.272	0.232
08	2000	388	139.17	0.896	3107	0.519	0.536	0.290	0.233	0.200
09	1500	287	119.57	0.731	2612	0.437	0.448	0.241	0.190	0.165
10	1000	188	96.78	0.574	2051	0.344	0.348	0.186	0.143	0.126
11	500	92	67.74	0.382	1364	0.228	0.227	0.120	0.087	0.078
12	250	45	47.59	0.255	911	0.151	0.148	0.076	0.052	0.048
13	150	27	36.65	0.189	676	0.110	0.106	0.053	0.036	0.032
20	1000	0	0	0.565	2020	0.343	0.348	0.186	0.143	0.125
21	500	0	0	0.376	1344	0.227	0.227	0.119	0.087	0.078
22	250	0	0	0.251	897	0.150	0.147	0.076	0.052	0.047
23	150	0	0	0.186	665	0.110	0.106	0.053	0.035	0.032
		laminar								
14	150	-	-	0.188	672	0.109	0.105	0.052	0.034	0.031
18	3000	-	-	1.136	4061	0.676	0.706	0.380	0.310	0.262
		SST k-ω								
15	150	27	36.65	0.189	676	0.110	0.106	0.053	0.036	0.032
24	150	0	0	0.189	676	0.110	0.106	0.053	0.036	0.032
19	3000	597	172.55	1.110	3968	0.660	0.692	0.376	0.308	0.262
		k-ω, *Power-law*								
16	150	0	0	0.180	643	0.100	0.092	0.044	0.028	0.024
17	3000	597	172.55	1.110	3968	0.660	0.692	0.375	0.307	0.262
		SST k-ω, *Carreau*								
25	150	0	0	0.182	651	0.102	0.096	0.046	0.030	0.026
26	3000	597	172.55	1.104	3947	0.660	0.690	0.371	0.303	0.260

at the outlets. The flow is laminarized at the outlets. As expected, the laminar model produces different results to both *k*-ω models on high *Reynolds* numbers. (Compare the results for 3000 Pa inlet pressure in Tab. 3.1). Both *k*-ω models provide similar results for the outlets (file 06 and 19). The laminar model is inappropriate for this *Reynolds* number and even at the small outlets causes, where the flow is already laminarized, different velocity values in comparison with the *k*-ω models (file 18).

A more accurate statement can be made with Fig. 3.6. The velocity profiles are shown for line probes at the pressure inlet BCA and a pressure outlet ICA. The difference between the SST *k*-ω model and the laminar viscous model is negligible for low *Reynolds* numbers, Fig. 3.6(a). Just the *k*-ω model with $k = \omega = 0$ deviates from all other cases, and this is insufficient. The SST *k*-ω model is appropriate for low *Reynolds* number flow and produces constant results. The difference between both *k*-ω models on high *Reynolds* number is marginal, Fig. 3.6(b). Due to the required non zero turbulence parameters, the *k*-ω model indicates turbulent flow also in low *Reynolds* numbers (inlet pressure 150 Pa) at the BCA-inlet, shown in Fig. 3.6(c). The SST *k*-ω model deals better with $k = \omega = 0$ and computes zero turbulence intensity on low inlet pressure, shown in Fig. 3.6(d). The turbulence range for the inlet (line-BCA) extends from non to medium turbulence. The outlet level is smaller. The plot on line-ICA shows increasing turbulence near the wall for 3000 Pa inlet pressure. The definition of the three thresholds low, medium and high turbulence is given in Section 2.8.

Figure 3.7 shows the influence of the material models on the simulation results. For small vessels on small *Reynolds* numbers it is not valid to use a *Newtonian* model, shown by Fig. 3.7(b). The influence decreases with higher *Reynolds* numbers and increasing vessel diameter, Fig. 3.7(a) and (c).

3.2.5 Turbulence

The turbulent kinetic energy and velocity vectors are shown in Fig. 3.8 for the upper part of the model. The transitional flow enters the model on inlet *Reynolds* number 2612. In the lower CCA the shape of velocity vectors indicates a laminar flow. The near to zero turbulent kinetic energy in this region provides further evidence of this. At the branch into ICA and ECA, the flow becomes turbulent near the wall, downstream in the ICA. The flow separates at the inner wall of the branching. Due to the streamline curvature, a distinctive secondary flow occurs downstream. And this is presented by velocity vectors in cross sectional plains in Fig. 3.8 on the right. Turbulence and the associated fluctuations of wall shear stress can cause the mentioned haemolysis (red blood cell damage), and this is studied in [32].

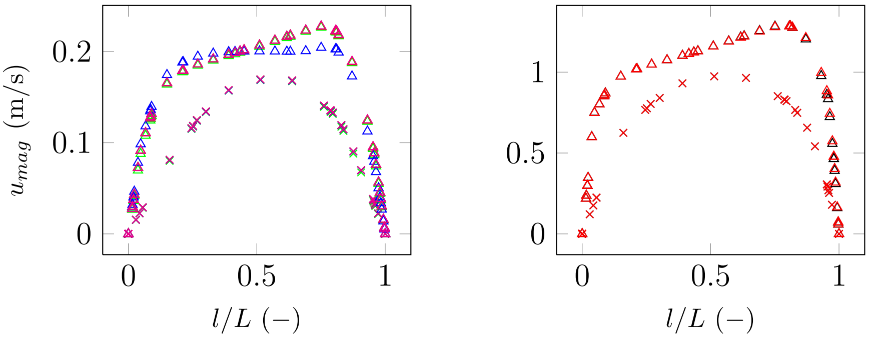

(a) Inlet pressure 150 Pa, black: k-ω with $k, \omega > 0$, green: laminar, red: SST k-ω with $k, \omega > 0$, blue: k-ω with $k, \omega = 0$, magenta: SST k-ω with $k, \omega = 0$.

(b) Inlet pressure 3000 Pa, black: k-ω, red: SST k-ω.

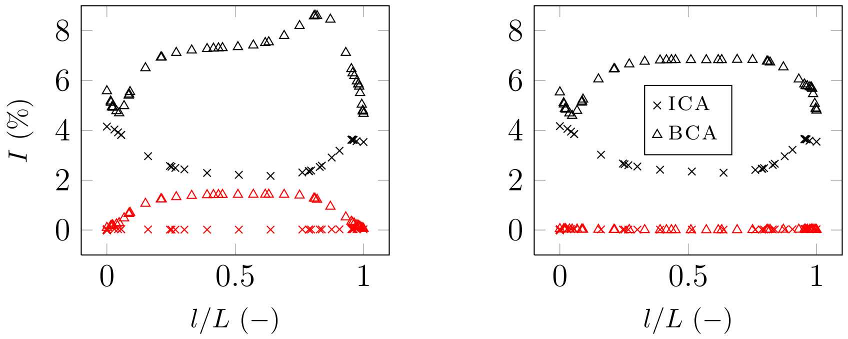

(c) k-ω with $k, \omega > 0$, black: inlet pressure 3000 Pa, red: inlet pressure 150 Pa.

(d) SST k-ω with $k, \omega = 0$, black: inlet pressure 3000 Pa, red: inlet pressure 150 Pa.

Figure 3.6: Velocity profiles of line probe ICA and BCA for low and high *Reynolds* numbers with various viscous model approaches, Fig. (a) and (b). In (a), the difference between SST k-ω model and laminar viscous model is negligible, the k-ω model is more sensitive to changing turbulence parameters. In Fig. (c) and (d) the turbulence intensity is shown. The blood fluid model is *Newtonian* in all figures.

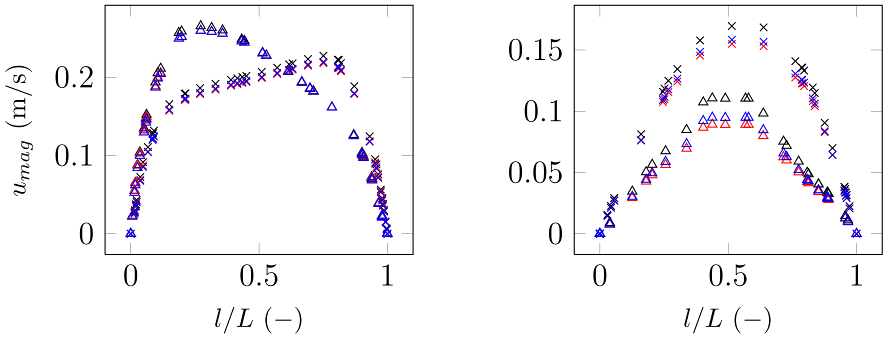

(a) Inlet pressure 150 Pa, ×-BCA, △-RSA.

(b) Inlet pressure 150 Pa, ×-ICA, △-FA.

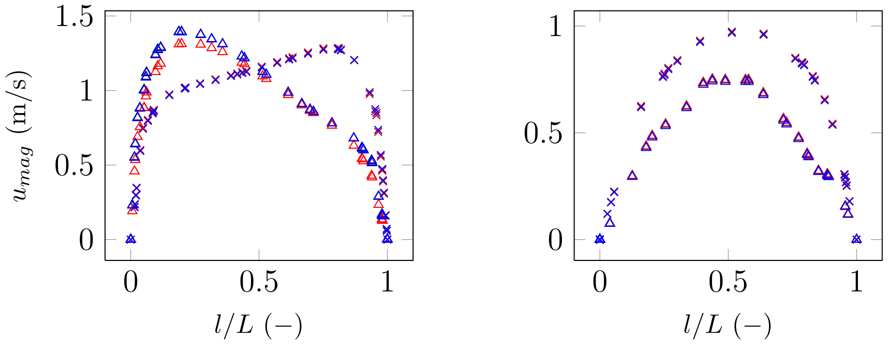

(c) Inlet pressure 3000 Pa, ×-BCA, △-RSA.

(d) Inlet pressure 3000 Pa, ×-ICA, △-FA.

Figure 3.7: Velocity profiles with various blood models. Black markers show blood as a *Newtonian* medium, red markers as non-*Newtonian Power-law* and blue markers as *Carreau* model. The k-ω turbulence model with $k, \omega > 0$ also in the laminar region was used for *Newtonian* and *Power-law*. The SST k-ω model was used for the *Carreau* model. The non-*Newtonian* approach results in most cases in lower velocity values, due to more viscosity on low shear rate. This effect is more relevant in low *Reynolds* number flow and in small vessels. The maximum difference between all material models is approximately 20 %, shown in Fig. (b). In contrast, Fig. (d) shows approximately similar functions. The length of line-BCA is $L = 0.0121\,\mathrm{m}$, of line-RSA $L = 0.0093\,\mathrm{m}$, of line-ICA $L = 0.0057\,\mathrm{m}$ and of line-FA $L = 0.0029\,\mathrm{m}$.

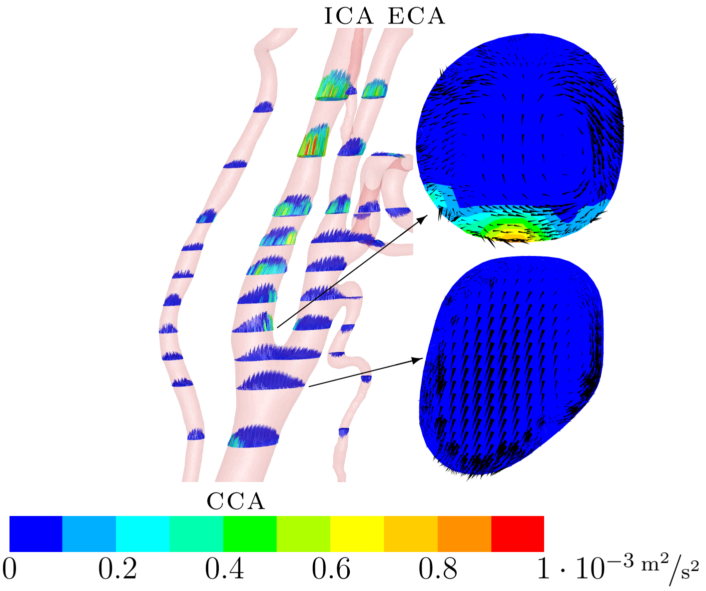

Figure 3.8: Turbulent kinetic energy with velocity vectors at $Re = 2612$ and inlet pressure 1500 Pa. On the right are two cross sections through the CCA shown with two dimensional velocity vectors in plain. After the bifurcation of the CCA into the ICA and ECA turbulence is produced and is visible in the ICA. The *k*-ω turbulence model and blood as a *Newtonian* medium were used.

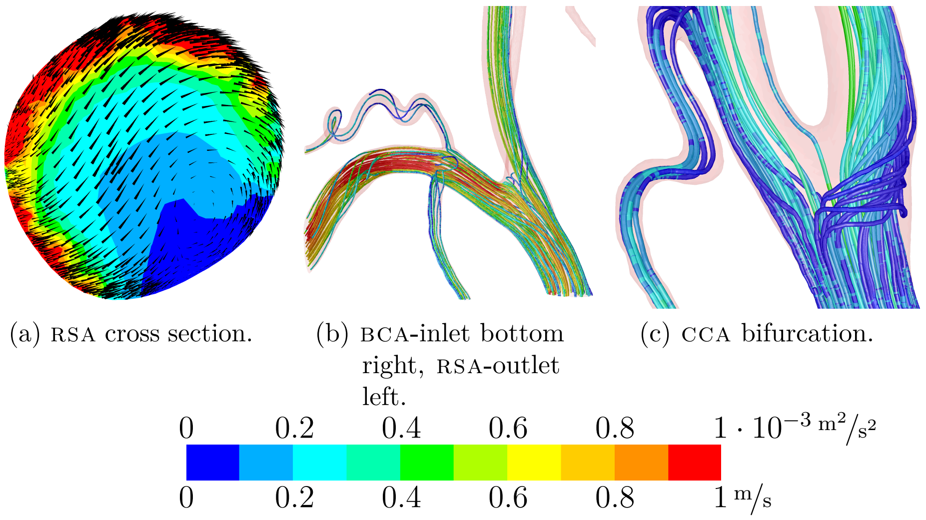
(a) RSA cross section.

(b) BCA-inlet bottom right, RSA-outlet left.

(c) CCA bifurcation.

Figure 3.9: Figure (a) shows the RSA cross section with coloured turbulent kinetic energy and velocity vectors in plain. In Fig. (b) and (c) the velocity magnitude is plotted on path lines. All Figures are on $Re = 2612$ and inlet pressure 1500 Pa, using *k*-ω turbulence model and blood as *Newtonian* medium.

A more detailed statement can be made with Fig. 3.9. In (a) a cross section through the RSA is shown with coloured turbulent kinetic energy and velocity vectors in plain. Again, a secondary flow occurs because of the arterial bend. As dealt with in [14, p. 736] for the aorta, the inner curvature is greater then the outer curvature in the present model. The lower pressure on the inner curvature, compared to Fig. 3.2 right, causes the boundary-layer flow to accelerate increasingly. Due to the centrifugal force, a secondary flow forms downstream. A secondary velocity component (perpendicular to the streamlines) is superimposed on the main flow. This component induces secondary vortices. The streamlines coloured with the velocity magnitude in Fig. (b) and (c) show these secondary flows. In Fig. (c) a region of recirculation at the inner right branch is visible. These haemodynamic factors play a significant role in the detection of atherosclerosis, which is an accumulation of fatty material in the intima (inner layer) of arteries. This cardiovascular disease is often present in artery bifurcations and bends caused by flow recirculation, [5].

3.3 Conclusions

The results of the steady simulation are feasible and comparable with other CFD simulations. It is desirable to include more geometric details in the model, particularly major neck veins and smaller peripheral blood vessels. A mesh independent solution is produced with wall y^+ and pressure gradient adaption in FLUENT. A maximum value of $y^+ = 5$ is desirable. At the inlet region, the SST k-ω model is more independent of the turbulence parameters k and ω than the k-ω model. All following simulations should be made with the SST version and $k = \omega = 0$ for low *Reynolds* numbers. The SST k-ω turbulence model is able to provide approximately similar results as the laminar viscous model for low *Reynolds* numbers, hence it is appropriate for the whole *Reynolds* number range.

For further simulations the *Newtonian* fluid model approach is not desirable. Small arteries on low *Reynolds* number values require a non-*Newtonian* fluid model with increasing viscosity on low shear rates. Comparing two non-*Newtonian* models, *Power-law* and *Carreau*, a slight difference was shown. In general the *Carreau* model approximates the blood viscosity more realistically than the *Power-law* model. Depending on the available computer resources, the influence of a second order discretization on the simulation should be investigated.

A study of the fluid structure interaction is necessary to estimate the influence of the vessel deformation on the simulation results. Therefore a multi physics software is required, for instance COMSOL.

4 Two-component simulation

Considering the pulsatile character of blood flow, a transient CFD model is required. The model is reduced to the interesting region of the CCA bifurcation, the LA, FA and STA branch, including two-component flow. In particular the CFD model comprises the two liquids blood (continuous component or primary phase) and the chemical agent cisplatin (dispersed component or secondary phase). As described in Section 1.3, cisplatin is injected via a catheter into the arterial blood flow. Due to this, the catheter has to be considered as thin pipe inside the CCA, because the catheter walls cause wall friction and influence the haemodynamic flow pattern.

4.1 Geometry

The catheter is an ideal pipe and in clinical practice has an inner diameter of 0.625 mm, an outer diameter of 0.924 mm and the common dose rate is approximately 50 ml/20 s [85] (Section A.6). Four different injection positions are common:

- Short before the common carotid bifurcation.
- Internal carotid artery at the height of the superior thyroid branch.
- Lingual shunt.
- Inside the lingual artery.

It was decided to begin with the first injection position, because the catheter can be modelled as straight ideal pipe, shown in Fig. 4.1(a). As discussed in Section 2.2 small pipe geometry creation using few voxels is complicated in SCANIP. Hence, it is impossible to model the catheter entirely including inner and outer wall in such small dimensions.

A catheter outer wall diameter of approximately 1.2 mm (this is 30 % larger than the real catheter) and tolerable wall smoothness was achieved with the CAD primitive generation tools in SCANIP. An additional volume at the interface of catheter outlet and blood was created to obtain an inner surface in the following mesh import in GAMBIT. Using the split face tool in GAMBIT, this interface was divided by a circle of 0.6 mm diameter and an ideal circular face for the

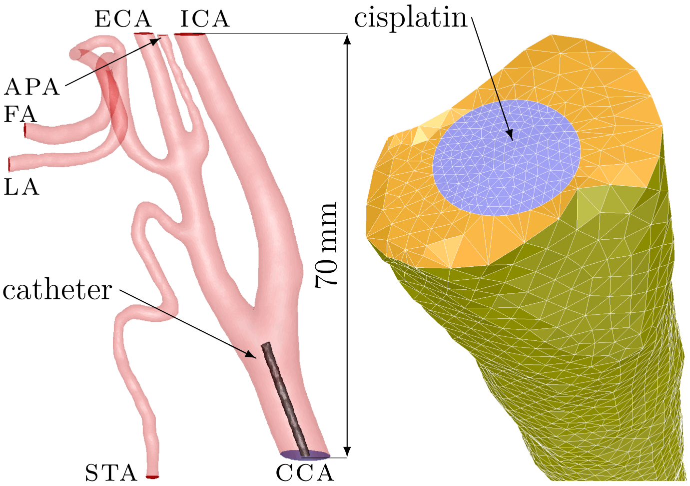

(a) Two-component model.

(b) Catheter.

Figure 4.1: Two-component model considering the cisplatin injection through a catheter, right before the CCA bifurcation. Figure (b) shows the meshed catheter wall, which is acceptably smooth but not ideally cylindric. The front surface is divided into the cisplatin inlet and the front wall.

catheter boundary condition was obtained. This face is slightly smaller than the real catheter, shown in Fig. 4.1(b). Since the catheter inner wall is not considered in the model, it was decided to neglect the cisplatin flow inside the catheter completely and this region remains unmeshed. Otherwise recircluation would occur inside the catheter near the catheter-blood interface. Additionally the steady ideal pipe flow of cisplatin inside the catheter is entirely solvable with the analytical equations of Section 2.1.2. So there is no need to include this region in a CFD simulation, because this would cause longer computation time and does not lead to greater knowledge.

4.2 Mesh

The mesh consists of hexahedron elements in the vessel core and tetrahedron elements adjacent to walls. A mesh independence test was done in a previous steady simulation on the highest flow rate of CCA using wall y^+ adaption as explained in Section 2.5. Due to just slightly monitor data changes after mesh adaption, the initial mesh of GAMBIT was taken, with a mesh size of 224115 cells.

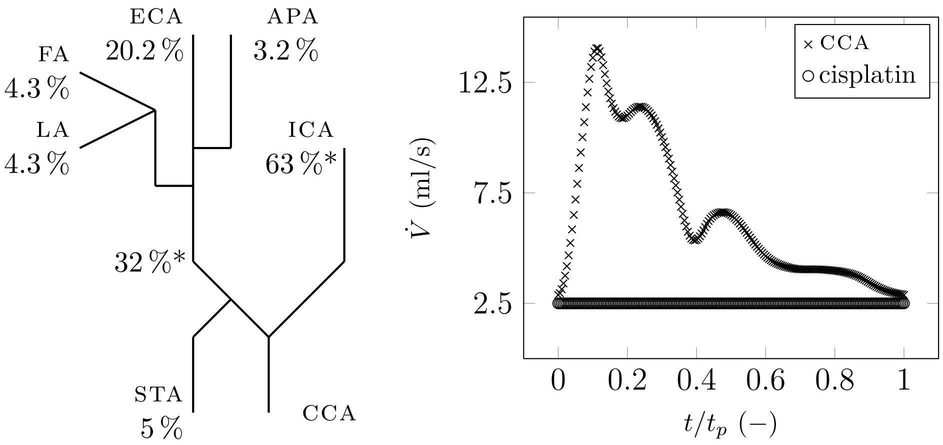

(a) Flow rate weighting.

(b) Inlet boundary conditions.

Figure 4.2: Boundary conditions used in the two-component simulation. Figure (a) shows the time continuous flow rate weighting off all outlets using the outflow condition. The asterisked values are the original time averaged data of [78]. The CCA flow rate inlet condition in Fig. (b) is realized as a transient table with 200 equal distant time steps ($0.0047\,\mathrm{s}$ time step size), as well as cisplatin with a constant value of $2.5\,\mathrm{ml/s}$. The cycle time t_p is $0.923\,\mathrm{s}$, which is equal to 65 heart beats per minute. In FLUENT, the flow rates are converted in mass fluxes ($\mathrm{kg/s{\cdot}m^2}$) using the correspondent component density and inlet area.

4.3 Boundary Conditions

The boundary conditions comprise two mass flow inlets, CCA and catheter, and six outflow outlets with adjusted flow rate weighting. Several measured data dealing with CCA blood flow pattern is already presented in Section 2.10. It is assumed that the additional catheter inlet in the present model does not change the general flow division in the CCA bifurcation, due to the modelled catheter position still being inside the CCA. This is not advisable if the injection position moves downstream, for instance to the ECA. The most appropriate data is given in [78], shown in Fig. 2.20(e) and (f) obtained from older volunteers. However, it can be expected that because of the stress during chemotherapy, the heart rate should be higher than the reported 65 beats per minute in this source. Additionally, the study was made with healthy volunteers. Hence, it is not known how a catheter will affect the reported rate of flow range.

Unfortunately it is impossible to consider a time dependent flow rate weighting of the CCA into the ECA and ICA, shown in Fig. 2.20(f), in the transient solver of FLUENT as a boundary condition for each outlet. Hence, only a time averaged flow rate weighting could be used. The time averaged mass loss (ICA + ECA)/ECA is reported at roughly 5 % in [78]. Two additional sources report approximately 7 % mass loss, summarized in Tab. 2.3. Regarding this 5 % to the STA branch, it is assumed that each branch of the ICA will have the same proportion of approximately 13.5 % of the ICA mass flow. The time averaged mass flow division was calculated for the ECA, STA, LA, FA and APA outlet and assumed for the ICA outlet. Figure 4.2(a) provides an overview of the time continuous flow rate weighting for all outflow conditons. The rate of flow wave function, using 200 equal time steps, is shown in Fig. 4.2(b) for the CCA and cisplatin inlet. These two inlet conditions are converted into a mass flux boundary in the FLUENT simulation. In particular a transient table for the CCA and a constant value for cisplatin is used. The volume fraction of the dispersed phase cisplatin was set to 100 % at the cisplatin inlet and 0 % at the CCA inlet.

Blood is modelled as a non-*Newtonian* fluid using the *Carreau* model with the parameters of Tab. 2.2. The maximum *Reynolds* number of the pulsatile blood flow is 856, which means laminar flow. A *Newtonian* material model was used for cisplatin with properties of water, this is given in Section 2.6.2. All walls are rigid and a non-slip condition is prescribed. The *Reynolds* number of the steady cisplatin flow in the catheter is 5331. This is far above the commonly known threshold for laminar pipe flow $Re = 2300$. Turbulence is considered through the SST k-ω model with $k, \omega = 0$ at the CCA inlet and by using the approach of Section 2.8.3 for fully developed turbulent pipe flow, $k = 0.359\,\mathrm{m^2/s^2}$, $\omega = 26165\,\mathrm{s^{-1}}$ for the turbulent cisplatin inlet on top of the catheter.

The mixing model was used including slip velocity and implicit body force effects. Assuming a bubble size of 0.1 mm for the dispersed phase cisplatin, a hydraulic diameter of $d_h = 6\,\mathrm{mm}$ for the CCA and a maximum blood velocity of $0.8\,\mathrm{m/s}$, a *Stokes* number of 0.021 was calculated using the equations of Section 2.9. This is much smaller than one and means that all cisplatin bubbles will closely follow the blood flow. A strong coupling between blood and cisplatin is supposed.

4.4 Solver Settings

After testing one initial cycle using 100 time steps, the transient simulation proceeded in batch mode using the 200 equal distant time steps of Fig. 4.2(b) for one additional cycle. Double precision, first order discretization and the pressure based segregated PISO solver including skewness and neighbour correction of one, were used with a convergence criteria of $1 \cdot 10^{-7}$ for the cisplatin volume fraction residual. All other settings remained at FLUENT default values. The

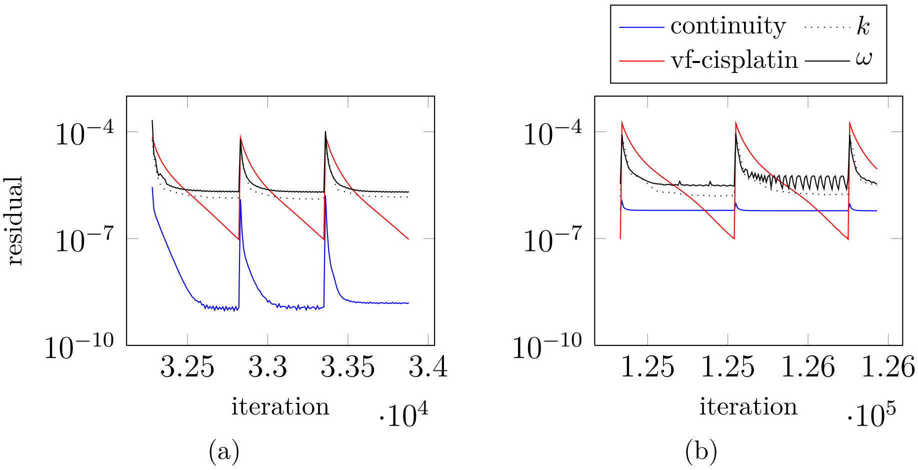

(a) (b)

Figure 4.3: Residuals shown for the first three time steps in Fig.(a) and time step 177 and 178 in Fig. (b). Each time step requires between 400–600 iterations until convergence of the cisplatin volume fraction residual.

energy equation was turned off during the simulation to speed up the process. And also because the temperature was fixed to 310.15 K on all boundaries. Data for each 10th time step was saved. The computing time required approximately four days, shared by three parallel processes.

4.5 Results and Discussion

A selection of residuals is presented in Fig. 4.3 for several time steps. The volume fraction residual of the dispersed phase is still decreasing. In future simulations the convergence criteria can be reduced further still. The continuity residual indicates a small numerical failure. Each time step required approximately 400–600 iterations. A maximum number of 800 iterations per time step is recommended.

4.5.1 Turbulence

Figure 4.4 shows vectors of velocity magnitude in several cross sections coloured by the turbulent kinetic energy k in the time step with the highest blood volume flow rate. The catheter inlet vectors in Fig. (a) are not exactly perpendicularly aligned with the catheter axis. The cisplatin flow is frontal orientated towards the inner wall of the CCA bifurcation with a small incline towards the ECA. Creation of the catheter geometry in CAD software would be useful to obtain a proper plain catheter front surface. This would be perpendicular, ideally

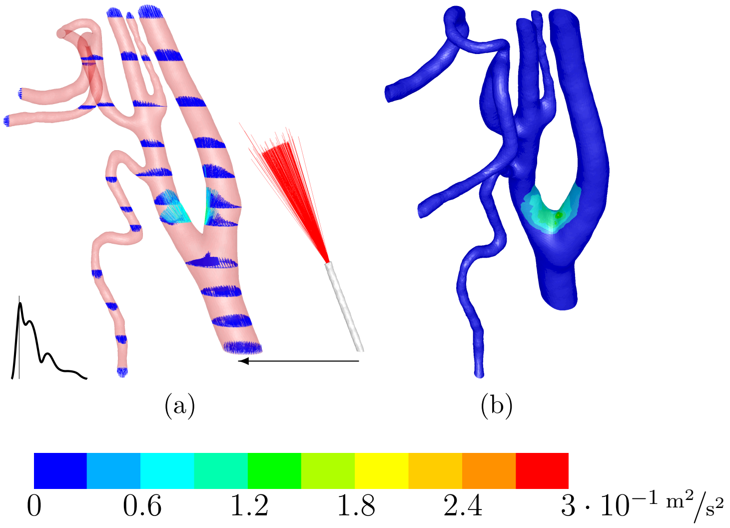
(a) (b)

Figure 4.4: Vectors of velocity magnitude coloured by turbulent kinetic energy k in Fig. (a). The catheter on the right is displaced from its origin in the CCA centre. The mean velocity at CCA inlet is $0.38\,\mathrm{m/s}$ and at cisplatin inlet $7.66\,\mathrm{m/s}$. Figure (b) shows the related contour plot. The colour bar is clipped, the maximum value of k is $0.4\,\mathrm{m^2/s^2}$ at cisplatin inlet.

cylindric and the catheter wall would be smooth. Because of the turbulent *Reynolds* number inside the catheter, turbulence is introduced in the blood flow through the cisplatin inlet. And it occurs at both inner walls after the CCA bifurcation in the ICA and ECA. The region on high turbulent kinetic energy, that indicates high turbulence and is shown in Fig. 4.4(b), is critical in matters of red blood cell damage (haemolysis) [31], thrombosis or even a stroke, dealt with in Section 1.1.3.

4.5.2 Wall Shear Stress

In consequence of the frontal orientated cisplatin inlet stream towards the CCA bifurcation wall, the wall shear stress shows a peak in this region, presented in Fig. 4.5(a) and (b) for systole and diastole, respectively. High wall shear stress can cause acute vascular endothelial changes, [34] already discussed in Section 1.1.3. Due to the toxic properties of cisplatin, this catheter inflow position can cause local inflammation [28], described in detail in Section 1.3.

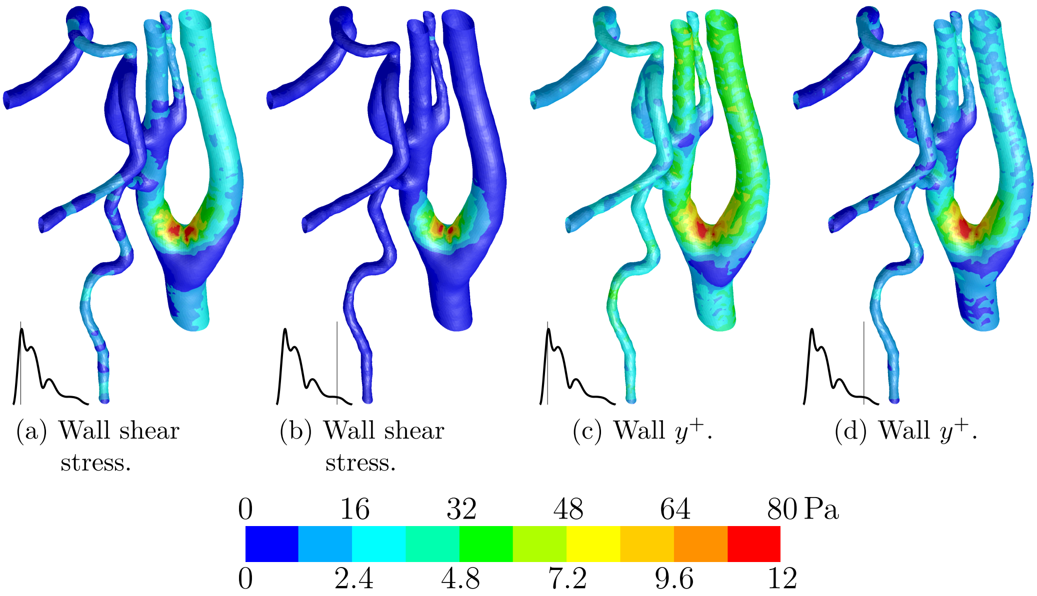

(a) Wall shear stress.

(b) Wall shear stress.

(c) Wall y^+.

(d) Wall y^+.

Figure 4.5: Wall shear stress and wall y^+ in systole and diastole. The colour bar is clipped, the maximum wall shear stress is 116 Pa in Fig. (a), the maximum wall y^+ is 13.6 in Fig. (c). On the bottom left the related blood flow boundary condition at the CCA is shown.

4.5.3 Mesh Quality

The mesh quality is sufficient in the most model regions $y^+ \leq 5$, apart from the region adjacent to the CCA bifurcation inner wall in Fig. 4.5(c) and (d). It is not expected that a finer mesh will change the qualitative cisplatin distribution in the model. However, this should be verified using further cycles of wall y^+ mesh adaption associated with a considerable longer computation time.

4.5.4 Cisplatin Distribution

The cisplatin distribution during one cardiac cycle can be described in detail by using Fig. 4.6(a)–(h). In general, the chemical agent cisplatin distributes in all arteries, as to be expected for this catheter position. This is undesirable, because only a high cisplatin concentration in a specific region gives maximum tumour control with minimum related side effects, as already mentioned in Section 1.1.3 and 1.3. Prior systole, the path lines indicate recirculation upstream in the CCA. The cisplatin volume fraction in the ECA is larger than in the ICA. This is explained by the flow rate weighting conditions of Fig. 4.2(a). With the start of systole and increasing blood flow, the cisplatin concentration decreases

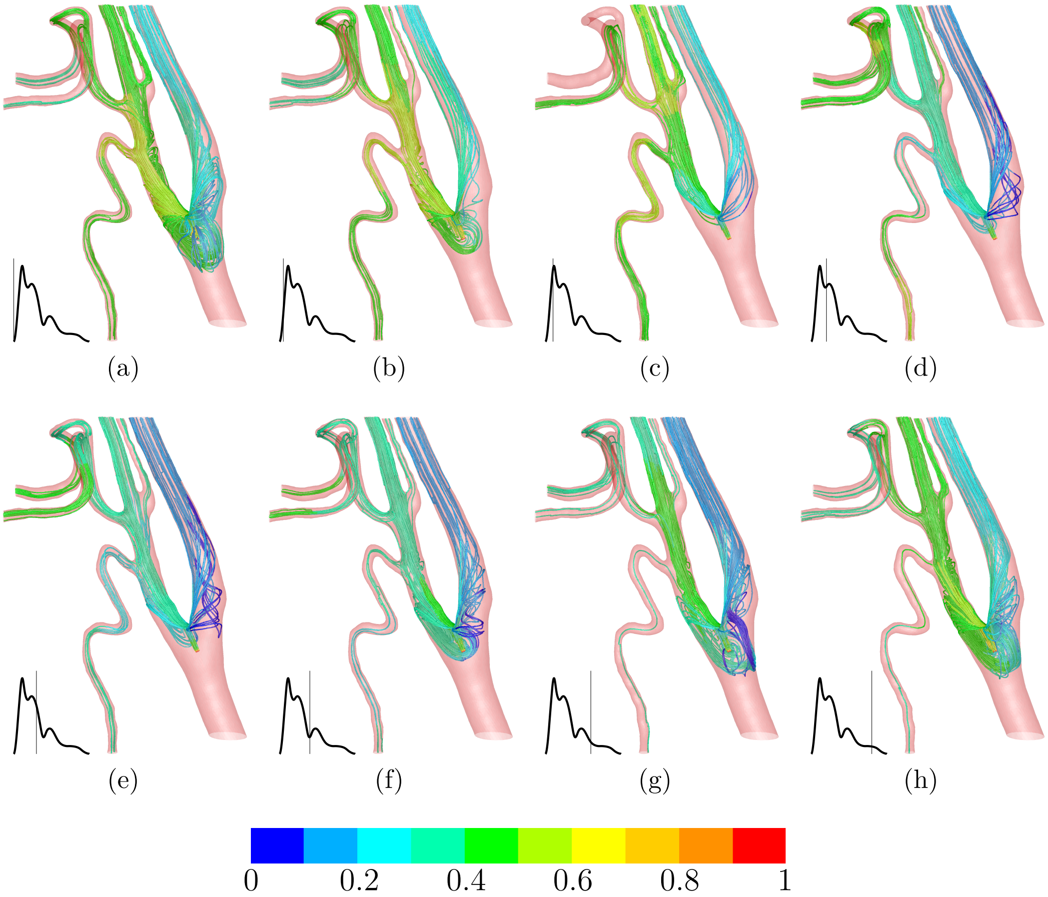
(a) (b) (c) (d)

(e) (f) (g) (h)

Figure 4.6: Path lines with origin cisplatin inlet coloured by volume fraction of cisplatin during one cardiac cycle. The catheter is hidden. The blood flow condition at the CCA inlet is show in each picture on the bottom left.

in the larger arteries ECA and ICA, Fig. (c)–(e) and the recirculation region disappears. There is a time shift in cisplatin volume fraction reduction to note between ECA and LA with FA. This is shown in Fig. (d). This shift is retained until the beginning of the diastole in Fig. (f) when the volume fraction in ECA, LA and FA are approximately equal. At the end of diastole in Fig. (g) a similar condition is observed as in Fig. (a). This suggests a periodic cisplatin distribution characteristic controlled by the cardiac cycle. It also shows the importance of considering a pulsatile blood flow boundary condition. If the simulation was steady, a delay in cisplatin concentration at various artery limits would be invisible in the simulation results.

The mass weighted average cisplatin volume fraction for all 21 saved time steps at all model outlets is presented in Fig. 4.7(a) and (b). The discussed

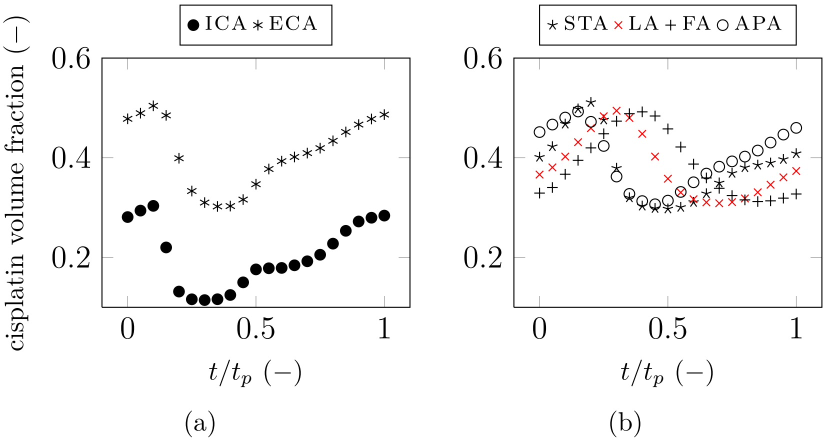

(a) (b)

Figure 4.7: Mass weighted average cisplatin volume fraction.

delay of cisplatin concentration between ICA and LA with FA is good to observe. In particular, the functions of ICA, ECA, STA and APA show a qualitatively similar shape contrary to the functions of LA and FA. Apart from the ICA all arteries have an approximately equal cisplatin concentration range between 0.3 and 0.5. It is not expected that a variation in cisplatin dosage will change this uniform distribution, rather a catheter position further downstream could have a positive effect in this matter.

Additionally, the time dependent cisplatin concentration functions, observed for all outlets, indicate that the time continuous boundary condition at the cisplatin inlet is not the most efficient technique for applying high chemical agent dosages. It is possible that an unsteady injection at a particular beneficial time range on higher dosage rate could enhance the cisplatin concentration and reduce side effects, such as local inflammation at artery walls, during the remaining period. An advantageous time range for injection would be between $t/t_p = 0$–0.3 during peak systole. Furthermore, it is possible that recirculation and the exposure time on high turbulence could be reduced by time dependent injection during systole.

In absolute values, Fig. 4.8(a) and (b) represent the rate of flow of the chemical. The prescribed flow rate weighting is the reason for the low level of STA, LA, FA and APA compared with ECA and ICA. The markers of the ICA in Fig. (a) are not fine enough to be resolved in early systole. Hence, it is possible that the presented maximum value is not the largest. Because of this a time integration, that would provide a volume value per cycle for each model limit, is not possible for the ICA. It is recommended to save more time steps in further computations.

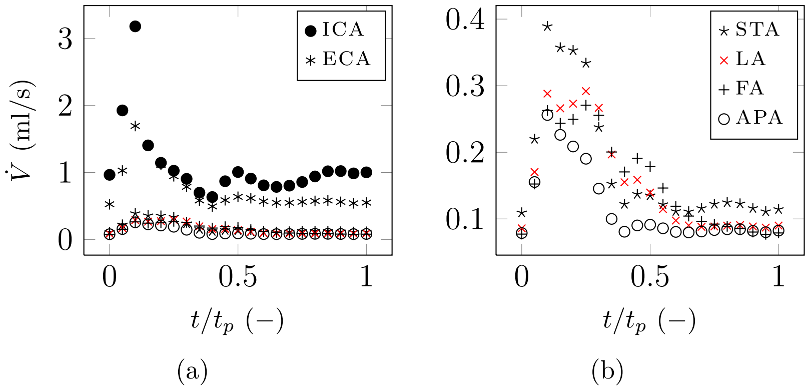

(a) (b)

Figure 4.8: Cisplatin rate of flow at the outlets. Figure (b) shows the outlets STA, LA, FA and APA of Fig. (a) separately with a finer ordinate resolution.

4.5.5 Time Step Independence

Finally, a time step independence test was made with 250 and 300 time steps. This is equal to 0.0037 s and 0.0031 s time step size. Each simulation was computed from the same initial file. Figure 4.9 provides significant evidence, that the initial used 200 time steps are fine enough resolved. The previous results are time step independent.

4.6 Conclusions

The simulation results are plausible and it can be assumed that the qualitative cisplatin distribution is correct. Experiments are strongly recommended to verify the quantitative results.

The used injection position gives an ineffective cisplatin division. This means that the chemical agent is distributed in all arteries and not in one specific tumour feeding artery, a fact of great importance. High wall shear stress and turbulence near the CCA bifurcation inner walls can cause serious harm, for instance acute vascular endothelial changes or haemolysis. It should be expected that an injection position in the core of the artery further downstream would reduce this high exposure. The time continuous cisplatin inlet condition seems to be ineffective during diastole, when upstream recirculation in the CCA mainly occurs. It should be investigated if a time dependent injection during the advantageous systole would lead to an equal cycle averaged cisplatin concentration with reduced side effects caused by the catheter inflow.

In blood flow CFD simulation using multiphase models, neither mass flow nor velocity outlets are practicable, due to required outlet data for each phase. This

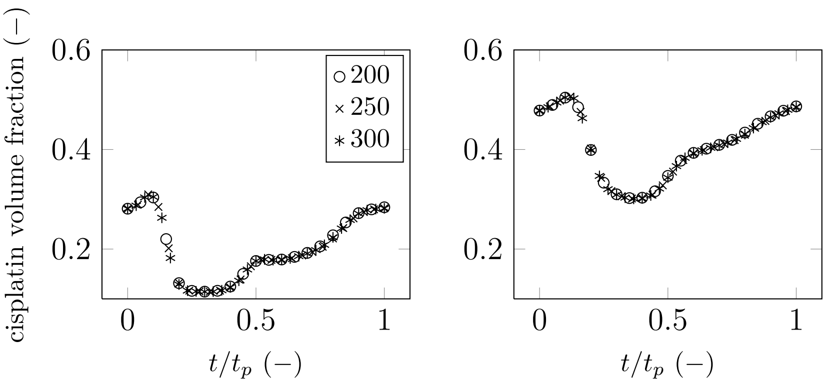

(a) ICA. (b) ECA.

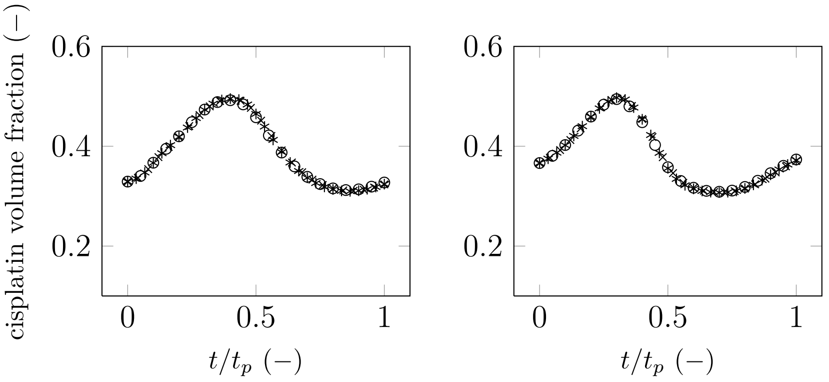

(c) FA. (d) LA.

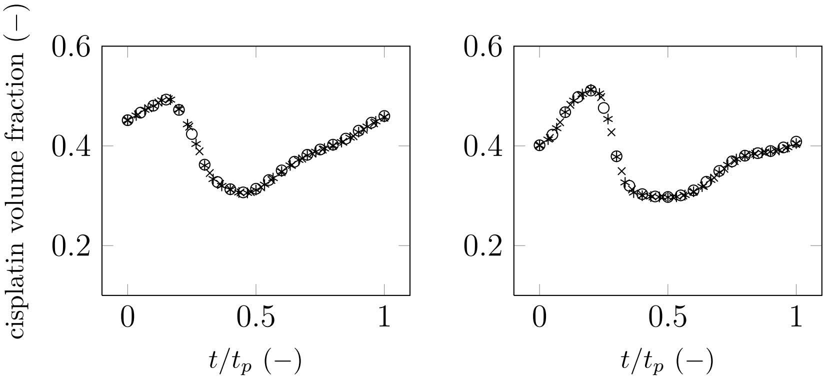

(e) APA. (f) STA.

Figure 4.9: Time step variation (200, 250, 300 time steps), monitored by mass weighted average cisplatin volume fraction for various artery outlets. Time step independence is achieved with 200 steps.

data is unknown a priori for the secondary phase cisplatin and is the aim of this simulation. An assumed flow rate weighting was used in this model based on measured data for the two main outlets ICA and ECA. The disadvantage is that the pressure is unrealistic by using the outflow condition in FLUENT and due to this, pressure results are not shown. Additionally it was impossible to consider the time dependent flow split between ICA and ECA. Hence, this simulation is not correct during systole. Furthermore this approach is only feasible for the presented catheter injection position, and this position is still before the CCA bifurcation. It is assumed that the general blood flow division remains unchanged in comparison with measured data of healthy volunteers in the normal state. An injection position further downstream in a side branch of the ECA would probably change the blood flow division. An alternative proper methodology would be to use the pressure inlet and outlet boundary conditions, that require only the volume fraction of the secondary phase at the inlets, and adjust the pressure to a correct level. However, time dependent pressure functions for each model boundary were not available and are difficult to assess for small arteries, such as the LA and FA. The implementation of an arterial one dimensional model seams to be the superior way for future CFD simulations dealt with in [50–55] and in Section 2.1.3 in this report.

A sub-step in the process from image data to a CFD mesh is desirable, meaning a CAD import, which offers much better geometry creation and boolean operation tools, independent of the image data's spatial resolution. This would lead to an ideal cylindric and smooth catheter geometry including inner and outer walls. Due to extensive large file sizes a model import using an IGES file, was unsuccessful because of low memory.

The time dependent blood flow boundary condition is realized as transient table with 200 equal distant time steps. Time step independence is verified. The implementation of a user defined function would offer the possibility to use adaptive time stepping in the transient solver. The time step size could be finer during systole and coarser during diastole, which is superior then a fixed time stepping.

The influence of several factors should be investigated, such as:

- The bubble size of the dispersed component cisplatin.
- FSI in comparison with rigid walls used in this model.
- The difference between the used mixture model and the *Eulerian* model.

In general, it is not known if the used mixing approach including bubble flow is appropriate or if a model of a chemical reaction would be more appropriate in this case.

5 Suggestions for future work

From the explanations in the previous chapters it is obvious, that a CFD simulation in chemotherapy is a nontrivial topic. Further investigation is required to optimize the injection method and to develop treatment guidelines. It was expected that it is impossible to include all natural phenomena in the presented simulation from the beginning. Hence, simplifications were required. This chapter lists some recommendations for future research.

In general, a validation with experiments is strongly recommended. For instance, by using a silicon model of the arterial network and laser *Doppler* velocimetry, the CFD mixture parameters can be adjusted. The implementation of a one dimensional arterial model seems to be useful, to obtain boundary conditions for each geometry. Neither in this project nor in the future is it probable that a full set of measured data for the blood flow (time dependent rate of flow and pressure at each artery limit) will be available. The use of CAD software is recommended to generate an ideal, bent and perfect smooth catheter for injection positions further downstream. Table 5.1 provides an overview of several assumptions, models and additional recommendations.

Table 5.1: Some models and principles for CFD chemotherapy simulation. The second column shows if the phenomenon is already considered in the model.

phenomenon	✓/✗	model	comment
fluid dynamics	✓	*Navier-Stokes* equations, finite volume method	appropriate for arteries not for micro circulation
turbulence	✓	SST k-ω	robust and appropriate
mixture	✓	mixture model	validation, variation of the bubble size and a comparison with the *Eulerian* model is required
pressure flow relationship	✗	one dimensional arterial model [50–56], applied in [57]	required to compute realistic pressure values and to consider wave reflection
vessel mechanics	✗	strain energy function	required for FSI
FSI	✗	ALE equations	FSI software and vessel wall thickness is required

REFERENCES

[1] M.M. Molla and M.C. Paul. LES of non-Newtonian physiological blood flow in a model of arterial stenosis, 2010. Submitted for publication in Medical Engineering & Physics. (Cited on pages 11, 43 and 44.)

[2] M.X. Li, J.J. Beech-Brandt, L.R. John, P.R. Hoskins, and W.J. Easson. Numerical analysis of pulsatile blood flow and vessel wall mechanics in different degrees of stenoses. *Journal of biomechanics*, 40(16):3715–3724, 2007. ISSN 0021-9290. doi: 10.1016/j.jbiomech.2007.06.023. URL `http://dx.doi.org/10.1016/j.jbiomech.2007.06.023`. (Cited on pages 11, 34 and 62.)

[3] A.S. Roy, L.H. Back, and R.K. Banerjee. Guidewire flow obstruction effect on pressure drop-flow relationship in moderate coronary artery stenosis. *Journal of biomechanics*, 39(5):853–864, 2006. ISSN 0021-9290. doi: 10.1016/j.jbiomech.2005.01.020. URL `http://dx.doi.org/10.1016/j.jbiomech.2005.01.020`. (Cited on pages 11 and 62.)

[4] M.C. Paul, M. Mamun Molla, and G. Roditi. Large-Eddy simulation of pulsatile blood flow. *Medical Engineering & Physics*, 31(1):153–159, 2009. ISSN 1350-4533. doi: 10.1016/j.medengphy.2008.04.014. URL `http://dx.doi.org/10.1016/j.medengphy.2008.04.014`. (Cited on pages 11, 16 and 62.)

[5] C.A. Taylor and C.A. Figueroa. Patient-Specific Modeling of Cardiovascular Mechanics. *Annu Rev Biomed Eng*, 11:109–134, 2009. doi: 10.1146/annurev.bioeng.10.061807.160521. URL `http://dx.doi.org/10.1146/annurev.bioeng.10.061807.160521`. (Cited on pages 11, 17, 28, 29 and 70.)

[6] D.A. Steinman, J.S. Milner, C.J. Norley, S.P. Lownie, and D.W. Holdsworth. Image-Based Computational Simulation of Flow Dynamics in a Giant Intracranial Aneurysm. *American Journal of Neuroradiology*, 24(4):559, 2003. URL `http://www.ajnr.org/cgi/reprint/24/4/559`. (Cited on pages 11, 16 and 28.)

[7] J. Cebral, R. Löhner, O. Soto, P. Choyke, and P. Yim. Patient-specific simulation of carotid artery stenting using computational fluid dynamics. In *Medical Image Computing and Computer-Assisted Intervention-MICCAI 2001*, pages 153–160. Springer, 2010. doi: 10.1007/3-540-45468-3_19. URL `http://dx.doi.org/10.1007/3-540-45468-3_19`. (Cited on pages 11 and 28.)

[8] D.A. Steinman. Image-based computational fluid dynamics modeling in realistic arterial geometries. *Annals of Biomedical Engineering*, 30(4):483–497, 2002.

ISSN 0090-6964. doi: 10.1114/1.1467679. URL `http://dx.doi.org/10.1114/1.1467679`. (Cited on pages 11, 17, 29, 35, 37 and 57.)

[9] T. Schenkel, S. Krittian, K. Spiegel, S. Höttges, M. Perschall, and H. Oertel. The Karlsruhe Heart Model KaHMo: A modular framework for numerical simulation of cardiac hemodynamics. In *IFMBE Proceedings Volume 25/4, World Congress on Medical Physics and Biomedical Engineering, September 7-12, 2009, Munich, Germany*, pages 615–618. Springer, September 2009. doi: 10.1007/978-3-642-03882-2_163. URL `http://dx.doi.org/10.1007/978-3-642-03882-2_163`. (Cited on pages 11 and 29.)

[10] I. Tohnai. Chemotherapy using intra-arterial infusion for oral cancer. *Nagoya Journal of Medical Science*, 68(3-4):101–108, 2006. ISSN 0027-7622. URL `http://ir.nul.nagoya-u.ac.jp/jspui/bitstream/2237/6962/1/p101_108.pdf`. (Cited on pages 11, 16, 18 and 19.)

[11] N. Fuwa, T. Kodaira, K. Furutani, H. Tachibana, T. Nakamura, R. Nakahara, T. Tomoda, H. Inokuchi, and T. Daimon. Intra-arterial chemoradiotherapy for locally advanced oral cavity cancer: analysis of therapeutic results in134 cases. *British journal of cancer*, 98(6):1039–1045, 2008. ISSN 0007-0920. doi: 10.1038/sj.bjc.6604272. URL `http://dx.doi.org/10.1038/sj.bjc.6604272`. (Cited on pages 11, 15 and 18.)

[12] H. Oertel, editor. *Bioströmungsmechanik : Grundlagen, Methoden und Phänomene*. Vieweg+Teubner / GWV Fachverlage, Wiesbaden, 2008. ISBN 978-3-8348-9554-7. doi: 10.1007/978-3-8348-9554-7. URL `http://dx.doi.org/10.1007/978-3-8348-9554-7`. (Cited on pages 12, 23, 43, 46 and 61.)

[13] Y.C. Fung. *Biodynamics : Circulation*. Springer, Berlin, 1984. ISBN 3-540-90867-6 ; 0-387-90867-6. (Cited on pages 12, 25, 30 and 60.)

[14] H. Oertel. *Prandtl-Essentials of Fluid Mechanics*. Applied Mathematical Sciences ; 158SpringerLink : Bücher. Springer Science+Business Media, LLC, New York, NY, 2010. ISBN 978-1-441-91564-1. doi: 10.1007/978-1-4419-1564-1. URL `http://dx.doi.org/10.1007/978-1-4419-1564-1`. (Cited on pages 13, 41, 43 and 70.)

[15] Wikipedia. Blood Wikipedia : The Free Encyclopedia. website, 2011. URL `http://en.wikipedia.org/wiki/Blood`. last checked 11/01/2011. (Cited on page 13.)

[16] K.B. Chandran, A.P. Yoganathan, and S.E. Rittgers. *Biofluid Mechanics : The Human Circulation*. Taylor & Francis Group, Boca Raton, Fl, 2006. ISBN 978-0-8493-7328-2. (Cited on pages 13, 14, 24, 25, 43, 55, 61 and 62.)

[17] L. Formaggia, A. Quarteroni, and A. Veneziani, editors. *Cardiovascular Mathematics : Modeling and simulation of the circulatory system.* MS&A ; 1SpringerLink : Bücher. Springer-Verlag Milan, Milano, 2009. ISBN 978-88-470-1152-6. doi: 10.1007/978-88-470-1152-6. URL `http://dx.doi.org/10.1007/978-88-470-1152-6`. (Cited on pages 14, 27, 30, 35, 42 and 44.)

[18] Y.C. Fung. *Biomechanics : mechanical properties of living tissues.* Springer, New York, NY, 2. ed. edition, 2004. ISBN 0-387-97947-6 ; 3-540-97947-6. (Cited on pages 14, 15 and 46.)

[19] Y.C. Fung. Elasticity of soft tissues in simple elongation. *American Journal of Physiology*, 213(6):1532, 1967. ISSN 0002-9513. (Cited on page 14.)

[20] Y.C. Fung. On mathematical models of stress-strain relationship for living soft tissues. *Mechanics of Composite Materials*, 11(5):726–740, 1975. ISSN 0191-5665. doi: 10.1007/BF00859649. URL `http://dx.doi.org/10.1007/BF00859649`. (Cited on page 14.)

[21] G.A. Holzapfel and R.W. Ogden, editors. *Biomechanical modelling at the molecular, cellular and tissue levels.* Springer Verlag, 2009. ISBN 978-3-211-95873-5. doi: 10.1007/978-3-211-95875-9. URL `http://dx.doi.org/10.1007/978-3-211-95875-9`. (Cited on pages 14, 45 and 46.)

[22] G.A. Holzapfel. Arterial Tissue in Health and Disease: Experimental Data, Collagen-Based Modeling and Simulation, Including Aortic Dissection. *Biomechanical Modelling at the Molecular, Cellular and Tissue Levels*, pages 259–344, 2009. doi: 10.1007/978-3-211-95875-9_4. URL `http://dx.doi.org/10.1007/978-3-211-95875-9_4`. (Cited on pages 14 and 46.)

[23] G.A. Holzapfel, T.C. Gasser, and R.W. Ogden. A new constitutive framework for arterial wall mechanics and a comparative study of material models. *Journal of elasticity*, 61(1):1–48, 2000. ISSN 0374-3535. doi: 10.1023/A:1010835316564. URL `http://dx.doi.org/10.1023/A:1010835316564`. (Cited on pages 14, 46 and 47.)

[24] G.A. Holzapfel and R.W. Ogden, editors. *Mechanics of biological tissue.* Springer Verlag, Berlin, 2006. ISBN 3-540-25194-4 ; 978-3-540-25194-1. (Cited on page 14.)

[25] D.W. Holdsworth, C.J.D. Norley, R. Frayne, D.A. Steinman, and B.K. Rutt. Characterization of common carotid artery blood-flow waveforms in normal human subjects. *Physiological Measurement*, 20:219, 1999. doi: 10.1088/0967-3334/20/3/301. URL `http://dx.doi.org/10.1088/0967-3334/20/3/301`. (Cited on pages 15, 55 and 56.)

[26] S.J. Vermeersch, E.R. Rietzschel, M.L. Buyzere, D.D. Bacquer, G.D. Backer, L.M. Bortel, T.C. Gillebert, P.R. Verdonck, and P. Segers. Determining carotid

artery pressure from scaled diameter waveforms: comparison and validation of calibration techniques in 2026 subjects. *Physiological Measurement*, 29:1267, 2008. doi: 10.1088/0967-3334/29/11/003. URL `http://dx.doi.org/10.1088/0967-3334/29/11/003`. (Cited on pages 15, 34, 56 and 57.)

[27] L.W.T. Alkureishi, R. De Bree, and G.L. Ross. RADPLAT: An Alternative to Surgery? *The Oncologist*, 11(5):469, 2006. doi: 10.1634/theoncologist.11-5-469. URL `http://dx.doi.org/10.1634/theoncologist.11-5-469`. (Cited on pages 15 and 18.)

[28] A.F. Kovács. Intraarterial chemotherapy and chemoembolization in head and neck cancer. Establishment as a neoadjuvant routine method. *Cancer Therapy*, 1:1–9, 2003. (Cited on pages 15, 19 and 76.)

[29] J.D. Humphrey and C.A. Taylor. Intracranial and abdominal aortic aneurysms: similarities, differences, and need for a new class of computational models. *Annual review of biomedical engineering*, 10:221, 2008. doi: 10.1146/annurev.bioeng.10.061807.160439. URL `http://dx.doi.org/10.1146/annurev.bioeng.10.061807.160439`. (Cited on page 16.)

[30] G. Xiong and C. Taylor. Virtual Stent Grafting in Personalized Surgical Planning for Treatment of Aortic Aneurysms Using Image-Based Computational Fluid Dynamics. *Medical Image Computing and Computer-Assisted Intervention-MICCAI 2010*, pages 375–382, 2010. doi: 10.1007/978-3-642-15711-0_47. URL `http://dx.doi.org/10.1007/978-3-642-15711-0_47`. (Cited on pages 16 and 28.)

[31] S.P. Sutera and M.H. Mehrjardi. Deformation and fragmentation of human red blood cells in turbulent shear flow. *Biophysical Journal*, 15(1):1–10, 1975. ISSN 0006-3495. doi: 10.1016/S0006-3495(75)85787-0. URL `http://dx.doi.org/10.1016/S0006-3495(75)85787-0`. (Cited on pages 16 and 76.)

[32] P.C. Lu, H.C. Lai, and J.S. Liu. A reevaluation and discussion on the threshold limit for hemolysis in a turbulent shear flow. *Journal of Biomechanics*, 34(10):1361–1364, 2001. ISSN 0021-9290. doi: 10.1016/S0021-9290(01)00084-7. URL `http://dx.doi.org/10.1016/S0021-9290(01)00084-7`. (Cited on pages 16 and 66.)

[33] R. Paul, J. Apel, S. Klaus, F. Schügner, P. Schwindke, and H. Reul. Shear stress related blood damage in laminar couette flow. *Artificial organs*, 27(6):517–529, 2003. ISSN 1525-1594. doi: 10.1046/j.1525-1594.2003.07103.x. URL `http://dx.doi.org/10.1046/j.1525-1594.2003.07103.x`. (Cited on page 16.)

[34] D.L. Fry. Acute vascular endothelial changes associated with increased blood velocity gradients. *Circulation Research*, 22(2):165, 1968. URL `http://circres.ahajournals.org/cgi/reprint/22/2/165.pdf`. (Cited on pages 16, 62 and 76.)

[35] D.N. Ku, D.P. Giddens, C.K. Zarins, and S. Glagov. Pulsatile flow and atherosclerosis in the human carotid bifurcation. Positive correlation between plaque location and low oscillating shear stress. *Arteriosclerosis, Thrombosis, and Vascular Biology*, 5(3):293, 1985. URL `http://atvb.ahajournals.org/cgi/reprint/5/3/293.pdf`. (Cited on page 17.)

[36] C.K. Zarins, D.P. Giddens, BK Bharadvaj, V.S. Sottiurai, R.F. Mabon, and S. Glagov. Carotid bifurcation atherosclerosis. Quantitative correlation of plaque localization with flow velocity profiles and wall shear stress. *Circulation Research*, 53(4):502, 1983. URL `http://circres.ahajournals.org/cgi/reprint/53/4/502.pdf`. (Cited on page 17.)

[37] C.G. Caro, J.M. Fitz-Gerald, and R.C. Schroter. Atheroma and arterial wall shear observation, correlation and proposal of a shear dependent mass transfer mechanism for atherogenesis. *Proceedings of the Royal Society of London. Series B, Biological Sciences*, 177(1046):109–133, 1971. ISSN 0080-4649. (Cited on page 17.)

[38] A.M.R. Agur and A.F. Dalley. *Grant's Atlas of Anatomy.* Lippincott Williams & Wilkins, 12. ed. edition, 2008. ISBN 978-0-7817-7055-2. (Cited on pages 17 and 18.)

[39] P. Köpf-Maier, editor. *Wolf-Heidegger's Atlas of Human Anatomy.* S. Karger Publishing, Basel, Freiburg, et al., 6., rev. and enlarged ed. edition, 2005. ISBN 3-8055-7668-4. (Cited on page 18.)

[40] W. Kirch, editor. *Encyclopedia of Public Health.* Springer Verlag Berlin Heidelberg, Dordrecht, 2008. ISBN 978-1-402-05614-7. doi: 10.1007/978-1-4020-5614-7. URL `http://dx.doi.org/10.1007/978-1-4020-5614-7`. (Cited on page 18.)

[41] J. Myers, editor. *Oral Cancer Metastasis.* Springer Verlag, New York, 2010. ISBN 978-1-4419-0774-5. doi: 10.1007/978-1-4419-0775-2. URL `http://dx.doi.org/10.1007/978-1-4419-0775-2`. (Cited on page 18.)

[42] D. Shannon. Fluid Mechanics in Cancer Treatment. Master's thesis, University of Glasgow, 2010. (Cited on page 19.)

[43] H.K. Versteeg and W. Malalasekera. *An Introduction to Computational Fluid Dynamics : The Finite Volume Method.* Pearson/Prentice Hall, Harlow, England et al., 2. ed. edition, 2007. ISBN 978-0-13-127498-3. (Cited on page 21.)

[44] J.H. Ferziger and M. Peric', editors. *Numerische Strömungsmechanik.* Springer-Verlag Berlin Heidelberg, Berlin, Heidelberg, 2008. ISBN 978-3-540-68228-8. doi: 10.1007/978-3-540-68228-8. URL `http://dx.doi.org/10.1007/978-3-540-68228-8`. (Cited on pages 21 and 51.)

[45] J.H. Ferziger and M. Peric'. *Computational Methods for Fluid Dynamics*. Springer, Berlin, 3., rev. ed. edition, 2002. ISBN 3-540-42074-6. (Cited on page 21.)

[46] E. Laurien and H. Oertel, editors. *Numerische Strömungsmechanik : Grundgleichungen und Modelle - Lösungsmethoden - Qualität und Genauigkeit*. Vieweg+Teubner Verlag / GWV Fachverlage GmbH, Wiesbaden, Wiesbaden, 3., vollständig überarbeitete und erweiterte auflage edition, 2009. ISBN 978-3-8348-9964-4. doi: 10.1007/978-3-8348-9964-4. URL `http://dx.doi.org/10.1007/978-3-8348-9964-4`. (Cited on pages 21, 48 and 54.)

[47] H.E. Siekmann and P.U. Thamsen, editors. *Strömungslehre für den Maschinenbau : Technik und Beispiele*. Springer-Lehrbuch. Springer Berlin Heidelberg, Berlin, Heidelberg, 2. ed. edition, 2009. ISBN 978-3-540-73990-6. doi: 10.1007/978-3-540-73990-6. URL `http://dx.doi.org/10.1007/978-3-540-73990-6`. (Cited on page 23.)

[48] D. Surek and S. Stempin, editors. *Angewandte Strömungsmechanik : für Praxis und Studium*. B.G. Teubner Verlag / GWV Fachverlage GmbH, Wiesbaden, Wiesbaden, 2007. ISBN 978-3-8351-9094-8. doi: 10.1007/978-3-8351-9094-8. URL `http://dx.doi.org/10.1007/978-3-8351-9094-8`. (Cited on page 24.)

[49] J.R. Womersley. Method for the calculation of velocity, rate of flow and viscous drag in arteries when the pressure gradient is known. *The journal of physiology*, 127(3):553, 1955. ISSN 0022-3751. URL `http://jp.physoc.org/content/127/3/553.full.pdf`. (Cited on page 25.)

[50] L.R. John. Forward electrical transmission line model of the human arterial system. *Medical and Biological Engineering and Computing*, 42(3):312–321, 2004. ISSN 0140-0118. doi: 10.1007/BF02344705. URL `http://dx.doi.org/10.1007/BF02344705`. (Cited on pages 26, 27, 82 and 83.)

[51] M.F. Snyder, V.C. Rideout, and R.J. Hillestad. Computer modeling of the human systemic arterial tree. *Journal of Biomechanics*, 1(4):341–353, 1968. ISSN 0021-9290. doi: 10.1016/0021-9290(68)90029-8. URL `http://dx.doi.org/10.1016/0021-9290(68)90029-8`. (Cited on pages 27, 82 and 83.)

[52] K. Chellappan, E. Zahedi, and M.A. Mohd Ali. Age-related Upper Limb Vascular System Windkessel Model using Photoplethysmography. In *3rd Kuala Lumpur International Conference on Biomedical Engineering 2006*, pages 563–566. Springer, 2007. doi: 10.1007/978-3-540-68017-8_141. URL `http://dx.doi.org/10.1007/978-3-540-68017-8_141`. (Cited on pages 27, 82 and 83.)

[53] A.P. Avolio. Multi-branched model of the human arterial system. *Medical and Biological Engineering and Computing*, 18(6):709–718, 1980. ISSN 0140-0118. doi:

10.1007/BF02441895. URL `http://dx.doi.org/10.1007/BF02441895`. (Cited on pages 27, 82 and 83.)

[54] M.S. Olufsen, C.S. Peskin, W.Y. Kim, E.M. Pedersen, A. Nadim, and J. Larsen. Numerical simulation and experimental validation of blood flow in arteries with structured-tree outflow conditions. *Annals of biomedical engineering*, 28 (11):1281–1299, 2000. ISSN 0090-6964. doi: 10.1114/1.1326031. URL `http://dx.doi.org/10.1114/1.1326031`. (Cited on pages 27, 82 and 83.)

[55] M.S. Olufsen. Structured tree outflow condition for blood flow in larger systemic arteries. *American Journal of Physiology- Heart and Circulatory Physiology*, 276 (1):H257, 1999. ISSN 0363-6135. (Cited on pages 27, 28, 82 and 83.)

[56] S.R. Devasahayam. *Signals and systems in biomedical engineering : signal processing and physiological systems modeling.* Topics in biomedical engineering international book series. Kluwer Academic/Plenum Publishers, New York, 2000. ISBN 0-306-46391-1. (Cited on pages 27 and 83.)

[57] I.E. Vignon-Clementel, C. Alberto Figueroa, K.E. Jansen, and C.A. Taylor. Outflow boundary conditions for three-dimensional finite element modeling of blood flow and pressure in arteries. *Computer Methods in Applied Mechanics and Engineering*, 195(29-32):3776–3796, 2006. ISSN 0045-7825. doi: 10.1016/j.cma.2005.04.014. URL `http://dx.doi.org/10.1016/j.cma.2005.04.014`. (Cited on pages 28 and 83.)

[58] J.R. Cebral, C.M. Putman, M.T. Alley, T. Hope, R. Bammer, and F. Calamante. Hemodynamics in normal cerebral arteries: qualitative comparison of 4D phase-contrast magnetic resonance and image-based computational fluid dynamics. *Journal of engineering mathematics*, 64(4):367–378, 2009. ISSN 0022-0833. doi: 10.1007/s10665-009-9266-2. URL `http://dx.doi.org/10.1007/s10665-009-9266-2`. (Cited on page 28.)

[59] S.Z. Zhao, X.Y. Xu, A.D. Hughes, S.A. Thom, A.V. Stanton, B. Ariff, and Q. Long. Blood flow and vessel mechanics in a physiologically realistic model of a human carotid arterial bifurcation. *Journal of Biomechanics*, 33(8):975–984, 2000. ISSN 0021-9290. doi: 10.1016/S0021-9290(00)00043-9. URL `http://dx.doi.org/10.1016/S0021-9290(00)00043-9`. (Cited on pages 29, 34, 56 and 57.)

[60] K. Perktold and G. Rappitsch. Computer simulation of local blood flow and vessel mechanics in a compliant carotid artery bifurcation model. *Journal of Biomechanics*, 28(7):845–856, 1995. ISSN 0021-9290. doi: 10.1016/0021-9290(95)95273-8. URL `http://dx.doi.org/10.1016/0021-9290(95)95273-8`. (Cited on page 29.)

[61] Y. Bazilevs, M.C. Hsu, D.J. Benson, S. Sankaran, and A.L. Marsden. Computational fluid-structure interaction: methods and application to a total cavopulmonary connection. *Computational Mechanics*, 45(1):77–89, 2009. ISSN 0178-7675. doi: 10.1007/s00466-009-0419-y. URL `http://dx.doi.org/10.1007/s00466-009-0419-y`. (Cited on page 29.)

[62] R. Torii, M. Oshima, T. Kobayashi, K. Takagi, and T.E. Tezduyar. Fluid-structure interaction modeling of aneurysmal conditions with high and normal blood pressures. *Computational Mechanics*, 38(4):482–490, 2006. ISSN 0178-7675. doi: 10.1007/s00466-006-0065-6. URL `http://dx.doi.org/10.1007/s00466-006-0065-6`. (Cited on pages 29 and 34.)

[63] J.M. Guccione, G.S. Kassab, and M.B. Ratcliffe, editors. *Computational Cardiovascular Mechanics : Modeling and Applications in Heart Failure*. Springer, New York, Dordrecht, Heidelberg, London, 2010. ISBN 978-1-4419-0729-5. doi: 10.1007/978-1-4419-0730-1. URL `http://dx.doi.org/10.1007/978-1-4419-0730-1`. (Cited on page 30.)

[64] G.P. Galdi, R. Rannacher, A.M. Robertson, and S. Turek, editors. *Hemodynamical flows : Modeling, Analysis and Simulation*. Oberwolfach Seminars ; 37. Birkhäuser, Basel [u.a.], 2008. ISBN 3-7643-7805-0 ; 978-3-7643-7805-9. doi: 10.1007/978-3-7643-7806-6. URL `http://dx.doi.org/10.1007/978-3-7643-7806-6`. (Cited on pages 30 and 44.)

[65] D. Gross, W. Hauger, J. Schröder, and E.A. Werner, editors. *Formeln und Aufgaben zur Technischen Mechanik 4 : Hydromechanik, Elemente der Höheren Mechanik, Numerische Methoden*. Springer-Lehrbuch. Springer-Verlag Berlin Heidelberg, Berlin, Heidelberg, 2008. ISBN 978-3-540-49843-8. doi: 10.1007/978-3-540-49843-8. URL `http://dx.doi.org/10.1007/978-3-540-49843-8`. (Cited on pages 32 and 42.)

[66] *ScanIP™, +ScanFE™ and +ScanCAD™ Reference Guide*. Simpleware LTD, Innovation Centre Rennes Drive Exeter EX4 4RN, UK, 2010. (Cited on page 37.)

[67] *Gambit 2.4 User's Guide*. Fluent Incorporated, Centerra Resource Park 10, Cavendish Court Lebanon, NH 03766, 2007. (Cited on page 39.)

[68] *Fluent 6.3 User Guide*. Fluent Incorporated, Centerra Resource Park 10, Cavendish Court Lebanon, NH 03766, 2007. (Cited on pages 40, 43, 50, 51, 52, 53, 54, 55 and 59.)

[69] S.M. Salim and S.C. Cheah. Wall y^+ Strategy for Dealing with Wall-bounded Turbulent Flows. In *Proceedings of the International MultiConference of Engineers and Computer Scientists 2009 Vol II*, IMECS, Hong Kong, March 2009. ISBN 978-988-17012-7-5. URL `http://www.iaeng.org/publication/IMECS2009/IMECS2009_pp2165-2170.pdf`. (Cited on pages 40, 51 and 59.)

[70] University of Tennessee. Velocity Vector and Strain Rate Tensor. website, 2010. URL `http://web.utk.edu/kit/443/vv-srt.pdf`. last checked 28/11/2010. (Cited on page 42.)

[71] Drug Bank Cisplatin. website, 2010. URL `http://www.drugbank.ca/cgi-bin/show_drug.cgi?CARD=DB00515`. last checked 28/12/2010. (Cited on page 45.)

[72] P. Pedersen. Axisymmetric analytical stiffness matrices with Green-Lagrange strains. *Computational Mechanics*, 35(3):227–235, 2005. ISSN 0178-7675. doi: 10.1007/s00466-004-0619-4. URL `http://dx.doi.org/10.1007/s00466-004-0619-4`. (Cited on page 46.)

[73] M. Lesieur. *Turbulence in fluids*. Fluid mechanics and its applications ; 84. Springer, Dordrecht, 4., rev. and enlarged ed. edition, 2008. ISBN 978-1-4020-6434-0. doi: 10.1007/978-1-4020-6435-7. URL `http://dx.doi.org/10.1007/978-1-4020-6435-7`. (Cited on page 47.)

[74] F. Durst. *Fluid Mechanics of Fluid Flows : An Introduction to the Theory of Fluid Flows*. Springer, Berlin, 2008. ISBN 978-3-540-71342-5 ; 978-3-540-71343-2. URL `http://www.springerlink.com/content/978-3-540-71342-5`. (Cited on pages 48 and 51.)

[75] CFD Online Wiki : Turbulence Intensity. website, 2010. URL `http://www.CFD-online.com/Wiki`. last checked 15/10/2010. (Cited on page 50.)

[76] D.C. Wilcox. *Turbulence modeling for* CFD. DCW Industries, La Cañada, Calif., 1993. ISBN 0-9636051-0-0. (Cited on page 51.)

[77] F.R. Menter. Improved two-equation k-omega turbulence models for aerodynamic flows. *NASA STI/Recon Technical Report N*, 93:22809–+, oct 1992. URL `http://adsabs.harvard.edu/abs/1992STIN...9322809M`. (Cited on page 51.)

[78] Y. Hoi, B.A. Wasserman, Y.J. Xie, S.S. Najjar, L. Ferruci, E.G. Lakatta, G. Gerstenblith, and D.A. Steinman. Characterization of volumetric flow rate waveforms at the carotid bifurcations of older adults. *Physiological Measurement*, 31:291, 2010. doi: 10.1088/0967-3334/31/3/002. URL `http://dx.doi.org/10.1088/0967-3334/31/3/002`. (Cited on pages 56, 57, 73 and 74.)

[79] J.M. Meinders and A.P.G. Hoeks. Simultaneous assessment of diameter and pressure waveforms in the carotid artery. *Ultrasound in medicine & biology*, 30 (2):147–154, 2004. ISSN 0301-5629. doi: 10.1016/j.ultrasmedbio.2003.10.014. URL `http://dx.doi.org/10.1016/j.ultrasmedbio.2003.10.014`. (Cited on page 57.)

[80] I. Zaccari, A.C. Rossi, E.M.H. Bosboom, and P.J. Brands. Pressure waveform estimation in the common carotid artery Different methods in comparison. In *4th European Conference of the International Federation for Medical and Biological Engineering*, pages 2536–2539. Springer, 2009. doi: 10.1007/978-3-540-89208-3_608. URL `http://dx.doi.org/10.1007/978-3-540-89208-3_608`. (Cited on page 57.)

[81] J.S. Milner, J.A. Moore, B.K. Rutt, and D.A. Steinman. Hemodynamics of human carotid artery bifurcations: computational studies with models reconstructed from magnetic resonance imaging of normal subjects. *Journal of vascular surgery*, 28(1):143–156, 1998. ISSN 0741-5214. doi: 10.1016/S0741-5214(98)70210-1. URL `http://dx.doi.org/10.1016/S0741-5214(98)70210-1`. (Cited on page 57.)

[82] I. Marshall, P. Papathanasopoulou, and K. Wartolowska. Carotid flow rates and flow division at the bifurcation in healthy volunteers. *Physiological Measurement*, 25:691, 2004. doi: 10.1088/0967-3334/25/3/009. URL `http://dx.doi.org/10.1088/0967-3334/25/3/009`. (Cited on page 57.)

[83] C.R. Deane and H.S. Markus. Colour velocity flow measurement: in vitro validation and application to human carotid arteries. *Ultrasound in medicine & biology*, 23(3):447–452, 1997. ISSN 0301-5629. doi: 10.1016/S0301-5629(96)00224-4. URL `http://dx.doi.org/10.1016/S0301-5629(96)00224-4`. (Cited on page 57.)

[84] SZ Zhao, XY Xu, MW Collins, AV Stanton, AD Hughes, and SA Thom. Flow in carotid bifurcations: effect of the superior thyroid artery. *Medical engineering & physics*, 21(4):207–214, 1999. ISSN 1350-4533. doi: 10.1016/S1350-4533(99)00046-6. URL `http://dx.doi.org/10.1016/S1350-4533(99)00046-6`. (Cited on page 57.)

[85] D. Campbell. Catheters. E-mail correspondence, 2011. transmitted 21/01/2011 & 24/01/2011. (Cited on page 71.)

List of tables

List of figures

NOMENCLATURE

Abbreviations

ALE	Arbitrary Euler Lagrange	30
APA	Ascending Pharyngeal Artery	17
BCA	Brachiocephalic Artery	17
CAD	Computer Aided Design	39
CCA	Common Carotid Artery	17
CFD	Computational Fluid Dynamics	11
CGS	Centimetre Gram Second	27
CMBE	Computational & Mathematical Biomedical Engineering	7
COMSOL	Comsol®	70
CT	Computer Tomography	15
DNS	Direct Numerical Simulation	48
ECA	External Carotid Artery	17
ERASMUS	EuRopean Action Scheme for the Mobility of University Students	7
FA	Facial Artery	17
FLUENT	Fluent®	38
FSI	Fluid Structure Interaction	30
GAMBIT	Gambit®	39
GUI	Graphical User Interface	x
ICA	Internal Carotid Artery	17
IGES	Initial Graphics Exchange Specification	82
LA	Lingual Artery	17
LES	Large Eddy Simulation	50
MATLAB	Matlab®	35
MRI	Magnetic Resonance Imaging	15
PISO	Pressure Implicit with Splitting of Operators	75
RANS	Reynolds Averaged Navier Stokes	49
RSA	Right Subclavian Artery	17
SCANCAD	$^{+}$ScanCAD™	38
SCANIP	ScanIP™	38
SWORKS	SolidWorks®	39
SST	Shear Stress Transport	40
STA	Superior Thyroid Artery	17
TUI	Text User Interface	x

US	Ultrasound Scanner		37
VA	Vertebral Artery		17
VOF	Volume of Fluid		19

Symbols

α	activation energy	$\mathrm{J/kg \cdot mol}$	44
α_W	Womersley number	–	25
$\dot{\gamma}$	shear rate	$\mathrm{s^{-1}}$	42
$\dot{m}$	mass flow rate	$\mathrm{kg/s}$	32
$\dot{V}$	rate of flow	$\mathrm{m^3/s}$	31
ϵ	strain	–	42
ϵ_φ	circumferential strain	–	33
ϵ_r	radial strain	–	33
λ	thermal conductivity	$\mathrm{W/m\,K}$	49
λ_r	friction coefficient	–	24
λ_t	time constant	s	43
$\mathbb{R}$	reflection factor	–	27
$\mathbb{T}$	transmission factor	–	27
$\mathcal{C}$	electrical capacitance	F	28
$\mathcal{I}$	electrical current	A	24
$\mathcal{L}$	electrical inductance	H	28
$\mathcal{R}$	electrical resistance	Ω	24
$\mathcal{U}$	electrical voltage	V	24
μ	dynamic viscosity	Pa s	42
μ_0	dynamic viscosity at zero shear rate	Pa s	43
μ_∞	dynamic viscosity at infinity shear rate	Pa s	43
μ_c	viscosity of continuous component	Pa s	54
μ_p	plasma viscosity	Pa s	43
μ_T	dynamic eddy viscosity	Pa s	48
ν	kinematic viscosity	$\mathrm{m^2/s}$	42
ν_p	Poisson's ratio	–	33
ω	specific dissipation rate	$\mathrm{1/s}$	53
ω_h	heart rate	$\mathrm{rad/s}$	25
$\overline{\overline{\tau_{Re}}}$	Reynolds stress tensor	$\mathrm{N/m^2}$	49
$\overline{\overline{\tau}}$	stress tensor	$\mathrm{N/m^2}$	42
$\overline{\overline{D}}$	strain rate tensor	$\mathrm{1/s}$	42
$\overline{\overline{e}}$	Green-Lagrange strain tensor	–	47
Ψ	strain energy	J	47
ρ	density	$\mathrm{kg/m^3}$	42
ρ_d	density of dispersed component	$\mathrm{kg/m^3}$	54
σ_φ	circumferential stress	$\mathrm{N/m^2}$	32

σ_r	radial stress	$^{\mathrm{N}}/_{\mathrm{m}^2}$	32
τ_c	characteristic time scale	s	54
τ_d	particle relaxation time	s	54
τ_{wall}	wall shear stress	$^{\mathrm{N}}/_{\mathrm{m}^2}$	40
φ	angle	°	30
$\vec{\bar{u}}$	time averaged velocity vector	$^{\mathrm{m}}/_{\mathrm{s}}$	48
$\vec{F}$	force vector	N	41
$\vec{u'}$	turbulent velocity fluctuation vector	$^{\mathrm{m}}/_{\mathrm{s}}$	48
$\vec{U}$	displacement vector	m	42
$\vec{u}$	velocity vector	$^{\mathrm{m}}/_{\mathrm{s}}$	21
$\vec{x}$	Cartesian coordinates vector	m	21
$\widehat{u}$	max. velocity	$^{\mathrm{m}}/_{\mathrm{s}}$	59
ξ	pressure loss coefficient	–	24
A	surface	m^2	41
C	circumference	m	53
c	wave speed	$^{\mathrm{m}}/_{\mathrm{s}}$	25
$C_0 \ldots C_3$	integration constants	–	32
C_μ	turbulence model constant	–	53
c_p	specific heat capacity	$^{\mathrm{J}}/_{\mathrm{kg\ K}}$	49
C_{cas}	blood deformation stress	$^{\mathrm{N}}/_{\mathrm{m}^2}$	43
d_d	bubble diameter	m	54
d_h	hydraulic diameter	m	53
E	modulus of elasticity	$^{\mathrm{N}}/_{\mathrm{m}^2}$	33
F	stress function	–	32
g	acceleration of gravity	$^{\mathrm{m}}/_{\mathrm{s}^2}$	23
H	height	m	41
h	wall thickness	m	25
Ht	haematocrit	–	43
I	turbulence intensity	–	53
I_1	first invariant	$\mathrm{N/m^2}$	42
I_2	second invariant	${\mathrm{N/m^2}}^2$	42
I_3	third invariant	${\mathrm{N/m^2}}^3$	42
j	complex number	–	28
K	consistency index	$\mathrm{Pa\ s^n}$	43
k	turbulent kinetic energy	$^{\mathrm{m}^2}/_{\mathrm{s}^2}$	53
K_{cas}	Casson viscosity	Pa s	43
L	overall length	m	61
l	length	m	61
l_e	entrance length	m	24
l_T	turbulence length scale	m	53

m	Cross rate constant	–	43
N	distribution exponent	–	23
n	Power-law index	–	43
p	pressure	$\mathrm{N/m^2}$	49
R	hydraulic resistance	$\mathrm{N\,s^2/m^8}$	24
r	radius	m	30
r_a	outer radius	m	23
Re	Reynolds number	–	53
s	complex argument	$\mathrm{1/s}$	28
St	Stokes number	–	54
T	temperature	K	43
t	time	s	48
T_0	reference temperature	K	44
T_α	reference temperature	K	44
t_p	periodic time	s	55
u'_{rms}	root mean square of turbulent velocity fluctuation	$\mathrm{m/s}$	49
u_b	velocity component of a body in x direction	$\mathrm{m/s}$	41
U_r	radial displacement	m	33
u_t	friction velocity	$\mathrm{m/s}$	40
u_{mag}	velocity magnitude	$\mathrm{m/s}$	49
w_{mean}	mean velocity	$\mathrm{m/s}$	32
y^+	dimensionless wall distance	–	40
y_{wall}	distance to the nearest wall	m	40
Z	characteristic impedance	$\mathrm{kg/m^4\,s}$	26

A Appendix

This chapter describes mainly self written MATLAB programs and summarizes useful FLUENT and Linux commands, which were used during computation. In Section A.5, the general project objectives are listed and it is discussed to what extent they have been fulfilled.

A.1 FSI Program

Using the differential equations of Section 2.3, a MATLAB file was created to solve the fluid-structure-interaction for laminar, incompressible flow with a *Newtonian* fluid and linear elasticity in an ideal pipe geometry. A validation test was made with COMSOL. The input parameters were pipe length $L = 0.1\,\mathrm{m}$, inner radius $b = 0.0025\,\mathrm{m}$, outer radius $a = 0.0028\,\mathrm{m}$, inlet pressure $p_i(0) = 600\,\mathrm{Pa}$, viscosity $\mu = 0.00345\,\mathrm{Pa\ s}$, Poisson's ratio $\nu_p = 0.499$ and the modulus of elasticity $E = 100000\,{}^{\mathrm{N}}\!/\!{}_{\mathrm{m}^2}$, compare Fig. 2.6. All other pressures were set to zero. The pipe dimensions, radius and wall thickness, are typical for the carotid artery, Tab. 1.1.

Figure A.1 shows solid mechanics and fluid mechanics results of the own program and COMSOL. Stress, strain and pressure show a high correlation. The velocity is much lower in the COMSOL simulation, by reason of the entrance length (2.8), which is in this case approximately 0.69 m on *Reynolds* number 2200. The flow is not fully developed in the COMSOL computation. The analytical model, which uses *Hagen-Poiseuille* law, assumes a fully developed laminar flow. Hence, the velocity level is higher. Due to the high memory consumption of COMSOL, a model which represents a long fluid entrance length, was not possible to run. The code of the program is shown below.

FSI program for a thick walled tube, laminar flow, Hoke's law or non-linear

```
clc
clear
close all
%input
%outer radius [m]
a=0.0028;
%inner radius [m]
b=0.0025;
%length [m]
L=0.1;
%outer pressure [Pa=N/m^2]
```

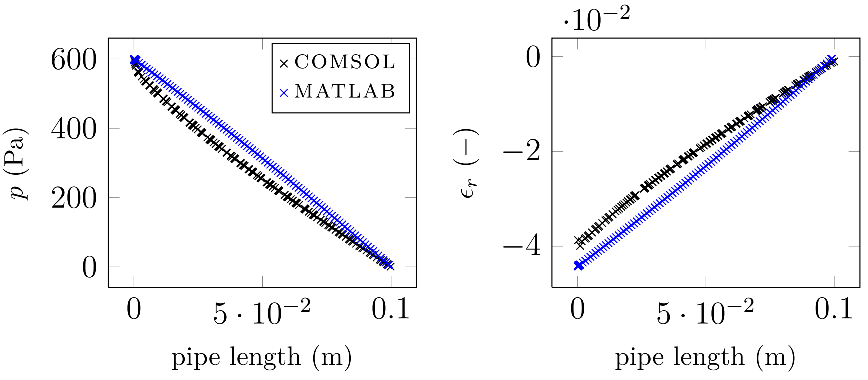

(a) Pressure.

(b) Radial strain.

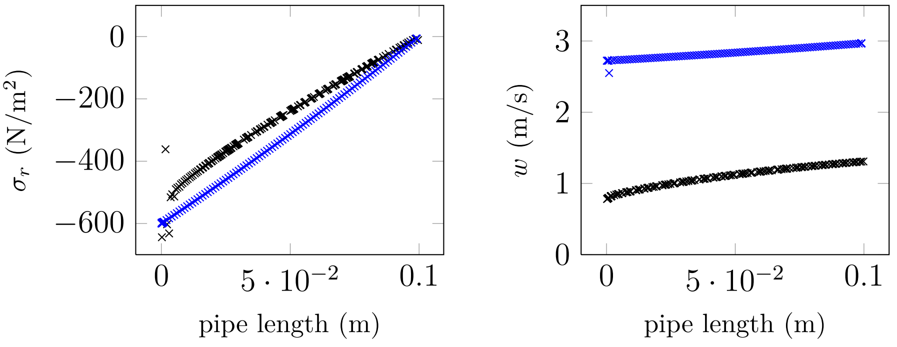

(c) Radial stress.

(d) Velocity at core.

Figure A.1: FSI validation of the own written MATLAB program with COMSOL. The significant deviation in Fig.(d) is explainable through the entrance length, which is not considered in the MATLAB program.

```
p_a=0;
%inner pressure start [Pa]
p_i0=800;
%inner pressure end [Pa]
p_iL=0;
%dynamic viscosity [Pa s]
mu=0.00345;
%Poisson's number [-]
n=0.499;
%density [kg/m^3]
rho=1056;
%number of discretization points in r direktion (pipe radius)
disk=10;
%number of discretization points in z direktion (pipe length)
ldisk=30;
%damping for pressure change
damping=100;
%number of iterations for fluid flow
i_fluid=1000;
%number of iterations for fsi coupling
i_fsi=50;
%Elasticity
%constant modulus of elsticity [N/m^2]=[Pa]
E=1*10^6;
%measured data from Holzapfel_2009
epsilon=[0 0.025 0.1 0.12 0.18 0.25 0.28 0.29 0.294 0.297 0.3];
sigma=[0 2000 7500 10000 16000 28000 50000 80000 100000 115000 130000]; %[Pa]
% polynom coefficients
p=polyfit(sigma,epsilon,7);
%for checking polynom quality
%polytool(sigma,epsilon,7)
sigma=(0:10:130000);
%strain stress function
epsilon=polyval(p,sigma);
```

Computing

```
%wallthickness
t=a-b;
%length variable
z=(0:(L/ldisk):L);
z(:,1)=[];
za=(0:(L/(10*ldisk)):(L/ldisk)); %finer discretization at the inlet
za(:,length(za))=[];
z=[za z];
%radius variable
r=(b:(t/disk):a).';
```

Initialize

```
%pressure drop dpi/dz
dpi_dz=(p_iL-p_i0)/L;
%pressure p_i(z)
p_iz=dpi_dz*z+p_i0;
%meshgrid
[P_IZ,R]=meshgrid(p_iz,r);
%radial stress
sigma_r=(a^2*b^2*(p_a-P_IZ))./((a^2-b^2).*R.^2)-(a^2*p_a-b^2.*P_IZ)/(a^2-b^2);
%circumferential stress
sigma_phi=(-a^2*b^2*(p_a-P_IZ))./((a^2-b^2).*R.^2)-(a^2*p_a-b^2.*P_IZ)/(a^2-b^2);
%circumferential strain EVZ
```

```
epsilon_phi=(sigma_phi*(1-n^2))./E - (n*sigma_r*(1-n^2))./(E*(1-n));
%with non linear strain stress function
epsilon_phi_nl=polyval(p,(sigma_phi))*(1-n^2) -...
polyval(p,(sigma_r))*n*(1-n^2)/(1-n);
%wall shape
%!switch between Hoke's law and non-linear elasticity!
b_z=(epsilon_phi_nl+1).*R;
b_z_init=b_z;
%original wall shape
b_0=z;
b_0(1,:)=b;
%rate of flow
v=-pi*b_z(1,:).^4/(8*mu).*dpi_dz;
```

FSI Coupling

```
for i=1:i_fsi;
i=i+1;
%Residual rate of flow without pulsatory inlet region (za)
iter(i,1)=i;
v_cut=v(:,length(za):length(v));
residu(i,1)=max(v_cut)-min(v_cut);
```

Iteration fluid flow

```
for i=1:i_fluid;
i=i+1;
%rate of flow
v=-pi*b_z(1,:).^4/(8*mu).*dpi_dz;
%norm v
v_norm=v./(max(v)-min(v));
%norm p_iz
p_iz_norm=p_iz./(max(p_iz)-min(p_iz));
%conservation of mass, it should be zero
delta_v=gradient(v_norm);
delta_v=0-delta_v;
%changing p_iz DAMPING is needed!!
p_iz_norm=p_iz_norm+(delta_v./damping);
p_iz=p_iz_norm.*(max(p_iz)-min(p_iz));
%replace boundary conditions p_i0 and p_iL
p_iz(1,1)=p_i0;
p_iz(1,(length(p_iz)))=p_iL;
%replace dpi_dz
grad_p_iz=gradient(p_iz);
grad_z=gradient(z);
dpi_dz=grad_p_iz./grad_z;
end
```

Solid reaktion

```
%linear elastic
[P_IZ,R]=meshgrid(p_iz,r);
%radial stress
sigma_r=(a^2*b^2*(p_a-P_IZ))./((a^2-b^2).*R.^2)-(a^2*p_a-b^2.*P_IZ)/(a^2-b^2);
%circumferential stress
sigma_phi=(-a^2*b^2*(p_a-P_IZ))./((a^2-b^2).*R.^2)-(a^2*p_a-b^2.*P_IZ)/(a^2-b^2);
%circumferential strain EVZ
epsilon_phi=(sigma_phi*(1-n^2))./E - (n*sigma_r*(1-n^2))./(E*(1-n));
%with non linear strain stress function
epsilon_phi_nl=polyval(p,(sigma_phi))*(1-n^2) -...
polyval(p,(sigma_r))*n*(1-n^2)/(1-n);
```

```
%wall shape
%!switch between Hoke's law and non-linear elasticity!
b_z=(epsilon_phi_nl+1).*R;
end
```

Final Results

```
%radial stress
sigma_r=(a^2*b^2*(p_a-P_IZ))./((a^2-b^2).*R.^2)-(a^2*p_a-b^2.*P_IZ)/(a^2-b^2);
%circumferential stress
sigma_phi=(-a^2*b^2*(p_a-P_IZ))./((a^2-b^2).*R.^2)-(a^2*p_a-b^2.*P_IZ)/(a^2-b^2);
%axial stress just in EVZ!!!
sigma_z=n*(sigma_r+sigma_phi);
%sigma_v v Mieses
sigma_v=sqrt(sigma_r.^2+sigma_phi.^2+sigma_z.^2-sigma_r.*sigma_z-sigma_r...
.*sigma_phi-sigma_phi.*sigma_z);
%radial strain EVZ
epsilon_r=(sigma_r*(1-n^2))./E - (n*sigma_phi*(1-n^2))./(E*(1-n));
%with non linear strain stress function
epsilon_r_nl=polyval(p,(sigma_r))*(1-n^2)- polyval(p,(sigma_phi))*n*(1-n^2);
%circumferential strain EVZ
epsilon_phi=(sigma_phi*(1-n^2))./E - (n*sigma_r*(1-n^2))./(E*(1-n));
%with non linear strain stress function
epsilon_phi_nl=polyval(p,(sigma_phi))*(1-n^2) - polyval(p,(sigma_r))*n*(1-n^2)/(1-n);
%wall shape
%!switch between Hoke's law and non-linear elasticity!
b_z=(epsilon_phi_nl+1).*R;
%rate of flow
v=-pi*b_z(1,:).^4/(8*mu).*dpi_dz;
%mean velocity
w_mean=-b_z(1,:).^2/(8*mu).*dpi_dz;
%Reynolds number
Re=(w_mean.*(2.*b_z(1,:))*rho)/mu;
%meshgrid for fluid region with deformed boundary wall linear
r_z=b_z;
for i=1:length(r_z);
j=(0:(r_z(1,i)/disk):r_z(1,i));
j=j';
k(:,i)=j;
end
r_z=k;
%w(r,z) velocity function
for i=1:length(r_z);
w= (-1)/(4*mu) * (b_z(1,i).^2 - r_z(:,i).^2).*dpi_dz(:,i);
k(:,i)=w;
end
w=k;
%max velocity
w_max=w(1,:);
%Matrix for output z' | p_iz' | Re' | w_max' | b_z(1,:)'
%pipe length | pressure | Re | w_max | wall shape
out=[z',p_iz',Re',w_max',b_z(1,:)'];
%cut off inlet region with wrong results for all variables
out=out(length(za):length(out),:);
%add inlet pressure boundary condition to out file
p_i_bound=p_i0.*ones(length(out),1);
out=[p_i_bound,out];
%write text file
dlmwrite('fsi-out.txt', out, 'delimiter', '\t', 'precision', 10)
%cut off inlet region za for velocity 3D function
w_cut=w(:,length(za):length(w));
r_z_cut=r_z(:,length(za):length(r_z));
```

```
%Z coordinate for velocity 3D function
Z=meshgrid(z , ones(length(r),1));
Z=Z(:,length(za):length(Z));
```

Figures

```
%fliud
figure
subplot(2,3,1)
stem(z,v)
title('rate of flow')
xlabel('pipe length (m)')
ylabel('rate of flow (m^3/s)')

subplot(2,3,2)
stem(z,p_iz)
title('pressure')
xlabel('pipe length (m)')
ylabel('pressure (Pa)')

subplot(2,3,3)
stem(z,w_mean)
title('mean velocity')
xlabel('pipe length (m)')
ylabel('mean velocity (m/s)')

subplot(2,3,4)
stem(iter,residu)
title('residual (without za)')
xlabel('iteration')
ylabel('rate of flow max-min')

subplot(2,3,5)
stem(z,Re)
title('Reynolds number !laminar!')
xlabel('pipe length (m)')
ylabel('Re (-)')

subplot(2,3,6)
surfc(Z,r_z_cut,w_cut,'EdgeColor','none')
title('velocity profile (without za)')
xlabel('pipe length (m)')
ylabel('radius (m)')
zlabel('velocity (m/s)')

%solid
figure
subplot(2,3,1)
surf(z,b_z,sigma_r,'EdgeColor','none')
title('radial stress')
xlabel('pipe length (m)')
ylabel('radius (m)')
zlabel('stress (Pa)')

subplot(2,3,2)
surf(z,b_z,sigma_phi,'EdgeColor','none')
title('circumferential stress')
xlabel('pipe length (m)')
ylabel('radius (m)')
zlabel('stress (Pa)')

subplot(2,3,3)
```

```
surf(z,b_z,sigma_z,'EdgeColor','none')
title('axial stress (plain strain)')
xlabel('pipe length (m)')
ylabel('radius (m)')
zlabel('stress (Pa)')

subplot(2,3,4)
surf(z,b_z,sigma_v,'EdgeColor','none')
title('v Mieses stress')
xlabel('pipe length (m)')
ylabel('radius (m)')
zlabel('stress (Pa)')

subplot(2,3,5)
surf(z,b_z,epsilon_r,'EdgeColor','none')
title('radial strain')
xlabel('pipe length (m)')
ylabel('radius (m)')
zlabel('strain (m/m)')

subplot(2,3,6)
surf(z,b_z,epsilon_phi,'EdgeColor','none')
title('circumferential strain')
xlabel('pipe length (m)')
ylabel('radius (m)')
zlabel('strain (m/m)')

%wallshape and non-linear elasticity
figure
subplot(1,2,1)
plot(z,b_z(1,:),z,b_z_init(1,:),z,b_0)
h=legend('fsi result','init','original');
set(h,'Interpreter','none')
title('wall shape')
xlabel('pipe length (m)')
ylabel('radius (m)')

subplot(1,2,2)
plot(epsilon,sigma)
title('non linear elasticity')
xlabel('strain')
ylabel('stress (Pa)')
```

A.2 Boundary Program

The boundary conditions are realized as transient table. A MATLAB program was written for the variation of the time step size.

Boundary program to generate a transient table

```
clc;
clear;
close all;
```

Input

```
area_cca=3.173945e-05; %(m^2)
```

```
area_cisp=2.851038e-07; %(m^2)
% Rate of flow from Hoi2010
read=importdata('Hoi_2010.txt');
time=read.data(:,1);
cca=read.data(:,2);
ica=read.data(:,3);
eca=read.data(:,4);

% downsampling, because to many points
pick=10;
cca_d=downsample(cca,pick);
ica_d=downsample(ica,pick);
eca_d=downsample(eca,pick);
time_d=downsample(time,pick);

% Pressure from Vermeersch2008
readP=importdata('vermeersch_2008.txt');
timeP=readP.data(:,1);
pressure=readP.data(:,2);
```

Computing

```
points=200; % number of time steps
t=linspace(time(1,:),time(length(time),:),points)'; % equal distance in t
tP=linspace(timeP(1,:),timeP(length(timeP),:),points)'; % equal distance in t

%time shift flow
t=t-min(t); % shift function to t_min=0
time=time-min(time); %shift function to t_min=0
time_d=time_d-min(time_d); %shift function to t_min=0
t=t/1000; %convert ms->s
time=time/1000; %convert ms->s
time_d=time_d/1000; %convert ms->s

%fitting spline flow
cca_cs=csapi(time_d,cca_d);
cca_spline=fnval(cca_cs,t);
ica_cs=csapi(time_d,ica_d);
ica_spline=fnval(ica_cs,t);
eca_cs=csapi(time_d,eca_d);
eca_spline=fnval(eca_cs,t);

%time shift pressure
tP=tP-min(tP); % shift function to t_min=0
timeP=timeP-min(timeP); %shift function to t_min=0
shrink=tP./t; %stretch tP to fit excactly t
tP=tP/shrink(length(shrink),1);
timeP=timeP/shrink(length(shrink),1);

%fitting spline pressure
pressure_cs=csapi(timeP,pressure);
pressure_spline=fnval(pressure_cs,tP);

%cisplatin dose function
cisp_x1=0; % left root (s)
cisp_x2=0.3; % right root (s)
cisp_a=-31200; % parabel stretch factor
cisp=cisp_a*(t-cisp_x1).*(t-cisp_x2);
cisp(cisp<0)=0; % set minimum value to zero
display('Integral cisplatin volume per cycle (ml)')
cisp_int=trapz(t,(cisp./60)) % integral volume per cycle
cisp_vel=(cisp/60*10^-6/area_cisp); % velocity (m/s)
```

```
%cisplatin turbulence
Re=cisp_vel*0.6*10^-3*998.2/0.001003; % Reynolds (-)
ii=Re<2300; % delete laminar threshold
I=0.16*Re.^(-1/8); % turb Intensity
I(ii)=0; % set to zero at laminar flow
k_cisp=3/2*(cisp_vel.*I).^2; % k
omega_cisp=k_cisp.^(0.5)/(0.09^(1/4)*0.07*0.6*10^-3); % omega
ii=isnan(k_cisp); % delete NaN
k_cisp(ii)=0;
ii=isnan(omega_cisp);  % delete NaN
omega_cisp(ii)=0;
```

Figures

```
plot(time,cca,time,eca,time,ica,t,cca_spline,'o',t,ica_spline,'o',t,eca_spline,'o')
h=legend('cca','eca','ica','cca-spline','ica-spline','eca-spline');
set(h,'Interpreter','none');
title('Measured data from Hoi2010 & Matlab curve fitting');
xlabel('time (s)');
ylabel('flow rate (ml/min)');

figure
plot(timeP,pressure,tP,pressure_spline,'o')
title('Measured data from Vermeersch2008 & Matlab curve fitting');
xlabel('time (s)');
ylabel('pressure (mmHg)');

figure
plot(t,cca_spline,t,cisp)
h=legend('cca','cisp');
set(h,'Interpreter','none');
title('Flow cca and unsteady cisplatin');
xlabel('time (s)');
ylabel('flow rate (ml/min)');
```

Export

```
mflux_cca=cca_spline/60*10^-6*1056/area_cca; %convert in (kg/(s*m^2))
mflux_cisp=cisp/60*10^-6*998.2/area_cisp; %convert in (kg/(s*m^2))

export=[t,mflux_cca];
timestep=diff(t); % compute current time step size
display('timestep')
timestep(1,1)
export(length(export)+1,:)=[t(length(t),:)+timestep(1,:),mflux_cca(1,:)]; % add last line
display('length')
length(export)
%paste header manual in text file
%cca_m_flux 2 201 1
%time mflux
dlmwrite('boundary.txt', export, 'delimiter', '\t', 'newline', 'pc','precision', '%.4f')

%export with cisplatin funtion
exportplus=[t,mflux_cca,mflux_cisp,k_cisp,omega_cisp];
exportplus(length(exportplus)+1,:)=[t(length(t),:)+timestep(1,:)...
,mflux_cca(1,:),mflux_cisp(1,:),k_cisp(1,:),omega_cisp(1,:)];  % add last line
%paste header manual in text file
%cca_m_flux 5 201 1
%time ccamflux cispmflux cispk cispomega
dlmwrite('boundaryplus.txt', exportplus, 'delimiter', '\t', 'newline',...
'pc','precision', '%.4f')
```

A.3 Fluent Commands

The GUI of FLUENT does not allow the selection of non-*Newtonian* viscosity options when a turbulence model is used. The user has to activate this option explicitly by using the following TUI command.

```
define/models/viscous/turbulence-expert/turb-non-newtonian
```

To start parallel processing on a Windows or Linux machine, the following command is required in the command window (cmd.exe or shell).

`fluent 3d -t4` with the version 3d, 3ddp or 2d, 2ddp and t1-∞ processors

The batch mode is a very useful tool for large jobs and is faster in comparison with the GUI mode. The command for parallel processing on Linux is shown below.

```
fluent 3ddp -t3 -gu -driver null < inputfile >& outputfile &
```

An input file for an unsteady simulation is shown below. The output file contains residuals and error messages.

```
/file/read-case-data
catheterA_03.cas.gz
solve/set/time-step 0.0094
solve/set/reporting-interval 20
;100 timesteps and 4000 inner iterations
/solve/dual-time-iterate 100 4000
/file/write-case-data
catheterA_04.cas.gz
exit
yes
```

A.4 Linux Commands

Here are some useful Linux commands to use FLUENT or any other software on a server client system. The user name is in this case 1004229r and the server name is carnot.mech.gla.ac.uk.

To connect to the server and launch FLUENT use:

```
ssh -X carnot.mech.gla.ac.uk -l 1004229r
module load fluent
fluent 3d
```

To copy files from client to the server use:

```
scp file.ext 1004229r@carnot.mech.gla.ac.uk:/home/ugrad/10/1004229r...
```

To copy files from the server to client use:

```
scp 1004229r@carnot.mech.gla.ac.uk:/home/ugrad/10/1004229r
.../file.ext /home/user/...
```

This list of commands show some basic Linux features:

- `top` shows all processes on a machine.

- `top -u 1004229r` shows all processes of the user 1004229r.
- `ls -l` shows files with size and extension in a folder.
- `pwd` shows the user home directory.
- `rm` removes files.
- `mkdir` and `rmdir` create and remove folder.
- `tar cfvz folder.tar.gz folder1 file1,2...` creates archive.
- `tar xfvz archive.tar.gz` extracts archive.
- `gedit file` shows a file in a text editor.

A.5 Project Objectives

The original project objectives at the beginning of this study are specified below:

- Generation of realistic patient specific three dimensional head and neck arterial geometry out of image data, using SCANIP. ✓
- Mesh generation for a CFD model, using GAMBIT. ✓
- Comparative study of several turbulence and material models, as well as boundary conditions in a steady model, using FLUENT. ✓
- Computation of a transient two-component CFD model, considering the chemical agent injection and pulsatile blood flow. ✓
- Variation of the injection position and injection parameters. ✗

Apart from the last objective, all were entirely fulfilled. Due to a lack of measured data, it was impossible to determine appropriate boundary conditions for more then one catheter injection position. Additionally, the geometry import into a CAD system failed, and this is required for modelling a curved catheter.

A.6 E-mails

```
From: "Campbell Duncan (NHS Greater Glasgow & Clyde)"
<duncan.campbell1@nhs.net>
To: "st.rhode@googlemail.com" <st.rhode@googlemail.com>
CC: "manosh.paul@glasgow.ac.uk" <manosh.paul@glasgow.ac.uk>
Date: Fri, 21 Jan 2011 15:17:35 +0000
Subject: catheters
```

Hi Stephan,

The internal lumen of the catheter is 0.625mm, external 0.924mm
estimates - average lumen of ligual artery 2.5mm, facial artery 3mm

I have a catheter donated to the project for your review, which I'll bring in next time we meet..

Duncan

Mr D F Campbell FRCS (OMFS), FRCS, FDS, MB BS, BDS
Consultant Oral & Maxillofacial Surgeon
Queen Margaret's Hospital, Fife

From: "Campbell Duncan (NHS Greater Glasgow & Clyde)"
<duncan.campbell1@nhs.net>
To: Stephan Rhode <st.rhode@googlemail.com>
CC: Manosh Paul <Manosh.Paul@glasgow.ac.uk>
Date: Mon, 24 Jan 2011 09:53:05 +0000
Subject: RE: catheters

Thanks Stephan,

To help me understand please define 'boundary conditions'.

Regarding outlets you should allow for small branches of the main vessels (facial, lingual etc) All the branches off CCA and ECA are named but there are a few named brances off the ligual and facial, these will possibly not be rendered in your rendered images as they are fairly small or short. I estimate that between origin and outflow both the lingual and facial will discharge 15% of flow to these not imaged outlflows. e.g. branches of the facial relevant to your image but not rendered are ascending palatine,tonsillar, submental and submandib/glandular. I dont think anyone is likely to have researched the flow aspects of these branches so 15% is an estimate up for discussion. It would be ideal if we could vary some of these parameters and see how much it effects the results.

The injection is usually 50mls over 20 seconds and again can be automated or pressure controlled manually. This will make immediate sense when you watch the technique for an angiogram. It will be a useful finding to determine whether we can advise on the best means of injection to maximise the angiosomal area under the curve AUC(dose/time).

I cannot advise you definitively on the best technique from the 3 you mention. Some points for you to consider, HR is likley to be in phase but may vary e.g. at rest in 50+ yrs aroound 70 but during the stress of this procedure probably 90bpm, the heart and therefor pulse rate may vary and the relevant dose is the tissue dose which will not be pulsatile.

I am hoping for a modality that can illustrate the problem in a pulsatile way and guide the technique by determining the best way to maximise the AUC which may involve varying the catheter pressure in phase with pulse pressure, varying rate of injection and advising on what pressure would result in retrograde arterial flow and for how far back up the artery.

Duncan

Mr D F Campbell FRCS (OMFS), FRCS, FDS, MB BS, BDS
Consultant Oral & Maxillofacial Surgeon
Queen Margaret's Hospital, Fife

B Declaration of originality

I confirm that this assignment is my own work and that I have:

- Read and understood the guidance on plagiarism in the Undergraduate Handbook, including the University of Glasgow Statement on Plagiarism.
- Clearly referenced, in both the text and the bibliography or references, all sources used in the work.
- Fully referenced (including page numbers) and used inverted commas for all text quoted from books, journals, web etc.
- Provided the sources for all tables, figures, data etc. that are not my own work.
- Not made use of the work of any other student(s) past or present without acknowledgement.
- In addition, I understand that any false claim in respect of this work will result in disciplinary action in accordance with University regulations.

I am aware of and understand the University's policy on plagiarism and I certify that this assignment is my own work, except where indicated by referencing, and that I have followed the good academic practices noted above.

Erklärung

Ich versichere hiermit wahrheitsgemäß, die Masterthesis bis auf die dem Betreuungsdozenten bereits bekannte Hilfe selbstständig angefertigt, alle benutzten Hilfsmittel vollständig und genau angegeben und alles kenntlich gemacht zu haben, was aus Arbeiten anderer unverändert oder mit Abänderung entnommen wurde.

Glasgow, 15th March 2011

Stephan Rhode